THE EFFECTS OF THE ENDOTHELIAL SURFACE LAYER ON RED BLOOD CELL DYNAMICS IN MICROVESSEL BIFURCATIONS
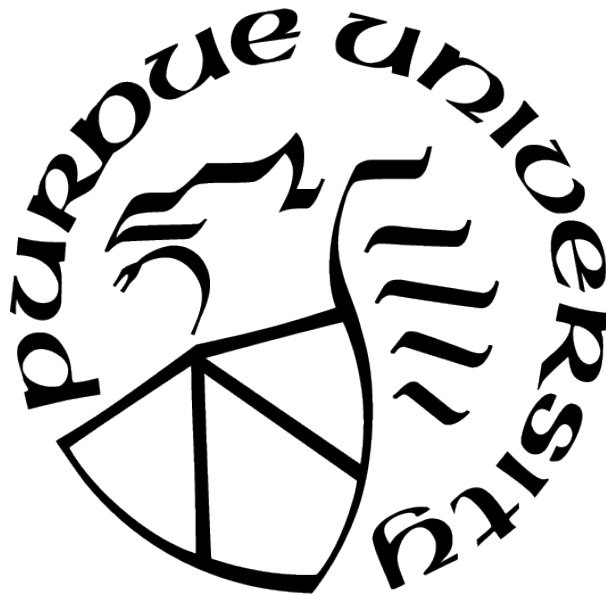
by

Carlson Triebold

A Dissertation

Submitted to the Faculty of Purdue University

In Partial Fulfillment of the Requirements for the degree of

Doctor of Philosophy

Department of Mathematics

West Lafayette, Indiana

August 2021

THE PURDUE UNIVERSITY GRADUATE SCHOOL
STATEMENT OF COMMITTEE APPROVAL

Dr. Jared Barber, Chair

Department of Mathematical Sciences, IUPUI

Dr. Julia Arciero

Department of Mathematical Sciences, IUPUI

Dr. Peijun Li

Department of Mathematics, Purdue University

Dr. Luoding Zhu

Department of Mathematical Sciences, IUPUI

Approved by:

Dr. Plamen Stefanov

For Becky

ACKNOWLEDGMENTS

First and foremost, I would like to thank my advisor, Dr. Jared Barber, for guiding me through this process every step of the way. I am forever grateful for his expertise, of which I was the fortunate recipient over the past few years, as well as his willingness to go above and beyond what was necessary to help me produce this work.

To the others on my defense committee, Dr. Julia Arciero, Dr. Peijun Li, and Dr. Luoding Zhu, thank you for your support and guidance. I am also thankful for the encouragement of my fellow students at IUPUI, especially Virgil Chan, Chris Neuffer, Michael Pilla, Erin Zhao, and Joel Zirkle.

To my parents, Carl and Carol, and siblings, Christopher, Conrad, Claire, and Caralyn, thank you for always believing in me, especially when I did not believe in myself.

And finally to my fiancée, Becky, who supported me from the beginning. I never would have been able to do this without you. Thank you.

TABLE OF CONTENTS

LIST OF TABLES

7

LIST OF FIGURES

10

11

ABSTRACT

Red blood cells (RBCs) make up 40-45% of blood and play an important role in oxygen transport. That transport depends on the RBC distribution throughout the body, which is highly heterogeneous. That distribution, in turn, depends on how RBCs are distributed or partitioned at diverging vessel bifurcations where one vessel flows into two. Several studies have used mathematical modeling to consider RBC partitioning at such bifurcations in order to produce useful insights. However, these studies assume that the vessel wall is a flat impenetrable homogeneous surface. While this is a good first approximation, especially for larger vessels, the vessel wall is typically coated by a flexible, porous endothelial surface layer (ESL) that is 0.5-1 µm thick. To better understand the possible effects of this layer on RBC partitioning, a diverging capillary bifurcation is analyzed using a flexible, two-dimensional RBC model. The model is also used to investigate RBC deformation and penetration of the ESL region when ESL properties are varied. The RBC is represented using interconnected viscoelastic elements. Stokes flow equations (viscous flow) model the surrounding fluid. The flow in the ESL is modeled using the Brinkman approximation for porous media with a corresponding hydraulic resistivity. The resistance of the ESL to compression is modeled using an osmotic pressure difference. The study includes isolated cells that pass through the bifurcation one at a time with no cell-cell interactions and two cells that pass through the bifurcation at the same time and interact with each other. A range of physiologically relevant hydraulic resistivities and osmotic pressure differences are explored.

For isolated cell simulations, decreasing hydraulic resistivity and/or decreasing osmotic pressure difference produced four behaviors: 1) RBC distribution nonuniformity increased; 2) RBC deformation decreased; 3) RBCs slowed down slightly; and 4) RBCs penetrated more deeply into the ESL. The presence of an altered flow profile and the ESL's resistance to penetration were primary factors responsible for these behaviors. In certain scenarios, ESL penetration was deep enough to present a possibility of cell adhesion, as can occur in pathological situations.

For paired cell simulations, more significant and complex changes were observed. Three types of effects that alter partitioning as hydraulic resistivity is changed are identified. De-

creasing hydraulic resistivity in the ESL produced lower RBC deformation. Including cell-cell interactions tended to increase deformation sharply compared to isolated cell scenarios. ESL penetration generally decreased for lower hydraulic resistivities except in scenarios with significant cell-cell interactions. This was primarily due to changes in flow profiles induced by the altered hydraulic resistivity levels.

1. INTRODUCTION

This study focuses on two aspects that play a significant role in blood flow dynamics, red blood cell (RBC) partitioning and the endothelial surface layer (ESL). At diverging vessel bifurcations where blood flows from one mother vessel into two daughter vessels, RBCs are often partitioned nonuniformly where, for instance, 5% of the RBCs go into one daughter branch even though 25% of the total blood flow goes into that branch [1], [2]. This contributes to the heterogeneous microvascular RBC distribution seen *in vivo* [2]. Experiments also give evidence for a 0.5-1 µm ESL that lines vessel walls [3], [4]. This contributes to vessel resistances that differ significantly from those predicted by glass tubes [5]. Further studies suggest the ESL has additional roles in shear-stimulated blood flow regulation [6] and in adhesion of platelets [7], leukocytes [8], and RBCs to vessel walls [9]. By using a mathematical model to consider the transport of one or two RBCs through an ESL-lined diverging capillary bifurcation, the studies presented in this dissertation help improve understanding of how ESL properties may affect RBC partitioning, deformation during partitioning, and the extent to which RBCs may interact with the ESL at bifurcations. This, in turn, can give insight into how ESL properties may affect the distribution and activities of other blood transported objects such as oxygen, which is carried by RBCs, other metabolites, drugs, platelets, and white blood cells. This can prove useful in studies of pathologies such as tumor vascularization [10], vascular occlusions [11], sickle cell anemia [12], and malaria [13].

Along with liquid plasma, RBCs are the primary constituents of blood by percentage, comprising 40-45% of its volume. At rest, RBCs are shaped like biconcave discs with a diameter of about 8 µm and a width of about 2 µm. They have a concentrated hemoglobin solution interior, a lipid bilayer membrane, and a cytoskeleton anchored into that membrane. This combination produces a viscoelastic response to deformation. RBCs are highly deformable and capable of passing through capillary vessels with diameters as small as approximately 2.7 µm [14]. Their flexibility and finite size contribute to the nonuniform partitioning seen at diverging vessel bifurcations. Using a model to take all these into account, Barber et al. [15] showed that RBC partitioning behavior in small capillary bifurcations at low RBC concentrations, or hematocrits, could be explained by three clearly defined effects. First,

an upstream finite size effect due to the finite size of the RBC and consequently the fact that the RBC's center of mass cannot get infinitely close to straight vessel walls. Second, a migration effect due to the flexibility of the RBC contributing to the RBC's tendency to migrate towards the center of a vessel upstream of a bifurcation. And finally, an obstruction effect due to the tendency for RBCs obstructing a lower flow downstream branch to be pulled into that lower flow vessel, also due to the finite size of the RBCs. Their results agreed well with Pries's [16], [2] empirically derived RBC partitioning function.

The endothelial glycocalyx (EGL) is comprised of two semi-distinct layers of membrane-bound macromolecules. The inner layer has been observed to have a quasi-periodic matrix structure [17] associated with bush like configurations of fibers [18] anchored into the endothelial cells that form the vessel wall. This layer extends approximately 0.05-0.4 µm from the vessel wall [19]. It then transitions into an outer layer, often referred to as the endothelial surface layer, or ESL. The ESL is made up of a more porous, loosely structured gel-like solution [19] which extends from the inner layer out into the vessel lumen a distance of, when combined with the inner layer, approximately 1 µm or more [3], [4].

The structure and function of these two layers has been studied extensively. Often, researchers have looked at properties of one of the layers while neglecting the other. This has sometimes led to confusion in terminology and the role of the osmotic pressure differences across the layers in hemodynamics [19], [20]. A primary function of the inner layer is its role as a molecular sieve for plasma proteins at the microvascular wall [21]. This results in a significant colloidal osmotic pressure drop across the layer of approximately 1.5×10^2 dyn/cm^2, placing the inner layer in a state of compression [20]. At the same time, observations suggest that flowing RBCs ($\geq$ 20 µm/s) do not invade the EGL while slower or stationary RBCs penetrate the EGL region [22]. Based on the hypothesis that the outer layer, or ESL, filaments resist flattening because of the colloidal osmotic pressures generated by plasma proteins in the ESL [23], Secomb et al. [3] found that an osmotic pressure increase of 20 dyn/cm^2 is sufficient to exclude RBCs from the layer, yet small enough to allow an RBC to completely compress the layer while stationary [24]. This predicted increase in osmotic pressure would place the ESL in a state of tension rather than compression. These

varying predictions (tension versus compression) for osmotic pressure differences in the EGL can be readily explained by the bi-layer model.

Besides its resistance to compression, the ESL is also known to impede the flow of plasma, which significantly increases flow resistance in microvessels when compared to *in vitro* studies of vessels with equal dimensions [25]. Modeling the ESL as a porous medium with a corresponding hydraulic resistivity and a resistive osmotic pressure difference, Secomb et al. [23] was able to obtain vessel flow resistance estimates that agreed with experiment. This further gave evidence of the importance of the ESL's resistance to both flow (hydraulic resistivity) and compression (osmotic pressure difference).

In addition to the previously mentioned studies, models have been used in many other contexts to better understand partitioning behavior at bifurcations and the effects of the ESL. Barber et al. [26] used a similar model to the one used here to find that cell-cell interactions for lower hematocrits made partitioning more uniform, in general. Such interactions were identified in three main categories: trade-off interactions, herding interactions, and following interactions. Trade-off interactions, the more prevalent of the three main types, produced more uniform partitioning overall, while herding and following interactions promoted less uniform partitioning. Trade-off interactions happen when the leading cell entering a daughter branch causes the following cell to enter the alternative branch. When the front cell enters one branch, it effectively carries a lot of volume with it into that branch. To maintain the flow split in the bifurcation (e.g. 25% out one daughter branch and 75% in the other daughter branch), the back cell enters the opposite branch. Herding interactions happen when the following cell entering a daughter branch causes the leading cell to enter the same branch. Similarly, following interactions are described as when the leading cell entering a daughter branch causes the following cell to enter the same branch. In both cases, this is caused by the cells being very close together which, in turn, causes the cells to move as a single object.

Balogh and Bagchi [27] used a model to study a large three-dimensional network of vessels featuring multiple successive bifurcations, both converging and diverging, and many RBCs to identify underlying cellular scale mechanisms including reverse partitioning. In classical RBC partitioning, the high flow branch gets disproportionately more cells than the low flow branch. In contrast, in reverse partitioning the low flow branch gets disproportionately more

cells than the high flow branch. They identify two main cell mechanisms that are responsible for increased reverse partitioning: asymmetry in the RBC distribution upstream of diverging vessel bifurcations and temporary and fluctuating increases in the RBC concentration near diverging bifurcations. Asymmetry in RBC distributions arises due to the partitioning behavior at previously encountered bifurcations and is more likely to affect partitioning in series of bifurcations in relatively close succession. In cases of increased concentration of cells near bifurcations, reverse partitioning arises due to a mechanism analogous to the previously described trade-off interactions.

Damiano [28] used mixture theory to model the ESL as a linearly elastic solid under deformation. He found that the presence of the ESL contributed to a significant increase in resistance and reduction in hematocrit in capillary tubes. These results matched qualitatively with experimental results. Hariprasad and Secomb [29] later modeled the effect of the ESL on RBC shapes. They found that the ESL led to two different possible steady state shapes that might result as they travel along the tube. These differences were observed for differing values of the hydraulic resistivity in the ESL chosen from a range of physiologically realistic values. Despite these efforts, such studies do not consider both the ESL and RBC partitioning in conjunction.

A wide range of numerical methods have been used to develop models of RBCs in microvessel flows [30]. Fedosov et al. [31] used dissipative particle dynamics (DPD) to reproduce experimental results. In this case, the system comprised of RBC membrane, external plasma, and internal cytoplasm was modeled mesoscopically by stochastic particles. DPD methods generally require large numbers of particles to accurately represent RBCs and their dynamics in high resolution. Lattice-Boltzman methods, such as those used by Sun and Munn [32] to investigate cellular interactions, yield the mechanics of the Navier-Stokes equations in a statistical limit. However, this statistical description of the flow equations depends upon a microscopic viscous relaxation timescale. Thus, as the Reynolds number of the system decreases, computation time increases dramatically. Immersed boundary methods distribute forces exerted on the plasma by the cell membrane to a local mesh of nearby points. However, these methods depend on the refinement of the mesh to resolve close cell-cell interactions, and additional care must be taken if cells are closer than a mesh spacing distance from

17

one another [33], [34]. Finite element methods, such as the one detailed in Chapter 2, explicitly model the cell membrane which provides insight into cell mechanics. Close cell-cell interactions are handled by invoking lubrication theory. For the scenarios considered in this dissertation, finite element methods require fewer nodes and less computational expense to achieve a desired degree of accuracy compared to other methods. The finite element model described in Chapter 2 utilizes twenty nodes along the discretized membrane of the RBC. Simulations run with forty nodes produced similar results. However, computational expense increases significantly with the addition of each node indicating that other methods should be utilized to simulate RBCs in higher hematocrit scenarios or in three dimensions.

Here we consider both the ESL and RBC partitioning using a two-dimensional mechanical model of single and paired cells passing through a diverging capillary bifurcation. To maintain a feasible study, the focus here is restricted to three major aspects of RBC dynamics in a single diverging capillary bifurcation. Other aspects, such as oxygen release, can and do occur but are not considered with the model presented here. The first major aspect is the partitioning of RBCs into one or the other downstream daughter branch. The second major aspect is the deformation of cells as they pass through the bifurcation. The third is how deeply the RBCs penetrate the ESL (ESL penetration) when they encounter the ESL.

As previously mentioned, RBC partitioning can affect the distribution of RBCs, and other blood constituents, throughout the microvasculature. Mechanical deformation of RBCs has been linked to release of various metabolites including adenosine triphosphate (ATP) and nitric oxide (NO). Bor-Kuckatay et al. [35] devised an experimental study *in vitro* that showed a significant link between NO concentration and RBC deformability as quantified by an elongation index. Following experimental studies by Forsyth et al. [36], [37], Zhang et al. [38] developed a model that predicts ATP release by the level of shear stress experienced in the cell membrane as well as its change in curvature. They predicted that the highest rates of these factors are observed in diverging bifurcations, indicating that the highest rates of ATP release are located at vessel bifurcations as well.

ESL penetration is particularly important for cell adhesion. ESL penetration by RBCs has been seen to occur in experiment in certain pathological scenarios involving thrombosis and cardiovascular disease where the ESL can be damaged [39], [40]. According to Vink et

al. [7], a damaged or reduced ESL will lead to RBC adhesion. They devised an experiment *in vivo* that showed how oxidized low-density lipoproteins reduce the gap between RBCs and endothelial cells (ECs), a measure of ESL damage with a smaller gap suggesting evidence of a damaged ESL. The estimated level of damage experienced by the ESL correlated directly with the number of RBCs observed to adhere to the EC surface. Cell adhesion can, in turn, lead to RBC damage and impaired RBC function [7]. Damaged or reduced ESL, as in the studies by Oberleithner et al. [9], [41], can also lead to an increase in interactions between RBCs and ECs via endothelial structures such as epithelial sodium channels.

Secomb et al. [42] developed a two-dimensional viscoelastic model similar to the one used in these studies. It reproduced the physiological shape of an RBC as it passed along a bifurcation made up of smooth vessels. The two-dimensional model, including internal viscous elements within the RBC membrane, was calibrated to match the motion and deformation experienced by cells rotating in shear flow. Barber et al. produced results consistent with a partitioning function empirically and experimentally derived by Pries [43] for both a single RBC [15] and two interacting RBCs [26], for vessels with no ESL.

The model developed in this dissertation, however, suggests that varying the hydraulic resistivity and osmotic pressure difference between the ESL and the free flowing region (referred to as the "osmotic pressure difference in the ESL", or simply as the "osmotic pressure difference" henceforth) does have a significant impact on the level of deformation undergone by an RBC. In addition, we show that physiologically realistic parameters of hydraulic resistivity and osmotic pressure within the ESL lead to sufficient penetration by RBCs at diverging vessel bifurcations for possible cell adhesion to take place in these scenarios.

The computational model used in simulations throughout these studies is developed in Chapter 2. Modeling of the ESL is similar to methods devised by Secomb and Hariprasad [23], [29]. Modeling of RBC motion in viscous flow is similar to models formulated by Secomb and Barber [15], [26], [42]. It contains improvements and added capabilities that increase computational efficiency and produce accurate results for situations not considered by previous models. These improvements include modeling ESL penetration by an RBC in vessel bifurcations and an expanded capability to resolve close cell-cell interactions through the application of lubrication theory, among others.

The model is first used to consider individual RBCs traveling through an ESL lined bifurcation in Chapter 3. By removing cell-cell interactions, the effect of the ESL on cell dynamics may be analyzed more closely. Decreased values of these parameters lead to more nonuniform RBC partitioning, decreased RBC deformation and increased cell penetration. Possible mechanical explanations for these phenomena are explored.

In Chapter 4, the further effect of the ESL on cell-cell interactions in bifurcations is considered. These results are compared to the single cell data as well as cell-cell interaction data from a smooth bifurcation to more clearly identify trends. The presence of an additional RBC in the bifurcation tends to increase deformation and ESL penetration across various values of the hydraulic resistivity and osmotic pressure parameters. However, RBC partitioning for different parameter values in the ESL can both increase and decrease uniformity due to various mechanical effects which are also explored.

2. MODELING TWO-DIMENSIONAL RED BLOOD CELL DYNAMICS IN A CAPILLARY BIFURCATION LINED WITH POROUS MEDIA

The following subsections detail the computational model used throughout this dissertation to perform simulations involving red blood cells (RBCs) at a diverging microvessel bifurcation. The two-dimensional model of the RBC as a network of viscoelastic elements immersed in a surrounding fluid was described previously by Barber et al. [26], and is given in section 2.1. The added model of the endothelial surface layer (ESL) as a porous media that resists compression combines approaches from work by Hariprasad and Secomb [29] and Secomb et al. [23]. The blood vessel bifurcation configuration used here is shown in Figure 2.2a and was chosen to approximately match the vessel geometries used in Barber [15] and Hariprasad and Secomb [29]. Detailed in section 2.2 is how a finite element program, FlexPDE [44], is used to solve the coupled fluid and solid equations for membrane velocities at each time step. The adaptive time integration method used takes those velocities to predict the trajectories of each RBC. Involved in the calculation of the membrane velocities is the use of lubrication forces, described in section 2.3, to account for cells in close proximity to other objects. Section 2.4 defines the various parameter values involved in simulations, section 2.5 gives reasons for premature simulation termination, and section 2.6 highlights the central challenges that arose from the numerical method and mathematical formulation of the model.

2.1 Mathematical Modeling

The fluid in the microvessel bifurcation is modeled using a combination of equations for viscous flow for the free flowing plasma and for porous media flow for the fluid in the ESL, respectively. The RBC traveling in the fluid is modeled using a network of viscoelastic and purely viscous elements. To couple these models together, we employ equations of membrane or mechanical equilibrium.

2.1.1 Modeling Fluid Flow

The suspending medium in the non-ESL region is assumed to be an incompressible fluid with a low Reynolds number so that the flow is well approximated by the Stokes flow equations:

$$\boldsymbol{\nabla} \cdot \boldsymbol{\sigma} = 0; \quad \boldsymbol{\nabla} \cdot \boldsymbol{u} = 0, \tag{2.1}$$

where $\boldsymbol{u} = (u(x,y), v(x,y))$ is the two-dimensional velocity field and the corresponding components of stress are:

$$\boldsymbol{\sigma} = \mu(\nabla \boldsymbol{u} + \nabla \boldsymbol{u}^T) - p\boldsymbol{I}. \tag{2.2}$$

μ is the dynamic fluid viscosity, $\boldsymbol{I}$ is the identity matrix of dimension 2, and $p(x,y)$ is the pressure field. The Reynolds number, the ratio of inertial forces to viscous forces in a fluid, is estimated using:

$$\mathrm{Re} = \frac{\rho U_c L_c}{\mu}, \tag{2.3}$$

where ρ is the density of the fluid, U_c is the characteristic velocity of the system, and L_c is the characteristic length scale of the system. Using $\rho = 1.025$ g/cm^3, $U_c = 0.1$ cm/s, $L_c = 0.0008$ cm, and $\mu = 0.012$ dyn·s/cm^2 for the density of plasma, the average velocity of an RBC, the average diameter of an RBC, and the dynamic viscosity of plasma, respectively, yields Re $\approx 0.0068 \ll 1$. This indicates that viscous forces dominate in the system and so inertial forces are ignored and the Stokes flow, instead of Navier-Stokes, equations are used.

Following past work by Secomb et al. [23] and Hariprasad et al. [29], the flow in the ESL is modeled by assuming the layer acts as a porous medium that has a relatively high hydraulic resistivity and a width that is roughly $w = 1$ µm. In particular, a Brinkman approximation [45] models the flow in the ESL by introducing drag on the fluid in the porous media that is proportional to the fluid's velocity:

$$\boldsymbol{\nabla} \cdot \boldsymbol{\sigma} = \kappa_v(d)\boldsymbol{u}. \tag{2.4}$$
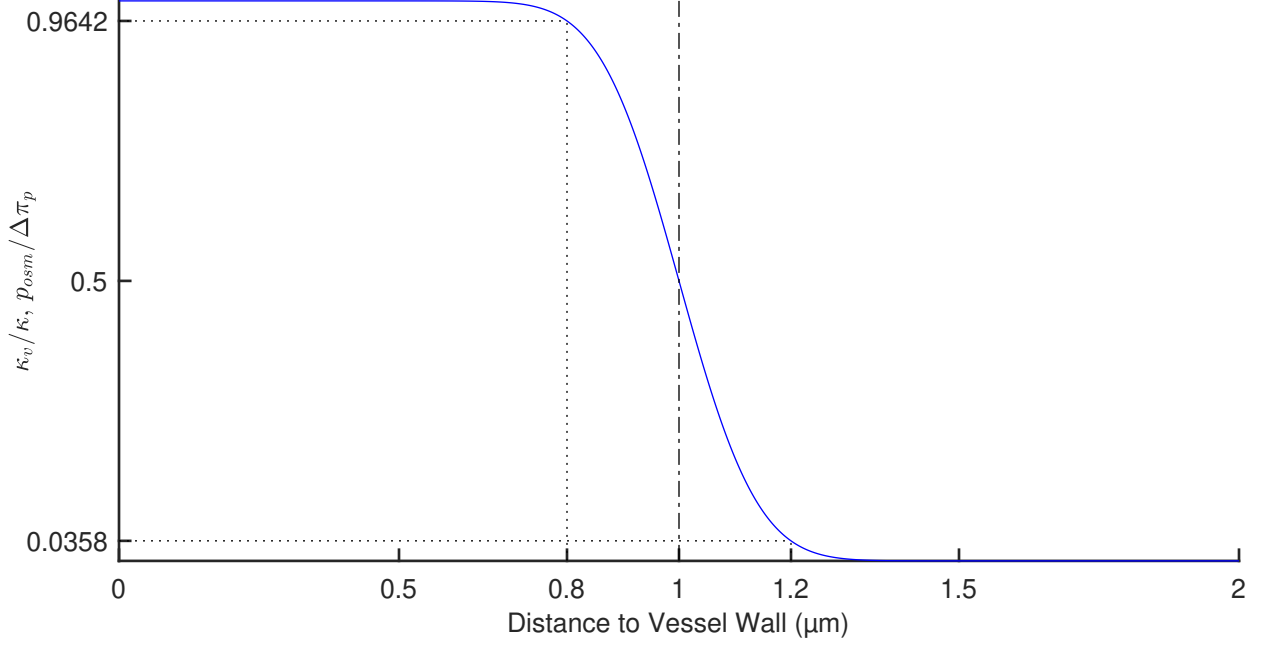
Figure 2.1. Assumed variation of hydraulic resistivity, κ, and osmotic pressure difference, $\Delta\pi_p$ within the ESL. Both are plotted against distance to the vessel wall, d. The dashed line indicates the ideal boundary between the free flowing plasma region and the ESL region. $> 96.4\%$ of the magnitude of the specified resistance or pressure is felt 0.2 µm past the ideal boundary.

The hydraulic resistivity $\kappa_v(d)$ is assumed to depend on the distance to the vessel wall, d, and is given by:

$$\kappa_v(d) = \kappa \frac{1}{2} \text{erfc}\left(\frac{d - w}{L}\right), \tag{2.5}$$

where κ is the maximum hydraulic resistivity in the ESL, erfc() denotes the complementary error function, and $L = 0.157$ determines the width of the diffuse ESL boundary, as illustrated in Figure 2.1.

The value of L was chosen by Secomb et al. [23] so that most of the variation in $\kappa_v(d)$ occurs over a distance of around 0.4 µm, which was shown to produce realistic vessel flow resistance estimates. Accordingly, within $w - 0.4/2 = 0.8$ µm of the vessel wall, $\kappa_v(d)$ is an approximately constant value which is $> 96.4\%$ the magnitude of the specified κ value and porous flow occurs. Similarly, $\kappa_v(d)$ is approximately zero ($< 3.6\%$ the magnitude of κ) further than $w + 0.4/2 = 1.2$ µm away from the wall and Stokes flow occurs. This choice of modeling the hydraulic resistivity (and ESL osmotic pressure, discussed later) as a diffuse

boundary rather than a sharp one was made both because it produces smoother dynamics in the ESL region allowing for larger time steps and faster simulations, and because simulations run with a sharp ESL boundary produced similar, yet less smooth, results, indicating that the choice of ESL boundary representation is relatively unimportant.

The fluid domain is pictured in Figure 2.2a with flow coming in on the left through the larger mother vessel and flow exiting out two daughter vessels on the right. The origin is located at the intersection of the centerlines of the mother vessel and the two daughter branches. The labeled arrows at the origin show the direction of the positive x and y coordinates. The length of each vessel is measured from the origin along the vessel centerline to the vessel inlet or outlet and are taken initially as $VL_0 = VL_1 = VL_2 = 5(w_0 - w)/2$, which is consistent with [15]. To limit the effects the choice of boundary conditions may have on RBC dynamics, the length of daughter branch i, where $i = 1$ or 2, is given by $VL_i = \max(5(w_0 - w)/2, 5 - R_{cell}/2 + D_i)$. D_i is the distance that the RBC has traveled down daughter branch i defined by $D_i = \max_j \left| \langle x_j, y_j \rangle \cdot \left((-1)^{i-1} \left\langle 1/\sqrt{2}, 1/\sqrt{2} \right\rangle \right) \right|$ where $\langle x_j, y_j \rangle$ is the jth cell node. This prevents the cells from getting close to the outlets.

The inlet normal derivative of the velocity is set to zero, corresponding to an assumption of well-developed flow at the entrance. The velocity and normal derivative of pressure at the outlets are prescribed to match the flow profile for well-developed flow in a tube with a $w = 1$ µm thick porous layer along its walls. The inlet pressure is set to zero. As described in more detail in section 2.2, a penalty method involving pressure is used in order to enforce the fluid incompressibility condition, which cannot be specified exactly by the finite element solver. The boundary conditions of the pressure at the inlet and outlets stated above are the correct conditions when using such a penalty pressure method as well as steady Stokes flow.

The flow profile and normal pressure derivative at the outlets are derived from equation 2.4, as follows. Consider for a moment well-developed, unidirectional flow in a vessel that is horizontal. The original equation simplifies to:

$$\mu \frac{\partial^2 u}{\partial y^2} = \frac{dp}{dx} + \frac{1}{2} \kappa \operatorname{erfc} \left(\frac{w_0/2 - |y| - w}{L} \right) u. \tag{2.6}$$

While this equation can be solved using, for instance, a standard boundary value problem solver (see Figure 2.3), it can be difficult to use this solution to supply boundary conditions for our finite element solver, FlexPDE. Because of this, we used alternate boundary conditions found by considering well-developed, unidirectional flow in a horizontally oriented vessel with $w = 1$ µm and a sharp boundary.

More precisely, the equations governing the horizontal velocity, $u(y)$, in the case of a sharp boundary are given by:

$$\mu \frac{\partial^2 u}{\partial y^2} - \frac{dp}{dx} = \begin{cases} \kappa u & w_0/2 - |y| - w < 0; \text{ porous layers} \\ 0 & w_0/2 - |y| - w > 0; \text{ free flowing region} \end{cases} . \tag{2.7}$$

The following boundary equations are used to solve these equations:

$$u_{b,por}\left(-\frac{w_0}{2}\right) = 0; \qquad u_{b,por}\left(-\frac{w_0}{2} + w\right) = u_{b,free}\left(-\frac{w_0}{2} + w\right);$$
$$\frac{du_{b,por}}{dy}\left(-\frac{w_0}{2} + w\right) = \frac{du_{b,free}}{dy}\left(-\frac{w_0}{2} + w\right); \qquad \frac{du_{b,free}}{dy}(0) = 0, \tag{2.8}$$

where $u_{b,por}(y)$ and $u_{b,free}(y)$ denote $u_b(y)$ in the porous layers and in the free flowing region, respectively. The first of these expressions corresponds to a no-slip boundary condition at the vessel wall, the second and third to boundary conditions enforcing a continuous, differentiable flow across the boundary between the ESL and the free flowing region, and the last to ensuring a finite maximum velocity at the center of the vessel, a consequence of the symmetry of this scenario. The solution, for $\kappa = 10^8$ dyn·s/cm^4, is plotted in red in Figure 2.3.

The difference between the diffuse and sharp boundary flow profiles is highest for the high flow daughter branch at high ($\kappa = 10^8$ dyn·s/cm^4) hydraulic resistivity (Figure 2.3). For this case, the percent relative error is approximately 2.66%, calculated with the following formula:

$$\% \text{ relative error} = \frac{\int |f_1(x) - f_2(x)| \, dx}{\int |f_1(x)| \, dx}. \tag{2.9}$$

25
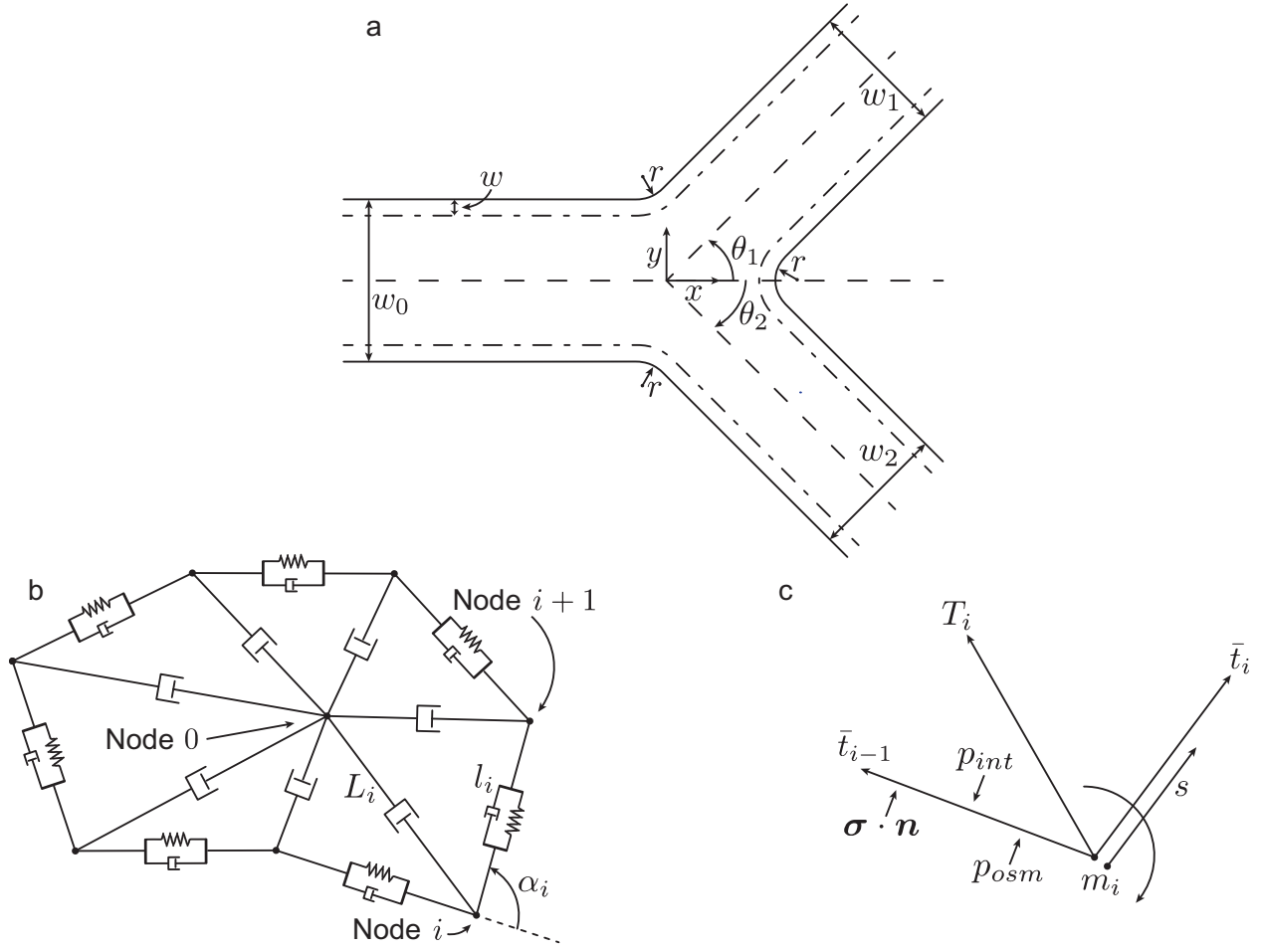
Figure 2.2. **(a)** Geometry of the fluid domain with vessel widths of $w_0 = 10$ µm and $w_1 = w_2 \approx 8.35$ µm including an ESL width of $w = 1$ µm. Daughter branches bifurcate at $\theta_1 = \theta_2 = 45°$ angles from the mother vessel. The radii of the circular arcs that link the vessel walls in the bifurcation are all $r = 2$ µm. The x-axis runs parallel to the centerline of the mother vessel, while the y-axis runs perpendicular. **(b)** Diagram of the two-dimensional model of a discretized RBC. Exterior line segments are comprised of viscoelastic elements of length l_i while interior elements of length L_i are purely viscous. **(c)** Summary of forces acting on the ith node of the discretized cell including membrane tensions ($\bar{t}_{i-1}$ and $\bar{t}_i$), bending resistance (m_i), internal viscous resistances (T_i), internal pressure (p_{int}), external fluid ($\boldsymbol{\sigma} \cdot \boldsymbol{n}$) and ESL ($p_{osm}$) forces. Also included is the arclength s that gives the distance from Node i along the ith external element and is used when calculating force balances for each node.

Figure 2.3. The fluid velocity out of an 8.35 µm wide vessel (same as daughter branches) when using sharp (red) and diffuse (blue) porous layer boundary assumptions. Hydraulic resistivity in the layer is high ($\kappa = 10^8$ dyn·s/cm^4) and flow is 0.575 times the flow in the mother daughter vessels (8 µm^2/ms) used in these studies. Percent relative error between the two methods is approximately 2.66%.

However, since the outlets are always at least $5 - R_{cell}/2$ µm from the RBC, the percent relative error in RBC velocities caused by using the approximate flow profile over the exact flow profile never exceeds 0.0249%.

Choice of geometry dimensions and daughter branch orientation in simulations as well as total vessel flux are discussed in section 3.2.

2.1.2 Modeling Red Blood Cells

The two-dimensional RBC model represents a cross-section through the center of the cell. It is discretized into a loop of n external nodes connected by n external line segments and to n internal line segments that connect to a single internal node (Figure 2.2b). Using $n = 20$ produces results that agree with experiment. These results include flow resistance in capillary vessels [42], typical bifurcation motion for isolated [15] and paired cells [26], and shear effects on cell shape in ESL-lined capillary tubes [29] (see Chapter 1 for more

details). A subset of the simulations used to produce the results in this dissertation were run with $n = 40$. No significant differences in RBC motion was observed. To represent the membrane's viscoelastic resistance to deformation, each external segment is modeled as a viscous and an elastic component connected in parallel. To represent the membrane's resistance to bending, a bending moment is introduced at each external node between each external segment. The effects of the internal viscosity of the cell as well as the viscous resistance of the cell membrane to out-of-plane deformations are represented using solely viscous internal segments.

The ith external node at position $\boldsymbol{x}_i$ is connected to the ith internal segment and external segments labeled $i - 1$ and i. The internal node is labeled as Node 0. During deformation, the ith external segment experiences a tension force, $t_i(s)$, a shear force, $q_i(s)$, and a bending moment, $m_i(s)$, where s is the distance along the element from node i toward node $i + 1$, l_i is the length of the ith external segment, and $0 \leq s \leq l_i$.

In addition to external fluid forces, the model also takes into account ESL-mediated forces that arise when an RBC impinges upon the ESL, which corresponds physiologically to an RBC compressing the layer. Pries et al. [5] assumed that the ESL exhibits slightly elevated colloid osmotic pressure due to the adsorption of plasma protein molecules. Following Secomb et al. [23], this difference in osmotic pressure is modeled in the same way as the hydraulic resistivity:

$$ p_{osm} = \Delta \pi_p \frac{1}{2} \text{erfc} \left(\frac{d - w}{L} \right), \tag{2.10} $$

where $\Delta \pi_p$ is a constant corresponding to the maximum difference in osmotic pressure between the ESL region and the vessel lumen. p_{osm} does not affect fluid flow and so is not included in the fluid equations. It does exert an additional pressure on portions of the RBC membrane that penetrate the ESL due to the osmotic or resistive forces in the compacted region which push the RBCs away from the vessel wall (see equation 2.16).

In experiments, visible cross-sectional areas can and do fluctuate. Two-dimensional models that use incompressible fluid equations to model the cell interior cannot reproduce such behavior. This model, however, represents the cell interior with viscous internal segments and an internal pressure. This choice has allowed the model to reproduce experimental be-

28

havior in a number of contexts including comparisons with experimental pictures of RBC cross-sections [15], [42]. At the same time, however, in three dimensions RBC volume is conserved due to internal fluid incompressibility and RBC surface area is conserved over the time scales considered here. These properties cause the cross-sectional areas of RBCs to conform to approximate, not exact, area conservation, and so the cross-sectional area is constrained by introducing a pressure to the interior of the cell:

$$p_{int} = k_p \left(1 - \frac{A}{A_{ref}} \right)$$
(2.11)

where k_p is a constant giving the strength with which the approximate area conservation is enforced and A_{ref} is a constant reference area of the RBC.

The average tension in the ith external segment is given by:

$$\bar{t}_i = k_t \left(\frac{l_i}{l_0} - 1 \right) + \mu_{\text{ext}} \frac{1}{l_i} \frac{dl_i}{dt}$$
(2.12)

where k_t is the elastic modulus, l_0 is the reference length of the segment, and μ_{ext} is the segment viscosity. The first and second terms on the right hand side of the equation correspond to the elastic and viscous components of the element, respectively. Linear elastic elements and viscous elements that are linear with respect to dl_i/dt are used for simplicity. The internal segments are purely viscous with the average tension in the ith internal segment given by:

$$T_i = \mu_{int} \frac{1}{L_i} \frac{dL_i}{dt}$$
(2.13)

where μ_{int} is the viscosity and L_i is the length of the ith internal segment.

The resistance of the cell membrane to bending can be modeled by including bending moments at each external node:

$$m_i = -\frac{k_b \alpha_i}{l_0}$$
(2.14)

where k_b is the bending modulus and α_i is the exterior angle between the external segments $i - 1$ and i.

2.1.3 Model Coupling

The coupling of the cell membrane stresses with the external stresses are given by the following equations of membrane or mechanical equilibria [46]:

$$\frac{dt_i}{ds} = -g_i; \quad \frac{dq_i}{ds} = -f_i; \quad \frac{dm_i}{ds} = q_i \tag{2.15}$$

where $g_i(s)$ and $f_i(s)$ are the tangential and normal components of the external stresses, respectively, $t_i(s)$ is the tension force, $q_i(s)$ is the shear force, and $m_i(s)$ is the bending moment at the ith external node.

The external fluid stresses, osmotic pressure difference, and interior pressure combine to give the following equation for the fluid stresses acting upon the ith external segment:

$$g_i = \boldsymbol{t}_i^T \cdot \boldsymbol{\sigma} \cdot \boldsymbol{n}_i; \quad f_i = \boldsymbol{n}_i^T \cdot \boldsymbol{\sigma} \cdot \boldsymbol{n}_i + p_{int} - p_{osm} \tag{2.16}$$

where $\boldsymbol{n}_i$ and $\boldsymbol{t}_i$ are the unit vectors normal and tangential to the ith external segment and point away from and counterclockwise to the cell interior, respectively. When g_i is a positive value, the fluid pulls on the cell membrane in a counterclockwise direction while a positive value of f_i corresponds to the fluid pulling the membrane outward.

Integrating the mechanical equilibrium equation for the bending moment in equations 2.15 above produces an equation for the average shear stress, $\bar{q}_i$, in the ith external segment in terms of the exterior angles, α_i and α_{i+1}, at either end of the segment:

$$\bar{q}_i = \frac{k_b(\alpha_i - \alpha_{i+1})}{l_i l_0} \tag{2.17}$$

By further integration and manipulation of the remaining equations of mechanical equilibria, we can write expressions for the forces acting on the endpoints of the external segments:

$$t_i(0) = \bar{t}_i + \frac{1}{l_i} \int_0^{l_i} (l_i - s) g_i(s) ds; \quad t_i(l_i) = \bar{t}_i - \frac{1}{l_i} \int_0^{l_i} s g_i(s) ds;$$

$$q_i(0) = \bar{q}_i + \frac{1}{l_i} \int_0^{l_i} (l_i - s) f_i(s) ds; \quad q_i(l_i) = \bar{q}_i - \frac{1}{l_i} \int_0^{l_i} s f_i(s) ds. \tag{2.18}$$

30

The internal segments are not acted upon by any fluid.

At the ith external node, the equilibrium of forces can be written as follows:

$$t_i(0)\boldsymbol{t}_i - t_{i-1}(l_{i-1})\boldsymbol{t}_{i-1} - q_i(0)\boldsymbol{n}_i + q_{i-1}(l_{i-1})\boldsymbol{n}_{i-1} + T_i\boldsymbol{T}_i + \boldsymbol{f}_{i,lub} = 0 \qquad (2.19)$$

where $\boldsymbol{T}_i$ is the unit vector pointing into the cell interior along the ith internal segment and $\boldsymbol{f}_{i,lub}$ are additional lubrication forces that are set to zero unless a cell node or segment is within $\delta_{lub} = 0.01$ μm from another cell or vessel boundary segment. These forces are detailed further in section 2.2. Equilibrating forces at the internal node yields:

$$\sum_{i=1}^{n} T_i\boldsymbol{T}_i = 0. \qquad (2.20)$$

These nodal equations 2.19 and 2.20 form a system of $2(n+1) = 42$ equations for each RBC. They describe the balance of forces at each node and produce equations that are linear in terms of the unknowns in the system that include velocities, $\{\boldsymbol{u}_{i=0}^{n}\}$, at each node and nearby fluid velocities and pressures.

The equations are also coupled to the surrounding fluid by enforcing no-slip boundary conditions at the cell membrane. The velocity of the membrane along the ith external segment, $\boldsymbol{u}_m(s)$, is estimated using linear interpolation and the unknown membrane nodal velocities:

$$\boldsymbol{u}_m(s) = \frac{l_i - s}{l_i}\boldsymbol{u}_i + \frac{s}{l_i}\boldsymbol{u}_{i+1} \qquad (2.21)$$

The fluid velocities along the membrane are required to match these interpolated membrane velocities which produce boundary conditions for the fluid on the cell boundary that involve the $2(n + 1)$ unknown membrane nodal velocities.

The resulting coupled fluid-nodal equations involve both unknown membrane nodal velocities and unknown fluid velocities and pressures. These coupled equations are solved numerically to obtain estimates for all unknown velocities at that particular time step. The membrane nodal velocities that are found in this way can then be used to obtain the long-term motion of the RBCs.

2.2 Numerical Method

The coupled system of equations describing the motion of RBCs and the surrounding plasma is solved using the finite element package FlexPDE [44]. FlexPDE uses a variational formulation. Each of the variables in the system is approximated by a linear combination of cubic basis functions making the spatial solution third order accurate. Adding such sums into the equations, multiplying by a test function (also cubic), and integrating by parts produces the corresponding variational formulation for the problem. The underlying equation involving a stiffness matrix and its load vector is solved using Lanczos iteration [47]. The solvers utilized by FlexPDE are structured in such a way that the incompressibility condition $\boldsymbol{\nabla} \cdot \boldsymbol{u} = 0$ cannot be specified exactly. Instead, the following condition is used:

$$\nabla^2 p = K \boldsymbol{\nabla} \cdot \boldsymbol{u}. \tag{2.22}$$

The penalty coefficient is chosen so that $K = \mu/L_{char}^2 = 1 \times 10^{-2}/(1 \times 10^{-5})^2 = 1 \times 10^8$ dyn·s/cm⁴, where $L_{char} = 1 \times 10^{-5}$ cm $= 0.1$ µm is the approximate length scale of incompressibility resolution. This value was found to sufficiently approximate the incompressibility of the fluid when the nodes and segments comprising the RBCs were a distance on the order of 0.1 µm from each other and the vessel wall [15], [42].

However, during simulations, RBCs may be forced into close proximity with each other and, in the cases considered with no ESL or impermeable ESL, to the boundary of the domain. When a porous ESL region is present, RBCs are never within approximately 0.1 µm of the vessel walls, as the hydraulic resistivity and osmotic pressure difference in the ESL are sufficient to prevent such penetration into the layer (see section 3.3). The adaptive mesh generator utilized by FlexPDE helps better resolve flow when cells are in close proximity with other rigid objects by creating an increasingly refined mesh in the narrow channels between RBCs and other objects. The adaptive meshing also automatically refines the mesh near the ESL's diffuse boundary where the hydraulic resistivity and osmotic pressure difference values change rapidly. In particular, the mesh is refined until estimated local relative errors are less than 1×10^{-3}.

In extreme cases where RBCs are within 0.01 μm of each other or the vessel wall, or $\ll L_{char} = 0.1$ μm, the penalty condition is unable to appropriately enforce incompressibility in the fluid. This results in cells that unrealistically collide in finite time with each other or the vessel wall. In fact, when RBCs and endothelial cells are close enough to each other, the surface roughness on the cells begin to produce solid-solid interactions with each other that limit how close those cells can be. For instance, the surface roughness of the RBCs includes the presence of a glycocalyx that protrudes from the membrane approximately 0.01 μm [48]. To prevent unrealistic collisions, lubrication theory is used to derive correction forces that are used at nodes in close proximity to other objects, as described in section 2.3.

Given the cell node positions, $\boldsymbol{y}_i^n$, at the nth time step at time t^n, the finite-element package is used to find the instantaneous velocity $\boldsymbol{u}_i^n$ of the ith cell node at that time. The velocities are used to predict the nodal positions, $\widetilde{\boldsymbol{y}}_i$, at time $t^n + dt_p$ using a forward Euler estimate:

$$\widetilde{\boldsymbol{y}}_i^{n+1}(t^n + dt_p) = \boldsymbol{y}_i^n + dt_p \boldsymbol{u}_i^n, \tag{2.23}$$

where dt_p is the predictor time step that can vary as the simulation progresses. The finite element program is then used with these new positions to estimate the corresponding instantaneous velocities at time $t^n + dt_p$, denoted by $\widetilde{\boldsymbol{u}}_i^n(t^n + dt_p)$. The corrected estimate of the nodal position at time $t^{n+1} = t^n + dt_c$ is given by:

$$\boldsymbol{y}_i^{n+1}(t^n + dt_c) = \boldsymbol{y}_i^n + \frac{dt_c}{2dt_p} \left[(2dt_p - dt_c)\boldsymbol{u}_i^n + dt_c\widetilde{\boldsymbol{u}}_i^n(t^n + dt_p) \right], \tag{2.24}$$

where dt_c is the corrector time step that can vary as the simulation progresses. Note that if the predictor and corrector time steps are equal to each other, this method is the same as Heun's method. However, the time steps are adaptive and so are usually different sizes. In this case, the method has $\mathcal{O}(dt_c^2) + \mathcal{O}(dt_p dt_c)$ global accuracy, and has the same stability region in terms of dt_c as Heun's method.

Using a constant time step frequently produces unrealistic and nonphysiological scenarios where cell and/or domain boundaries may overlap. The integration with respect to time is therefore performed using an adaptive second order Runge-Kutta scheme where the time step

is chosen so that the minimum distance between any two objects (e.g. between two RBCs or between a RBC and the wall) changes by no more than a set percentage. In addition, to better resolve motion in and through the ESL, that percentage is chosen to depend on RBC proximity to the ESL. In particular, when a portion of a cell is within $w = 1$ μm of the vessel wall (where hydraulic resistivity and osmotic pressure differences are at 50%), the cell is considered to be in the "ESL region". Otherwise, it is outside the region. When the ESL is present, the time step is chosen so that minimum relative distance changes by no more than 10% when the cells are not in the ESL region and 1% when they are. When the ESL is not present, minimum relative distance changes are limited to 10% throughout the domain. The time steps were additionally limited so that no single time step never exceeded 1 ms. These adaptive additions improve numerical accuracy and sufficiently reduce the size of time steps so that simulations do not change significantly when the time steps are reduced in size even further.

At the center of implementing two discrete adaptive time integration rules in the domain, 10% in the free flowing plasma region and 1% in the ESL region, is finding the distance from a cell to the vessel wall. The distance to the vessel wall is the minimum distance from any point on the cell membrane, parametrized by the curve $\boldsymbol{RBC}(t_{RBC})$, to any point on the vessel wall, parametrized by the curve $\boldsymbol{VW}(t_{VW})$: $\min\limits_{t_{VW}, t_{RBC}} ||\boldsymbol{VW}(t_{VW}) - \boldsymbol{RBC}(t_{RBC})||_2$. In general, the function $||\boldsymbol{VW}(t_{VW}) - \boldsymbol{RBC}(t_{RBC})||_2$ can have multiple local minima corresponding to more than one location on the cell being close to the vessel wall (for an example of this, see Figure 4.9). In addition, the problem is made more difficult because the goal is to find the minimum distance to all of three disparate sections of the vessel wall. While there are many ways to proceed, we solved the minimization problem using a program that finds the distance from a polygon (cell) to a point in space, a program that finds minimums (Matlab's fminbnd), and a partitioning of parametrized curves into much smaller curve segments.

The first program finds the minimum distance from a point, P, in space to a particular polygon by taking the minimum of all minimum distances from P to each of the lines that pass through the edges of the polygon by using a dot product projection. If the projected point on the line, S, lies on the edge, this is also the minimum distance to that edge. However, if S does not lie on the edge, the distance from P to the nearest endpoint of the edge is used

instead. This distance program can be thought of as a function that returns the distance from the cell to any point in space, including points on the ESL boundary or vessel wall: $D_{cell}(x,y)$. Before continuing, we note that there are three distinct sections of the border between the free flowing plasma region and the ESL region, as seen in the bifurcation domain pictured in 2.2a, one for the top, bottom, and rightmost vessel wall. These are parameterized in terms of t_i and denoted by $\boldsymbol{VW}_i(t_i) = \langle x(t_i), y(t_i) \rangle$ for $i = 1, 2, 3$. Matlab's fminbnd is first used to find an estimate for typical local minimum values, $\tilde{m}_i$, along each of these three boundaries:

$$\tilde{m}_i = \min_{t_i \in [t_{i,min}, t_{i,max}]} D_{cell}(\boldsymbol{VW}_i(t_i)). \tag{2.25}$$

When $\tilde{m}_i$ is less than 1.1 µm away from the vessel wall or less than 2 µm away from the wall while also being one of the two walls closest to the cell, more care is taken in finding the distance. In such cases the boundaries were broken into smaller pieces no longer than half the minimum external segment length, $l_{\min}$. Matlab's fminbnd is again used to find local minimums on each of those smaller segments. On such small intervals when only one cell node is close (within $l_{\min}/2$) to any given small segment, all possible local minima on the portion of wall being tested are found. Each of the local minimums found as solutions to these minimization problems are compared and the smallest value yields the global minimum. Note that technically if cells become twisted enough, the preceding algorithm may fail to find all local minima and the correct corresponding global minima. All simulations, however, were checked by eye to ensure no such abnormal situations occurred.

In a previous study by Barber and Zhu [49] regarding cancer cells, a similarly adaptive time integration technique was employed and produced good results. But rather than using a second order Runge-Kutta method, a second order Adams-Bashforth method was used in the study. However, applied to the scenarios involving RBCs in diverging bifurcations described here, preliminary tests showed a relatively high number of simulations breaking before a branching determination could be made. Upon closer inspection, a possible explanation for these breakages could be an increased tendency for segments to exhibit unstable buckling behavior when in bifurcations. Segments and nodes in series would develop a zig-zag pattern along a cell membrane and then oscillate back and forth in consecutive time steps. This could

be due to the reliance of the Adams-Bashforth method upon velocity information from two previous time steps versus the Runge-Kutta method's reliance on only one. Overall, better results were obtained using the Runge-Kutta method described here, and breakages in the simulations were reduced to such a degree that branching determinations were able to be made in more than 99% of simulations.

Another addition to the modeling approach is exact prescription of the location of multiple finite element nodes. In particular, FlexPDE allows inclusion of "features" which are user-defined curves along which FlexPDE makes the finite element triangle edges align. By defining the ESL boundary (where $w = 1$ µm) as a feature, FlexPDE meshes so that triangle edges and corresponding nodes along those edges fall along that boundary (see Figure 2.4). When RBCs are farther from the ESL boundary, this strategy improves both the speed and accuracy of the finite element solutions. When RBCs get close to or cross over these features, however, this can result in multiple very small triangles in the gaps between the RBC and ESL boundaries leading to poorly conditioned matrices and slow converging iterative methods. To alleviate this issue, portions of the boundary that are near the RBC are excluded from being prescribed as features. In those scenarios, multiple features are still used as they still help improve FlexPDE's mesh construction and corresponding numerical results but only portions of the ESL boundary that are farther than 0.1 µm away from the RBC are used.

Cutting the features up requires finding where the cell intersects the ESL boundary (akin to collision detection). A cell can actually cross the boundary in multiple locations, so in order to only include portions of the ESL boundary that are not within 0.1 µm of the cell, we must first find all points on the ESL boundary that are 0.1 µm away from the RBCs. This is done by first finding the points on the vessel wall that are closest to the RBC, as described previously. After finding those local minima, we search to the left and right of the left and rightmost minima, respectively, in order to find where the ESL boundary is exactly 0.1 µm away from the cell. ESL boundary points between those two locations (and effectively close to the cell) are omitted from the ESL boundary features created in FlexPDE.
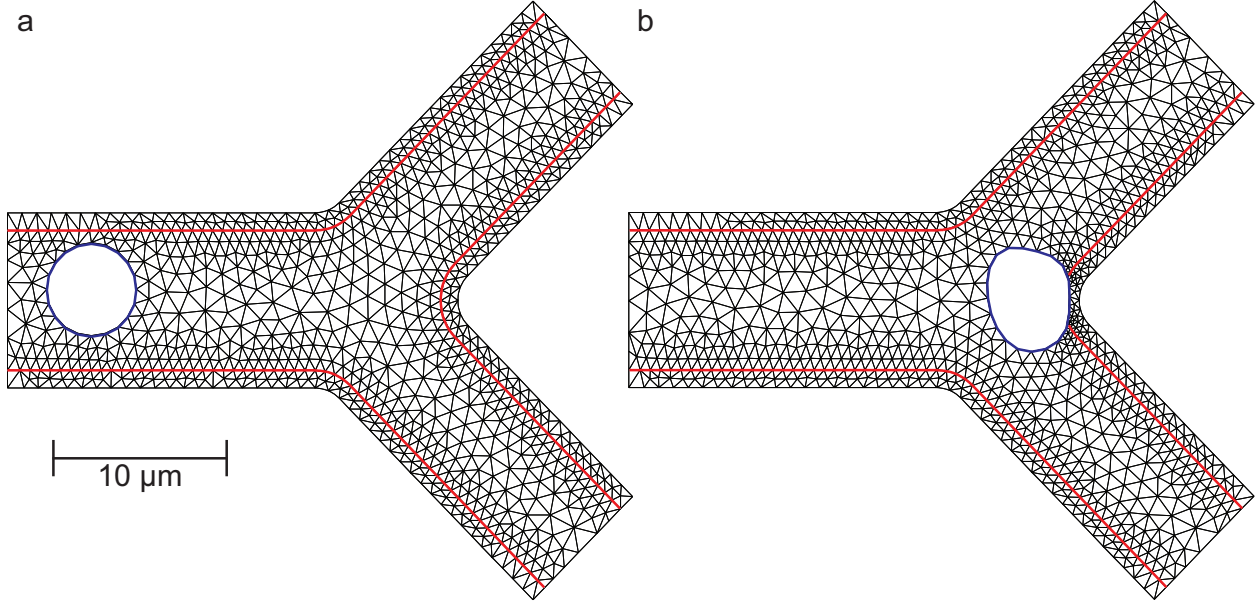
Figure 2.4. Mesh construction and ESL boundary feature, shown in red, for a typical simulation. **(a)** Mesh construction for a time step with no ESL penetration. Triangle edges and corresponding nodes fall along the ESL boundary feature. **(b)** Mesh construction with an RBC impinging upon the ESL. The feature at the far wall is broken into two sections no less than 0.1 µm from the cell.

2.3 Lubrication Forces

The external nodes and segments of the discretized RBCs often come into close proximity to each other and to the solid domain boundaries representing the vessel walls. The geometry of such situations are not realistic in a physiological sense due to the discretized nature of the cell. In reality, there are no sharp corners formed by linear segments in a cell membrane. Thus, when two surfaces come into close proximity with one another, the rate at which they approach each other may be overestimated if the narrow gap between them contains a corner. To account for the smooth edges of a real RBC, an external node that is in close proximity to another object is replaced by a linear segment of length $l = 0.1$ µm and set parallel to the other object, as shown in Figure 2.5. We will refer to this segment as the lubrication segment. Methods involving lubrication segments are employed to handle multiple close proximity scenarios that are described below.

While one could replace the node with such a segment by altering the cell's boundary in the finite element program, this is not the best option for obtaining accurate force calculations on these nodes. In fact, to accurately calculate the incompressibility of the fluid in a small (less than $w = 0.01$ µm wide) gap between a lubrication segment and an external segment, the penalty constant K, normally set at $K = 1 \times 10^8$ dyn·s/cm^4, must be increased to a value on the order of $K = 1 \times 10^{12}$ dyn·s/cm^4. This is even greater than the value predicted by a characteristic length scale of 0.01 µm, which indicates shortcomings in the finite element approach and corresponding pressure penalty method when using such extreme values. While one could replace the node with a segment and use this much higher value of K, the computational time required is approximately $\propto K$ making this an unfeasible solution. Instead, to better estimate the forces when cell nodes approach other objects, we also calculate and incorporate lubrication forces into the nodal equations.

In order to estimate appropriate lubrication forces that arise when an external node approaches another segment (whether that of another cell or a domain boundary segment), we solve the simplified steady Stokes equations in the narrow gap between the lubrication segment and the opposite segment. These equations may be simplified due to the assumption that the width of the gap, w, is much smaller than l, the length of the lubrication segment. This assumption is valid since these lubrication forces are only introduced in the model when $w \leq 0.01$ µm, and as mentioned above, l is taken to be 0.1 µm in typical situations. Thus, assuming without loss of generality that the lubrication segment is positioned in the $x - y$ plane vertically, as in Figure 2.5, we arrive at the following equation for fluid velocity in the gap:

$$\mu \frac{\partial^2 v(x,y)}{\partial x^2} = \frac{dp(y)}{dy}, \tag{2.26}$$

where $\boldsymbol{u} = (u(x,y), v(x,y))$. The goal is to calculate an equation for the total force acting upon the lubrication segment. To do so, we must first integrate the above equation with respect to x with the following boundary conditions for the velocities at the approaching node and the lubrication segment in place: $v(0,y) = v_n$, $v(w,y) = v_s$, $u(0,y) = u_n$, $u(w,y) = u_s$. In addition, we assume negligible p at the top and bottom (in particular, significantly smaller

38
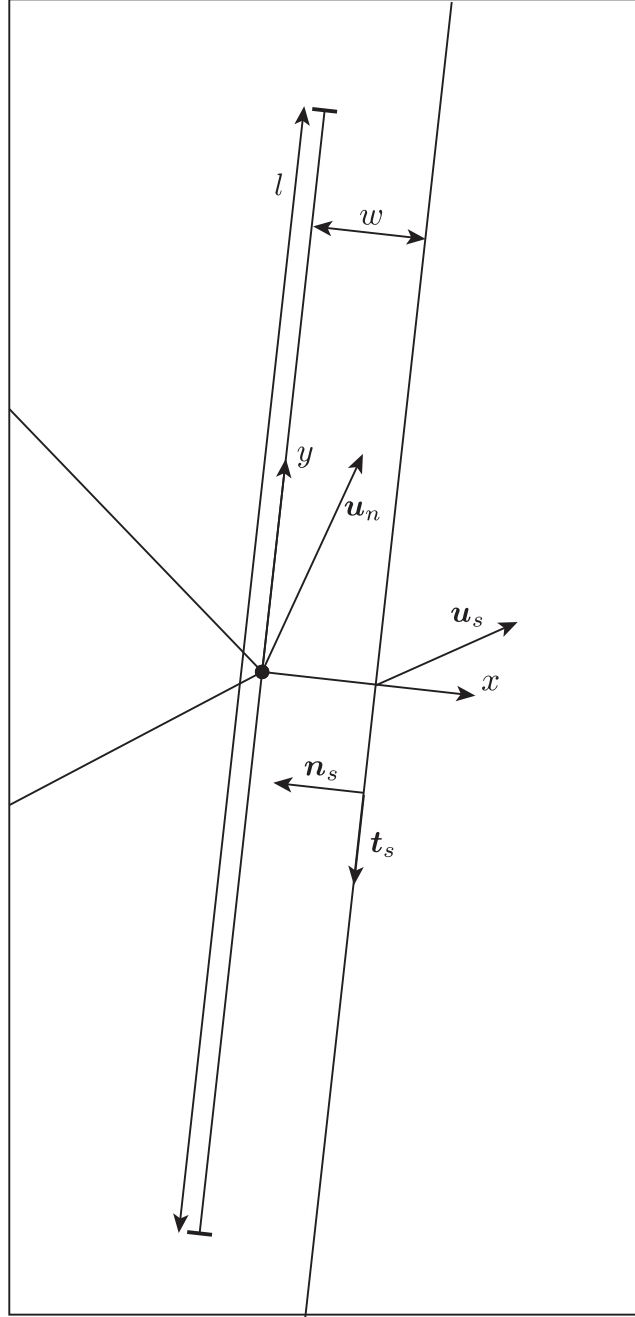
Figure 2.5. An external node of an RBC (left) approaching another segment of an RBC or vessel wall (right). Pictured is the temporary lubrication segment of length l parallel to the segment being approached. The width of the gap, always at least 10 times smaller than the length of the lubrication segment is denoted by w. Important vectors used in the equations calculating the lubrication forces arising from such a situation include $\boldsymbol{u}_n$ and $\boldsymbol{u}_s$, the velocity vectors of the external node and opposite segment, respectively, as well as $\boldsymbol{n}_s$ and $\boldsymbol{t}_s$, the vectors normal and tangential to the approached segment, respectively.

than the typically very high and low pressures generated within such gaps). Then, after applying the incompressibility condition, making rigid body assumptions, and integrating the force acting upon the lubrication segment as a result of its motion relative to the opposite segment, we have:

$$\boldsymbol{h} = -\mu \left(\left(\frac{l}{w} \right)^3 \hat{\boldsymbol{n}}_s \hat{\boldsymbol{n}}_s^T + \left(\frac{l}{w} \right) \hat{\boldsymbol{t}}_s \hat{\boldsymbol{t}}_s^T \right) \boldsymbol{u}_d, \tag{2.27}$$

where $\boldsymbol{h}$ is the force acting upon the lubrication segment. Here $\boldsymbol{u}_d = \boldsymbol{u}_n - \boldsymbol{u}_s$ where $\boldsymbol{u}_n$ is the velocity of the node/lubrication segment and $\boldsymbol{u}_s$ is the velocity of the opposite segment. Also, $\hat{\boldsymbol{n}}_s$ and $\hat{\boldsymbol{t}}_s$ are the unit normal and tangent vectors. Note that the unit vectors would be the same in relation to the lubrication segment as opposed to the opposite segment since these segments are constructed to be parallel to one another.

The motion of the cells are corrected using lubrication forces by introducing them to the nodal equations 2.19. Notice that the geometry used in the finite element solver is unaltered. As previously explained, altering the cell's boundary by including lubrication segments does not significantly improve results/performance. Instead, at the nodes, lubrication forces are introduced using a force of the form $\boldsymbol{f}_{i,lub} = r\boldsymbol{h}$:

$$t_i(0)\boldsymbol{t}_i - t_{i-1}(l_{i-1})\boldsymbol{t}_{i-1} - q_i(0)\boldsymbol{n}_i + q_{i-1}(l_{i-1})\boldsymbol{n}_{i-1} + T_i\boldsymbol{T}_i + r\boldsymbol{h} = 0. \tag{2.28}$$

$r = \max(0, 1 - w/0.01)$ is a linear ramping function added to gradually introduce the lubrication forces to the equations. Including such a function avoids abrupt changes in forces which may introduce instability to the system. In a case where the segment opposite the lubrication segment is part of another RBC, an equal and opposite force is applied. This force is distributed to the nodes connected to the opposite segment in proportion to their proximity to the location on the segment nearest the approaching external node. This is accomplished by incorporating the forces into the fluid forces acting upon this opposite segment, as follows:

$$g_{i,\text{lub}} = \boldsymbol{t}_i^T(\boldsymbol{\sigma}\boldsymbol{n}_i + \delta(s_0)r\boldsymbol{h}); \quad f_{i,\text{lub}} = \boldsymbol{n}_i^T(\boldsymbol{\sigma}\boldsymbol{n}_i + \delta(s_0)r\boldsymbol{h}) + p_{int} - p_{osm}, \tag{2.29}$$

where s_0 is the distance from the beginning of the opposite segment to the point on the opposite segment closest to the approaching node. Using these updated external forces, we

can update the nodal equations and incorporate the lubrication forces. For example, for $t_i(0.1)$ we get:

$$
\begin{aligned}
t_i(0.1) &= \bar{t}_i + \frac{1}{l_i} \int_0^{l_i} (l_i - s) g_{i,\mathrm{lub}}(s) ds \\
&= \bar{t}_i + \frac{1}{l_i} \int_0^{l_i} (l_i - s) g_i(s) ds + \mu r \left(\frac{l_i - 0.1}{l_i} \right) \left(\frac{l}{w} \right) \boldsymbol{t}_i^T \cdot \boldsymbol{u}_d.
\end{aligned}
\tag{2.30}
$$

When a single cell approaches (distance $< \delta_{lub} = 0.01$ µm) a vessel wall, or when two cells approach each other, or when a cell is deformed in such a way that its membrane approaches its opposite side (a squeezed cell), the scenario usually occurs as outlined above: a single node approaches a single segment. However, other scenarios arise with sufficient frequency during simulations to warrant special consideration.

A typical less straightforward scenario is illustrated in Figure 2.6, a case where a node is within δ_{lub} of not just one, but two segments of another RBC. Here We considered only cases where the two segments in question are adjacent to each other as cases where two non-adjacent segments both approach the same node were not seen in our simulations. Other scenarios, such as a node being in close proximity to three segments, do take place during simulations, but are exceedingly rare. In such rare cases, even though the simulation was stopped, we were still able to examine the results and assess the partitioning, deformation, and penetration behavior up to that point.

When a node (right node in Figure 3.4) is within δ_{lub} of two adjacent external segments, it falls into one of three categories when considering the angle between the two segments, α, associated with each node:

1. Equal but opposite normal vectors for the approaching node and the nearest node on the approached object. In this case, both α's are greater than 0 and the nearest point on the nearest segment to the approaching node is another node (2.6a).

2. Different normal vectors for the approaching node and the nearest node on the approached object. This can happen in two different ways. In one, both α's are greater than 0 but the nearest point on the nearest segment to the approaching node is *not* another node, as illustrated in 2.6b. In the other, both α's are less than 0 and will produce a similar set of
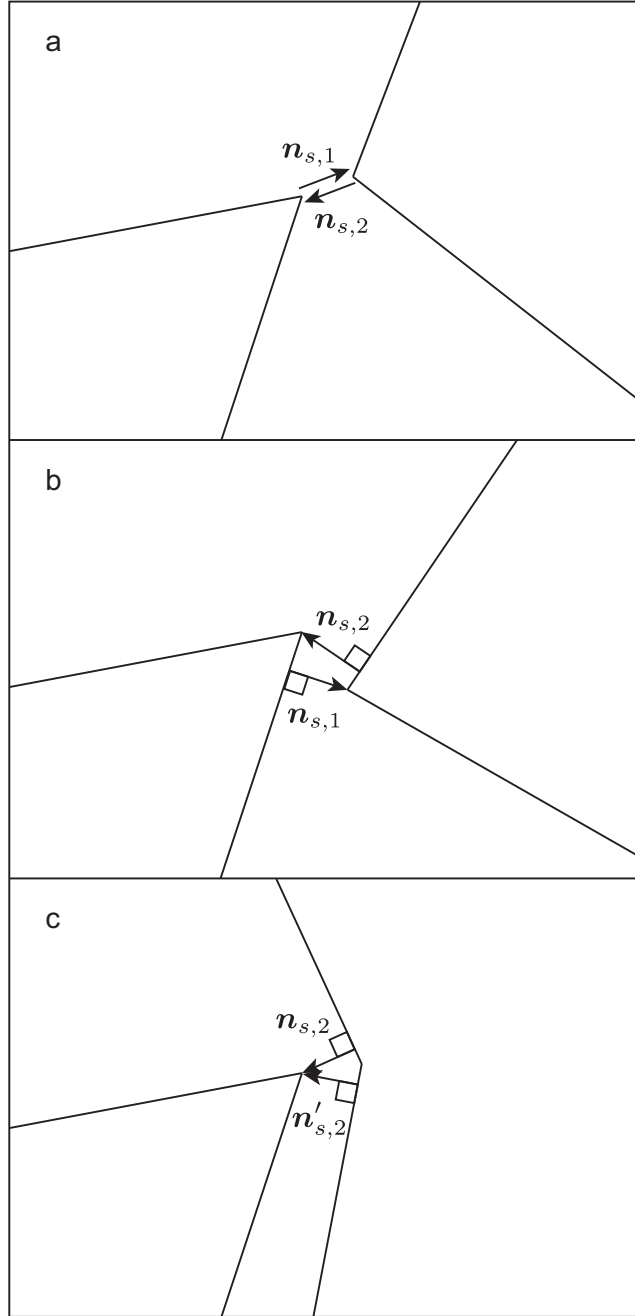
Figure 2.6. Applying lubrication forces in three special cases. The normal vectors associated with the node approaching on the right are labeled with a subscript 1 and point from the approached object to the approaching node. Similarly, the normal vectors associated with the node on the left are labeled with a subscript 2 and point from the approached object to the approaching node. The normal vectors $\boldsymbol{n}_s$ are those used to calculate lubrication force estimates in equation 2.27. **(a)** A node approaching two segments where the shortest distance between them is another node. **(b)** A node approaching two segments where the shortest distance between them is not another node. **(c)** A node approaching two segments where there are effectively two "shortest" distances.

two distinct normal vectors. (Note that when both α's are less than zero, the nearest point on the nearest segment to the approaching node cannot be another node, and so two distinct normal vectors will always occur in that situation.)

3. Two normal vectors for "closest points" on each segment. This occurs When one α is greater than 0 while the other is less, as illustrated in 2.6c.

Before discussing how these cases are handled, it is important to mention that these three cases are easily generalized to cases where a node is approaching a segment from the same cell through its interior. For example, if we instead think of Figure 2.6a as a cell being squeezed, α is less than 0 at the two encroaching nodes, instead of greater than 0. Despite this switch, the scenarios are treated exactly the same as those whose nodes and segments are from two different cells, except for a small adjustment to the viscosity of the cytoplasm. As mentioned above, the viscosity of the interior fluid of the cell is modeled through viscous interior segments. These segments stretch from the external nodes to a single interior node. This approximation of the effects of the interior viscosity is no longer accurate when those viscous interior segments lie approximately parallel to the sections of the cell membrane that approach each other. This is due to the viscous resistance acting only parallel to the membrane, not perpendicular to it, which is needed to accurately represent resistance to cell squeezing that is typically seen in cells. When a node of a cell approaches a segment from the same cell through its interior, this is exactly the situation that arises. This issue is alleviated by increasing the dynamic fluid viscosity of the plasma μ in the lubrication equation 2.27 to five times its original value. This matches experimental estimates of the value of the viscosity of cytoplasm [50].

In the three scenarios outlined above, one must take care to apply the lubrication forces carefully to the approaching nodes. This is done as follows:

1. The lubrication force of the approaching node is calculated by adjusting the normal vector $\boldsymbol{n}_s$ in equation 2.27 to be the vector connecting the approaching node to the node between the segments being approached, as seen in Figure 2.6a. Note that in such a scenario the node receives double the force, a direct contribution from the $r\boldsymbol{h}$ term (force due to it being near another object) and an indirect contribution from the delta function term in the

fluid equations (force due to it being the part of an object that is close to another node). Because of this only 0.5 of the calculated force is used for each node in question.

2. The lubrication force of the approaching node is calculated by taking $\boldsymbol{n}_s$ in equation 2.27 to be the normal vector pointing from the nearer of the two opposite segments to the approaching node, as seen in Figure 2.6b. This case has been previously handled by Barber [51] by adjusting l to take into account the proximity of the approaching node to the end of the opposite segment. However, this has lead to complications in regards to continuity with respect to the forces applied across multiple time steps as a node is dragged along multiple segments of another cell. Thus, the values are halved as before.

3. The lubrication force of the approaching node is calculated by taking $\boldsymbol{n}_s$ in equation 2.27 to be the normal vector pointing from the first opposite segment, as well as the second opposite segment and taking the average of the resulting forces. The node in between the opposite segments is omitted from lubrication force calculations to avoid a doubling of the resultant forces.

With multiple approximations made for these additional lubrication terms, it is important to note that the addition of these terms are not to accurately resolve forces and motion when nodes approach objects. Instead, the goal is to preserve the qualitatively correct behavior experienced by such nodes especially including elimination of unrealistic collisions of nodes with other objects. This additionally allows the dynamics of other nodes to continue evolving (compared to resulting in a crashed simulation) as the approaching nodes approach and retreat from objects in a qualitatively correct fashion. Finally, it should be mentioned that in the case of a node coming into close proximity to a curved portion of a vessel wall, it is observed that l is significantly smaller than the radius of curvature of the wall, and so the arc of the curvature of the wall may be reasonably ignored and the wall assumed to be straight for the purposes of calculating lubrication forces.

2.4 Parameter Values and Initial Conditions

Experimentally produced material parameter values of RBCs have been determined previously, specifically for the shear elastic modulus, shear viscosity, and the bending resistance

Table 2.1.
Parameters used in the model and their values.

Parameter	Description	Value	Units
k_p	Strength with which approximate area conservation is enforced	50	dyn/cm^2
k_t	Membrane shear elasticity	1.2×10^{-2}	dyn/cm
k_b	Membrane bending modulus	9×10^{-12}	dyn·cm
μ_{ext}	External segment viscosity	2×10^{-4}	dyn·s/cm
μ_{int}	Internal segment viscosity	1×10^{-4}	dyn·s/cm
μ	Dynamic viscosity of the surrounding fluid	1×10^{-2}	dyn·s/cm^2
l_0	Reference length of the external membrane segments	0.97	μm
A_{ref}	Reference area for the cross-sectional area of an RBC	22.2	μm^2
K	Penalty constant for enforcing incompressibility	1×10^8	dyn·s/cm^4
δ_{lub}	Threshold below which lubrication forces are calculated	1×10^{-2}	μm
κ	Maximum hydraulic resistivity in the ESL	Various	dyn·s/cm^4
$\Delta\boldsymbol{\pi}_p$	Maximum osmotic pressure difference between the ESL and the vessel lumen	Various	dyn/cm^2

of the membrane [52]. These values are not readily applicable to the two-dimensional discretization, however, and so parameters were selected such that RBC shapes and motions matched qualitatively with experimental results of continuous cell rotations observed in RBCs that are placed in dilute suspension in a high viscosity medium subjected to simple shear flow. [42]. These parameters were validated by comparing model predictions with corresponding experimental observations made both *in vitro* and *in vivo*. The resulting parameters are detailed in Table 2.1, and are used in every simulation described in subsequent chapters.

2.5 Reasons for Premature Simulation Termination

Due to the close interactions of RBCs with one another, with the vessel wall, or with the ESL region, it is occasionally necessary to terminate simulations before the criteria used to automatically determine a RBC's partitioning choice are met (section 3.2). Through the adaptive methods described above (2.2), physiologically unrealistic scenarios such as cell membrane segments intersecting one another are entirely avoided, which greatly reduces the number of failed simulations. In fact, in the vast majority of simulations (greater than 99%), the information required from the simulation, such as branching behavior, was successfully collected even in the situations where an automatic determination could not be made before simulation termination. However, the occasional simulations were, in fact, terminated before pertinent data could be collected.

Reasons for simulation failures generally fall under two categories. First, if the adaptive time step size is reduced to smaller than a rolling average of 1×10^{-7} ms over 10 time steps, the simulation cannot be expected to complete in a reasonable amount of computation time. And second, if a cell is in a situation requiring the calculation of lubrication forces that is not described above (2.3), the simulation is unable to proceed with accurate approximations of nodal velocities. An example situation would be if a cell node is within the lubrication threshold of more than two cell or vessel wall segments. In total, the number of such failing simulations was small enough as to have no significant effect on the results described in subsequent chapters.

2.6 Primary Mathematical and Numerical Challenges

The primary challenge of developing this model was to include an explicitly modeled ESL, resistant to both compression and flow, capable of interacting directly with flexible RBCs. In order to accurately represent RBC dynamics in a diverging microvessel bifurcation, this RBC-ESL interaction feature was vital. A sharp ESL boundary between the ESL region and the free flowing plasma was originally chosen. However, a relatively high rate of premature simulation termination for the sharp ESL boundary ultimately led to the implementation of a diffuse ESL boundary which produced similar, though more smooth, results.

To achieve greater numerical accuracy near the ESL boundary where the parameters associated with the ESL vary widely in a small amount of space, adjustments were made to the adaptive mesh generator. A "feature" boundary was created to ensure that the edges of the finite element triangles that form the mesh would align along the median of the ESL boundary. Greater mesh refinement was prescribed along the feature as well. However, as cells cross over this feature, very small triangles may arise in the resulting mesh. To prevent this, portions of the ESL boundary median are excluded from being defined as part of the feature. Making these exclusions requires determining exactly where the cell intersects with the ESL boundary median, which is akin to collision detection. Collision detection is also necessary when determining the ideal time step size in part to prevent RBC membranes from crossing over one another as they interact closely in the bifurcation. Close interactions between RBCs (and vessel walls in scenarios without an ESL) also necessitated the addition of lubrication elements. The proper application of these in myriad configurations of the positions of the segments and nodes that comprise the discretized cell membranes also presented a key mathematical challenge.

3. ISOLATED RED BLOOD CELL PARTITIONING, DEFORMATION, AND ESL PENETRATION IN DIVERGING CAPILLARY BIFURCATIONS

3.1 Introduction

The model developed in Chapter 2 is used here to consider red blood cells (RBCs) passing one at a time (isolated) through a microvessel bifurcation lined with an explicitly modeled endothelial surface layer (ESL). By removing the complexity of cell-cell interactions, the influence of the ESL on RBC dynamics may be studied more closely. In particular, the two ESL parameters of hydraulic resistivity and osmotic pressure difference are seen to have a significant impact on RBC dynamics in bifurcations. The effect of varying these parameters across physiological and pathological ranges is analyzed in relation to three primary aspects of RBC dynamics: RBC partitioning, RBC shape deformation, and the penetration of the RBC into the ESL region. In general, increasing hydraulic resistivity and/or osmotic pressure difference in the ESL increases uniform partitioning and deformation but decreases penetration. Possible mechanical explanations for these phenomena are explored, including the effect of these ESL properties on the centralization of fluid flow, cell migration effects, obstruction effects, and the time to recover from significant ESL penetration.

3.2 Methods

The initial shape of the RBCs for every simulation is taken to be a circle with radius $R_{cell} = 2.66$ µm. The three-dimensional equilibrium shape of an RBC is a biconcave disc. However, *in vivo*, the cross-section of the cell membrane, which our two-dimensional model is made to mimic, is constantly changing. Rather than choosing one of the many different cross-sectional shapes observed *in vivo* as the two-dimensional reference shape and potentially producing biased results, a circular shape is chosen. To encourage cells to quickly evolve into more realistic RBC cross-sections as simulations develop, the reference perimeter $nl_0 = 20 \times 0.97 = 19.4$ µm is set larger than the initial circular diameter $2\pi R_{cell} \approx 16.7$ µm. The center of the cell is initialized in the fluid at location $(x, y) = (-15 \text{ µm}, y_0)$. y_0 is contained

in the interval $[y_b, y_t] = [-(w_0/2 - w - R_{cell} - \epsilon), w_0/2 - w - R_{cell} - \epsilon] = [-1.29$ µm, 1.29 µm$]$ where w_0 is the width of the mother vessel, and w is the usual width of the ESL layer, as illustrated in Figure 2.2a. This corresponds to the initial cell shape being at least $\epsilon = 0.05$ µm away from the middle of the diffuse boundary of the ESL. For comparison's sake, the same interval is used in $\kappa = 0$ and $\kappa \to \infty$ scenarios.

The branching domain considered here is as seen in Figure 2.2a, and is representative of a diverging vessel bifurcation in a capillary network. The mother branch is taken to have a width of $w_0 = 10$ µm, or 8 µm not including the width of the ESL. It has been shown that arteriolar vessel diameters approximately follow the equation $w^3_{\text{mother}} = w^3_{\text{daughter}_1} + w^3_{\text{daughter}_2}$ [53]. Using this equation on the non-ESL portions of the vessels in our bifurcation along with the assumption that the two daughter branches have equal widths yields an estimate for the diameters of the non-ESL portion of the daughter branches of 6.35 µm or 8.35 µm when the ESL is included. Equal branching angles of 45° are considered. Past studies have suggested that the branching angle does not significantly affect cell partitioning [2], [15].

Changing ESL properties in a given microvascular system can affect flow at all levels from larger to smaller vessels with altered pressured drops and resistances in larger vessels affecting smaller vessel flows and vice versa. It is not immediately obvious, in general, how changing ESL properties may affect flow in capillaries. Hence, to better understand how to prescribe the total flow rate Q_0 in our system as ESL properties are varied, we calculated flow estimates by using a modified version of a portion of the compartmental model of Zhao et al. [11]. The model was modified to include an explicitly defined uniform porous layer in the vessels. The model includes compartments of identical large arterioles, small arterioles, capillaries, small venules, and large venules. The vessel lengths, diameters, dynamic fluid viscosities, and vessel counts were chosen in that model to match typical flow behavior in the rat hindlimb. To calculate the corresponding flow in such a system, one can use Ohm's Law applied to fluid flow which says that the flux of fluid through a vessel compartment is equal to the pressure drop across that compartment divided by the resistance to flow in that

compartment. Combining this with Kirchoff's Law applied to fluid flow, which says that fluid flux must be conserved across compartments, we get the following expression:

$$\frac{P_{distal} - P_1}{R_{LA}} = \frac{P_1 - P_2}{R_{SA}} = \frac{P_2 - P_3}{R_C} = \frac{P_3 - P_4}{R_{SV}} = \frac{P_4 - P_V}{R_{LV}} \tag{3.1}$$

where R_{LA}, R_{SA}, R_C, R_{SV}, and R_{LV} are the resistance to flow in each compartment and P_{distal}, $P_1, ...P_4$, and P_V are the pressures at either end of each corresponding compartment. The following pressure values were used by Arciero et al. [54]: $P_{distal} = 1.68 \times 10^5$ dyn/cm^2, which corresponds to 90% of the aortal pressure of 140 mmHg, and $P_V = 0$ dyn/cm^2. Resistance values are calculated for various values of κ, the hydraulic resistivity in the ESL, as described below, resulting in a system of linear equations that can be solved for the unknown pressures. These are then used to calculate average fluid flow rates in the capillaries:

$$\bar{u}_{cap} = \frac{P_2 - P_3}{R_C n_C A_{cap}} \tag{3.2}$$

where n_C is the number of capillaries in the compartment and $A_{cap} = \pi(w_0/2 - w)^2$ is the area of a circular cross section of the three-dimensional version of the standard capillary used in the simulations described in this chapter.

To calculate the resistance to flow in each compartment in equation 3.1, we begin with an equation for three-dimensional unidirectional flow in a cylinder of length L_{cyl} analogous to equation 2.6 used to model two-dimensional unidirectional flow:

$$\frac{\mu}{r} \frac{\partial}{\partial r} \left(r \frac{\partial u}{\partial r} \right) - \frac{\Delta p}{L_{cyl}} = \kappa_{cyl} u, \tag{3.3}$$

where $\kappa_{cyl} = \kappa$ in the porous layer and 0 elsewhere (a "sharp ESL boundary"). Solving for the fluid velocity, we obtain the solution (following techniques of Damiano et al. [55]):

$$u(r) = \begin{cases} \frac{\Delta p}{\kappa L_{cyl}} + c_1 \mathcal{J}_0 \left(i \frac{r}{\delta} \right) + c_2 \mathcal{Y}_0 \left(-i \frac{r}{\delta} \right) & \text{in the porous layer} \\ -\frac{\Delta p}{4 \kappa \delta^2 L_{cyl}} r^2 + c_3 \ln r + c_4 & \text{in the free flowing region} \end{cases} \tag{3.4}$$

50

where $\mathcal{J}_0$ and $\mathcal{Y}_0$ are Bessel functions of the first and second type, respectively, i denotes the imaginary unit, and $\delta = \sqrt{\mu/\kappa}$. Note that c_3 must equal zero to ensure a finite solution as $r \to 0$. The remaining unknown constants of integration c_1, c_2, and c_4 are determined by the following boundary conditions:

$$u_{por}(R_{cyl}) = 0;$$
$$u_{por}(R_{cyl} - w) = u_{free}(R_{cyl} - w); \tag{3.5}$$
$$\frac{du_{por}}{dr}(R_{cyl} - w) = \frac{du_{free}}{dr}(R_{cyl} - w),$$

where u_{por} and u_{free} denote $u(r)$ in the porous layer and in the free flowing region, respectively. The constants R_{cyl} and w denote the radius of the cylindrical vessel and the width of the porous layer (non-ESL region's radius is $R_{cyl} - w$). The first of these expressions corresponds to a no-slip boundary condition at the vessel wall, and the second and third to boundary conditions enforcing a continuous, differentiable transition of the flow profile from the porous layer to the free flowing region.

Before integrating $u(r)$ to calculate fluid flux, an adjustment was made to the values for the dynamic viscosity μ provided by Zhao et al. [11]. The values in that study used an empirically derived function for *in vivo* vessels from Pries et al. [43] that included the ESL implicitly. We, however, are explicitly including the ESL and so instead use an empirically derived function for the dynamic viscosity in glass tubes, also from [43]. Calculation of the average fluid flow rates in the capillaries produced differences of no more than 25% across the range of κ values used in this study.

The rescaling property of the Stokes flow equations says that if $\boldsymbol{u}$ and p solve the Stokes flow equations then so do $k\boldsymbol{u}$ and kp for any constant k, when boundary conditions are also appropriately rescaled. This leads to the predicted dynamics of the system, including partitioning behavior, deformation, and ESL penetration, remaining exactly the same only at a different time scale. This holds true for cells in vessels modeled as drops of higher viscosity liquid. However, this is not true in our case because the elements that comprise the RBCs contain not only viscous components but also elastic components. The elasticity voids the rescaling property. For example, an elastic element immersed in steady viscous flow

twice as strong will stretch much farther introducing zero fluid velocities (no-slip) along its additional length where the fluid velocities were not necessarily zero before. To investigate the rescalability properties of the model and how important the overall flow rate in the system is, a representative sample of simulations were run at both the fluxes listed above and fluxes increased by 50%. These produced no significant differences in resulting dynamics. This indicates that the 25% estimated spread among realistic average fluid flow rates in the capillaries can be safely ignored.

Q_0 was thus chosen to give average fluid velocities of approximately 0.1 cm/s, which is realistic physiologically [56]: $Q_0 = 8 \times 10^{-3}$ cm^2/s for cases including an ESL, and $Q_0 = 10 \times 10^{-3}$ cm^2/s when κ_v was set to zero, which corresponds to a vessel completely stripped of any ESL and effectively 10 µm wide. The fraction of bulk blood flow into the upper daughter branch, also referred to as the flow split of the upper daughter branch, is given by $\Psi_1 = Q_1/Q_0$, where Q_1 is the flux at the outlet of the upper daughter branch.

Five cases are considered in regards to the maximum hydraulic resistivity of the ESL, κ:

1. 0; ESL completely permeable, equivalent to an effective vessel width of 10 µm

2. 1×10^6 dyn·s/cm^4; low in comparison to normal physiological conditions, but observed experimentally due to certain pathological conditions [57]

3. 1×10^7 dyn·s/cm^4; lower bound of the normal physiological range [23]

4. 1×10^8 dyn·s/cm^4; upper bound of the normal physiological range [23]

5. ∞; impermeable ESL, equivalent to an effective vessel width of 8 µm

In the first and fifth cases, the osmotic pressure difference is set to $\Delta\pi_p = 0$ and ∞, respectively. These values correspond to the two extremes of a completely missing ESL $((\kappa,\Delta\pi_p) = (0,0))$ and a completely impermeable and rigid ESL $((\kappa,\Delta\pi_p)\rightarrow(\infty,\infty))$. For each of the second through fourth cases, two values are considered in regards to the maximum osmotic pressure difference, 20 and 200 dyn/cm^2, which correspond to estimates for the lower and upper bounds of the normal physiological range, respectively [58]. These values are equivalent to an osmotic pressure difference of $< 1\%$ when comparing the ESL to the free flowing plasma region.

To estimate cell partitioning behavior, we follow the precedent set by Barber [26]. An RBC is determined to have transitioned from the mother vessel to a specific daughter branch if all three of the following conditions hold:

1. It has crossed the middle of the diffuse ESL boundary or is within 0.1 µm of the vessel wall if no ESL is present.

2. All of the nodal velocities of the cell membrane point towards that daughter branch.

3. The y-value of the centroid of the cell lies on a background fluid streamline that enters that daughter branch.

The background fluid streamlines are the streamlines for the flow that occur when the cell is not present. If these criteria are not met due to a numerical failure causing the simulation to stop before a determination has been made, the simulation is examined by hand to determine which daughter branch the cell enters. There were no cases where a determination could not be made.

The RBC flux into the top or first daughter branch as a fraction of the total RBC flux into both daughter branches, Φ_1, can be estimated for a prescribed flow split, Ψ_1, as follows:

$$\Phi_1(\Psi_1) = \int_{y_b}^{y_t} p_1(y_0) b_1(\Psi_1, y_0) dy_0. \tag{3.6}$$

The density function $p_1(y_0)$ describes the probability that the center of a cell passes through $y = y_0$ when the center of the cell passes through $x = x_0 = -15$ µm, and is calculated as follows:

$$p_1(y_0) = \frac{u_d(y_0)}{\displaystyle\int_{y_b}^{y_t} u_d(y) dy}. \tag{3.7}$$

The distribution of the velocities upstream of the bifurcation, $u_d(y)$, is estimated by first measuring the instantaneous velocities of circular cells whose centers, $(x_0 = -15$ µm$, y_0)$, are placed at nine locations distributed uniformly on the interval $[y_b, y_t]$. The average nodal velocities of the external nodes are fitted with a fourth order polynomial which is used as an

estimate for $u_d(y)$. This polynomial fit has an R^2 value of > 0.98. The piecewise function $b_1(\Psi_1, y)$ is defined as follows:

$$b_1(\Psi_1, y_0) = \begin{cases} 1 & \text{if the RBC enters the upper branch} \\ 0 & \text{if the RBC enters the lower branch} \end{cases} \tag{3.8}$$

The initial y-value $y_0 = y_c$ over which the cell will enter the upper branch and below which the cell will enter the lower branch is found using a bisection algorithm that iterates until the interval bounding y_c is no larger than 0.041 µm. y_c is estimated by averaging the upper and lower bound on y_c obtained from the bisection algorithm.

Also considered is the effect of hydraulic resistivity and osmotic pressure difference on RBC deformations in diverging vessel bifurcations. For simulations involving a single RBC, this can be measured by calculating the dissimilarity in cell membrane shape for two simulated cells initialized at the same cell center coordinates $(x_0 = -15$ µm,$y_0)$. The shape disagreement in the cell membrane for two different simulated cells can be expressed using the equation:

$$SD(y_0, d_c) = 1 - \left(\frac{\text{overlapping cell area}}{\text{average cell area}} \right), \tag{3.9}$$

where shape disagreement, $SD(y_0, d_c)$, is a function of the common distance traveled by the centroids of both cell membranes. A similar equation was employed by Barber and Zhu [49] in regards to the deformation of cancer cells in a microfluidic channel.

Higher values of κ will produce more centralized flow profiles and faster traveling RBCs. To better isolate effects due to deformation versus translation, we compare the shapes of cells that have traveled the same distance instead of the same time. Because an adaptive time-stepper is used, the discrete times and distances at which cell shapes are calculated are not necessarily the same across different simulations. To find the shape of each compared cell after it has traveled d_c µm, linear interpolation with respect to the distance traveled by the centroid of the cell is used. The shape disagreement at d_c µm between cell shapes can then be calculated using the formula above. In addition, we can calculate an "average shape

disagreement" between different $(\kappa, \Delta \pi_p)$ sets by averaging with respect to the initial cell center y-value location, y_0, and distance traveled ($d_c = 0$ to 30 µm):

$$\overline{SD} = \frac{1}{30(y_t - y_b)} \int_{y_b}^{y_t} \int_0^{30} S_D(y_0, d_c) dd_c dy_0. \tag{3.10}$$

High sensitivity to the hydraulic resistivity or osmotic pressure difference in the ESL corresponds to a high percentage disagreement between cell membrane shapes, as this indicates a large differential effect on deformation of the cell.

Finally, how deeply an RBC penetrates into the ESL region is considered. This is measured at any given time, t, for a cell whose center is initialized at y-value y_0 by calculating the penetration of the RBC, δ, as follows:

$$\delta(t, y_0) = w - \min_{s_B, s_C} \| \boldsymbol{B}(s_B) - \boldsymbol{C}(s_C) \|_2, \tag{3.11}$$

where $\boldsymbol{B}(s_B)$ is a parametrization of the boundary curve corresponding to the vessel wall and $\boldsymbol{C}(s_C)$ is a parametrization of the cell membrane curve of the discretized RBC. This produces a positive value for RBCs penetrating past the middle of the diffuse boundary of the ESL and a negative value for RBCs before that midpoint. The methods used for obtaining the minimum distance to the vessel wall during the adaptive time integration process are also used to calculate the minimum distance and subsequent penetration (see section 2.2 for more details).

In order to better compare simulations across different $(\kappa, \Delta \pi_p)$ sets for a given flow split, "average passing time", $\bar{t}_p$, and "average maximum penetration distance", $\bar{\delta}_{max}$ are defined as follows. Passing time, t_p, is a function of the initial center center y-value, y_0, and is defined as the time it takes for cells to travel 30 µm, which is the approximate time RBCs take to fully navigate the bifurcation and travel down one of the daughter branches (see Figure 3.3). Average passing time is given by:

$$\bar{t}_p = \frac{1}{y_t - y_b} \int_{y_b}^{y_t} t_p(y_0) dy_0. \tag{3.12}$$

The maximum penetration distance, δ_{max}, for a given initial cell center y-value, y_0, is found by taking the maximum of the penetration distance, δ, over the entire simulation time: $\delta_{max}(y_0) = \max\limits_{t}(\delta(t, y_0))$. The average maximum penetration distance is then found by averaging the maximum penetration distance for all cells that significantly penetrate the ESL over y_0. This corresponds to cells that penetrate past the middle of the diffuse boundary of the ESL region, or $\delta > 0$. Therefore, we have the following definition.

$$\bar{\delta}_{max} = \frac{\int_{y_b}^{y_t} \delta_{max}(y_0) H(\delta_{max}(y_0)) dy_0}{\int_{y_b}^{y_t} H(\delta_{max}(y_0)) dy_0}, \tag{3.13}$$

where H is a Heaviside function that is 0 when $\delta_{max} < 0$ and 1 otherwise.

3.3   Results

In Figure 3.1a, the critical initial y-value of the RBC center, y_c, is plotted as a function of the fraction of bulk blood flow entering the upper daughter branch, Ψ_1. y_c is the value over which the cell would enter the upper branch, and below which the cell would enter the lower branch. Using equation 3.6 gives Figure 3.1b which shows the fraction of cells entering the upper branch, Φ_1, plotted as a function of Ψ_1. Results are plotted for a low hydraulic resistivity of $\kappa = 10^6$ and a high hydraulic resistivity of 10^8 dyn·s/cm^4 in solid red and blue, respectively, for a high osmotic pressure difference of $\Delta\pi_p = 200$ dyn/cm^2. The dashed red curves correspond to scenarios with a low hydraulic resistivity of $\kappa = 10^6$ dyn·s/cm^4 for a low osmotic pressure difference of $\Delta\pi_p = 20$ dyn/cm^2. The case of high hydraulic resistivity and low osmotic pressure difference in the ESL is not shown, as it coincides with the solid blue line already plotted. This indicates that the osmotic pressure difference does not significantly affect partitioning at high levels of hydraulic resistivity. The other cases plotted, however, show subtle trends.

Note that uniform partitioning of cells corresponds to the diagonal line $\Phi_1 = \Psi_1$, which corresponds to the fraction of cells entering the upper branch equaling the fraction of bulk blood flow entering that branch. This indicates that the farther a curve is from this diagonal line, the more nonuniform the partitioning becomes. It can be seen then that lowering the

hydraulic resistivity in the ESL results in more nonuniform partitioning, and that lowering the osmotic pressure difference increases this nonuniformity even further. However, these trends are small when compared to other factors that may affect partitioning behavior such as RBC flexibility or vessel size [2], [15].

An example of cells that are partitioned differently due solely to ESL property differences is observed in Figure 3.2. Plotted in blue is a cell from a simulation using a high hydraulic resistivity of $\kappa = 10^8$ dyn·s/cm^4, and plotted in red is a cell from a simulation using a low hydraulic resistivity of $\kappa = 10^6$ dyn·s/cm^4. A high osmotic pressure difference of $\Delta\pi_p = 200$ dyn/cm^2 is used in both cases. Both cells are initialized at the same center point, $(x_0, y_0) = (-15, 1.048)$, at a flow split of $\Psi_1 = 0.3125$. In Figure 3.2a, snapshots of the cells are shown after 0, 10, 20, and 30 µm distance traveled. Also included are cell streamlines for each cell which are comprised of the paths that the centroid of each cell follows. Initially, the cell in the case of high hydraulic resistivity in the ESL deforms more than the other cell which leads to more migration towards the mother vessel centerline. The streamline of this cell remains below that of the low hydraulic resistivity case until both cells have traveled approximately 17.9 µm. From this point on, however, the streamlines cross over each other and the cell in the high hydraulic resistivity case enters the upper branch while the other cell enters the lower branch.

To understand the mechanisms at work behind the streamlines of these cells crossing over one another, in Figure 3.2b and c is shown in closer detail the velocities of the fluid and nodes of the cells. A snapshot of the cells is shown after 18.5 µm were traveled. Velocity profiles of the bulk blood flow in each of the two hydraulic resistivity cases are shown in the mother and daughter vessels. For high hydraulic resistivity, little flow is possible through the ESL, and so to conserve flux, higher velocities occur near the vessel centerlines than occur in the low hydraulic resistivity case. This leads to higher shear rates which gives rise to greater RBC deformations, as previously observed. This also leads to a greater obstruction effect, which is described by Barber et al. [15] as the effect of a cell blocking a daughter branch being more likely to enter that branch. By entering the branch, the cell makes up for a decreased plasma flow directly into the branch and preserves the downstream flow split and the conservation of volume flux. Increasing hydraulic resistivity in the ESL reduces flow
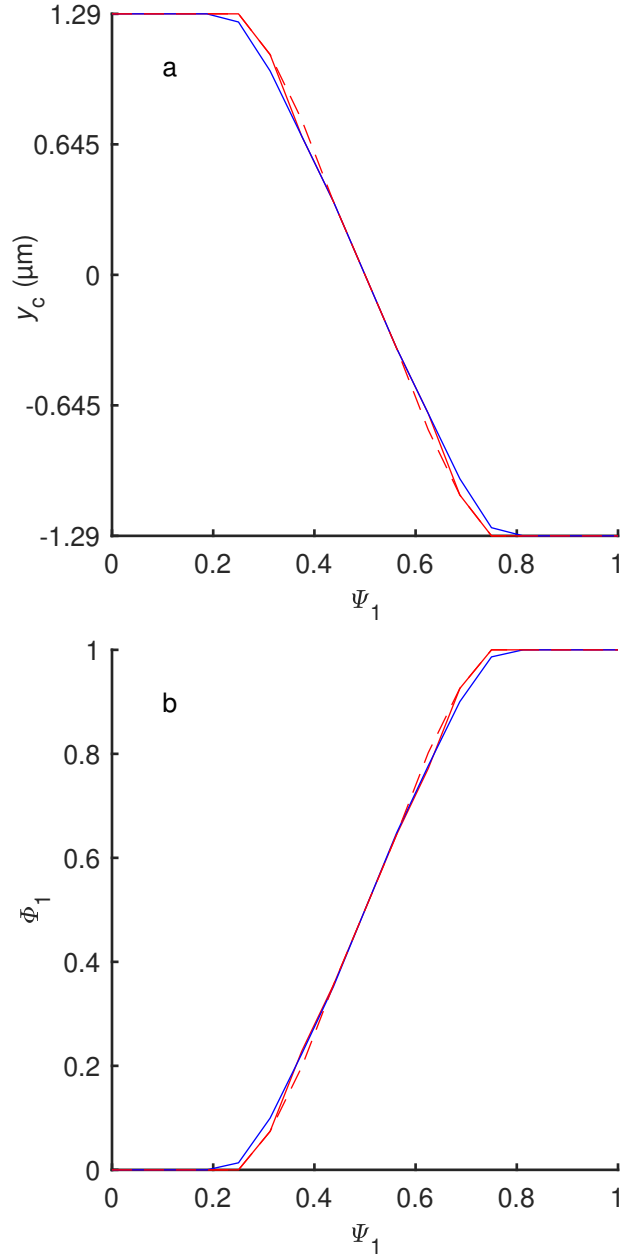
Figure 3.1. The effects of ESL properties on RBC partitioning at a microvessel bifurcation. Results are plotted for $\kappa = 10^6$ and 10^8 dyn·s/cm^4 in solid red and blue curves, respectively, for $\Delta\pi_p = 200$ dyn/cm^2. The dashed red curves correspond to $\kappa = 10^6$ dyn·s/cm^4 for $\Delta\pi_p = 20$ dyn/cm^2. **(a)** The critical initial y-value of the cell center, y_c, and **(b)**, the fraction of RBCs entering the upper branch, Φ_1, as a function of bulk blood entering the upper branch, Ψ_1.

through the ESL which effectively narrows the gaps between the obstructing cell and the walls at the opening of the vessel. This leads to an overall increase in the strength of the obstruction effect as less plasma flow is able to enter the obstructed branch, as seen in the velocities plotted at the opening of the upper daughter branch.

It should be noted that the two primary effects of an increased hydraulic resistivity for isolated cell partitioning described above have opposing effects. Higher hydraulic resistivity in the ESL increases migration towards the mother vessel centerline which increases the number of cells entering the high flow branch. This leads to more nonuniform partitioning. However, higher hydraulic resistivity in the ESL also increases the strength of the obstruction effect experienced by cells traveling through the bifurcation which increases the number of cells entering the low flow branch. This leads to less uniform partitioning. Overall, the obstruction effect is the stronger of the two and so increasing hydraulic resistivity in the ESL leads to more uniform partitioning, as seen in Figure 3.1.

When decreasing osmotic pressure difference at a low level of hydraulic resistivity in the ESL, cells in the mother vessel remain relatively unaffected by the forces due to the osmotic pressure difference. Hence decreasing the osmotic pressure difference has a negligible effect on cell migration. However, at the bifurcation, the cell is able to significantly penetrate into the ESL region which reduces the level of obstruction they cause at the daughter branches. ESL penetration is plotted in Figure 3.6. As described above, reduced obstruction leads to more nonuniform partitioning.

Figure 3.3 compares simulations with two different levels of hydraulic resistivity, $\kappa = 10^8$ and 10^6 dyn·s/cm^4, plotted in blue and red, respectively. The osmotic pressure difference for both is set at $\Delta\pi_p = 200$ dyn/cm^2, and the flow split for both is $\Psi_1 = 0.375$. Cell center y-values are initialized at $y_0 = 0.726$ µm above the mother vessel centerline in Figures 3.3a and c and at $y_0 = 0.645$ µm in Figures 3.3b and d. Given the level of refinement in simulations predicting the critical initial cell center y-value at the flow split of $\Psi_1 = 0.375$, these are the initial y-values closest, above and below, to the predicted value of $y_c = 0.685$, which for both levels of hydraulic resistivity is the same. However, due to the discrete nature of the bisection algorithm used to make the prediction, these values are likely not precisely equidistant from the critical value. Rather, they were chosen such that they are as close to
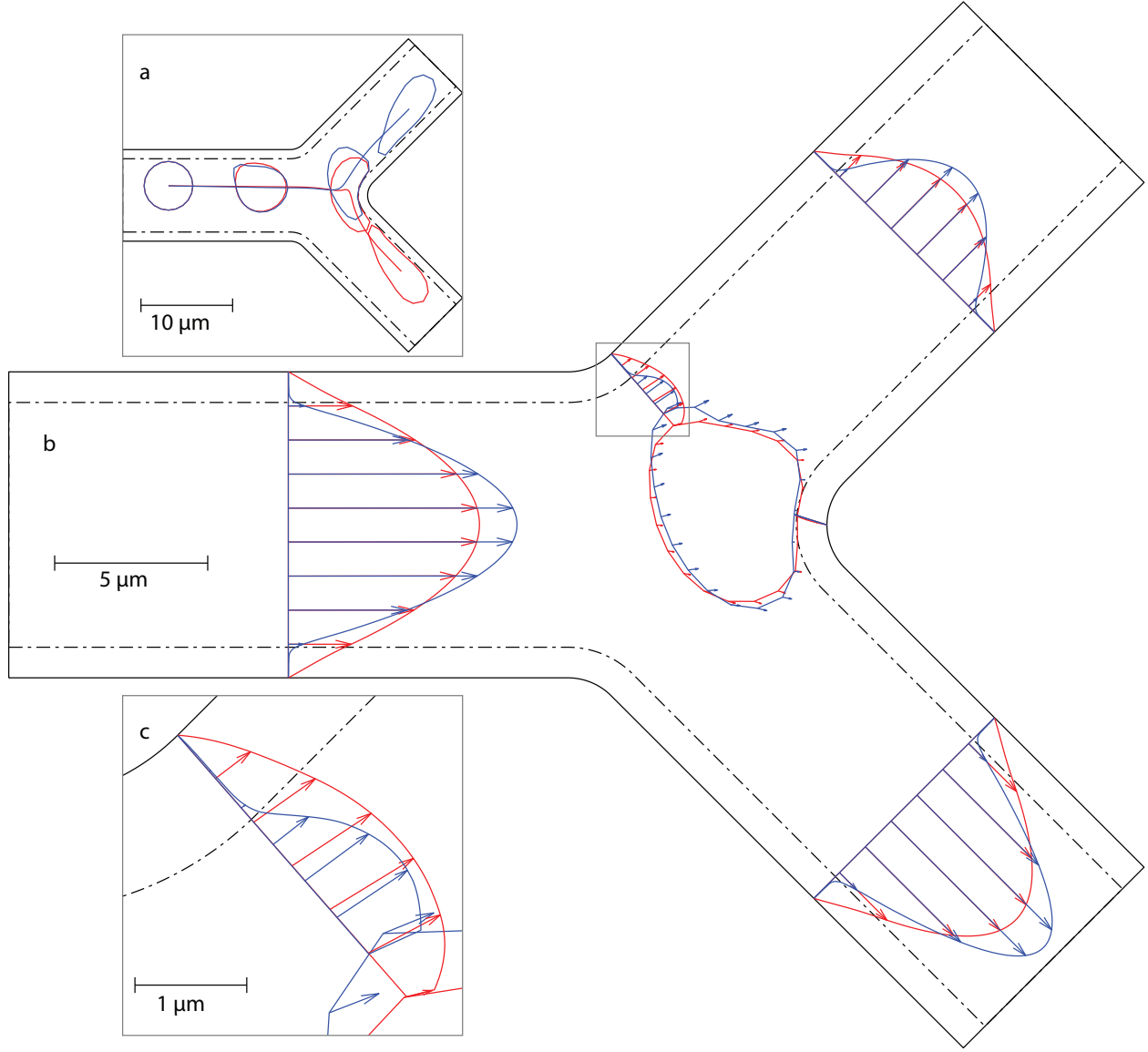
Figure 3.2. An example of distinct partitioning behavior between scenarios with differing levels of hydraulic resistivity in the ESL for Ψ_1=0.3125. Blue represents $\kappa = 10^8$ dyn·s/cm^4 and red represents $\kappa = 10^6$ dyn·s/cm^4, both for $\Delta\pi_p = 200$ dyn/cm^2. **(a)** Snapshots of RBCs at 0, 10, 20, and 30 µm traveled plotted with the cell streamlines. **(b)** Velocity profiles of the bulk blood flow, as well as nodal velocities of the RBCs at a 18.5 µm snapshot. The region enclosed in the grey box is magnified in **(c)**. **(c)** The velocity profiles of the bulk blood flow at the mouth of the low flow daughter branch from the cell membrane to the vessel wall, including the ESL.

equidistant as possible in this study. At $y_0 = 0.726$ μm, both cells enter the upper branch, and at $y_0 = 0.645$ μm, both cells enter the lower daughter branch. The trajectories of the centroid of each cell is also plotted. In general, cells in the higher hydraulic resistivity cases appear to undergo more deformation and elongation while navigating the bifurcation.

In Figure 3.3c, shape disagreement between the cells in the high and low hydraulic resistivity cases from Figures 3.3a and b is plotted as a function of the distance traveled by the cells for both $y_0 = 0.726$ and 0.645 μm in solid and dashed curves, respectively. The cells entering the lower branch see a larger shape disagreement as they pass through the bifurcation than those entering the upper branch. However, before the cells interact with the ESL at the bifurcation, the opposite is true. Figure 3.3d shows the distance the cell travels through the bifurcation as a function of the time the cell has traveled for each simulation. As before, high and low hydraulic resistivity is plotted in blue and red, respectively, and solid and dashed curves correspond to the initialized cell center y-values of $y_0 = 0.726$ μm and $y_0 = 0.645$ μm, respectively. In general, higher hydraulic resistivity in the ESL leads to a cell traveling faster.

Both increased deformation and increased speed for higher hydraulic resistivity in the ESL can be explained by increased flow centralization, as was seen in Figure 3.2. For higher hydraulic resistivity in the ESL, fluid is effectively forced to flow through more narrow gaps between cells and vessel walls. This leads to higher fluid flow rates as cells pass through the vessels, as well as higher forces allowing the fluid to stretch and compress the cell more vigorously than in scenarios with lower hydraulic resistivity in the ESL.

Figure 3.4a shows how cell shape disagreement between cells depends on the initial cell center location. Cell shape disagreement between high and low hydraulic resistivities of $\kappa = 10^8$ dyn·s/cm^4 and $\kappa = 10^6$ dyn·s/cm^4, respectively, is plotted as a function of the entire range of possible initial cell center y-values, $[y_b, y_t] = [-1.29, 1.29]$. For both, the osmotic pressure difference is $\Delta\pi_p = 200$ dyn/cm^2 and the flow split is $\Psi_1 = 0.375$. Upon traveling 10 μm, plotted in red in Figure 3.4b, before reaching the bifurcation, higher shape disagreement is observed in cells initialized nearer the walls of the mother vessel, where the shear rate is generally higher. At 20 μm, after interaction with the ESL at the bifurcation, an additional spike of shape disagreement just below the predicted critical value y_c develops.
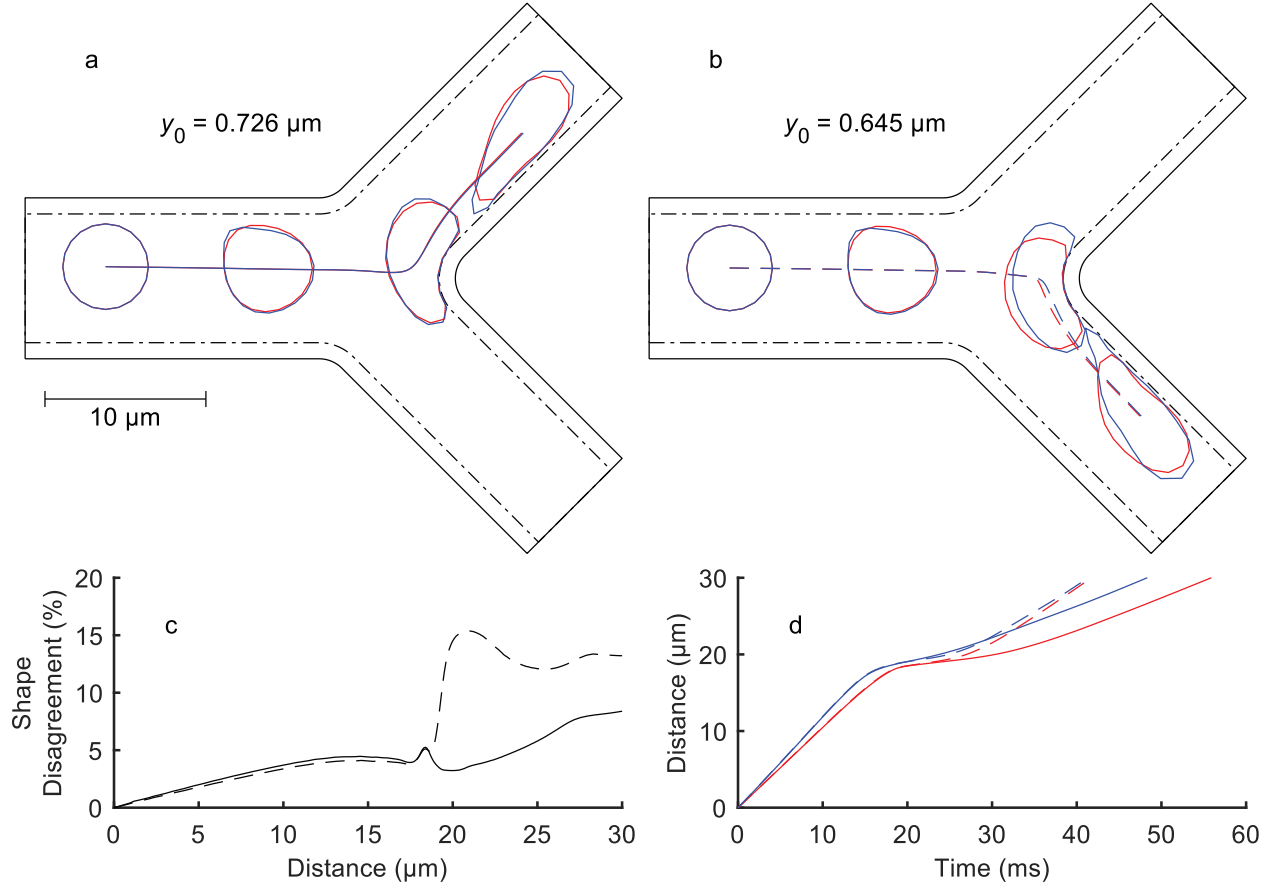
Figure 3.3. The effects of hydraulic resistivity in the ESL on cell shape and speed for $\Psi_1 = 0.375$. Blue represents $\kappa = 10^8$ dyn·s/cm^4 and red represents $\kappa = 10^6$ dyn·s/cm^4, both for $\Delta\pi_p = 200$ dyn/cm^2. Snapshots of RBCs at 0, 10, 20, and 30 µm traveled are plotted with the cell streamlines, initialized at **(a)** $y_0 = 0.726$ µm and **(b)** $y_0 = 0.645$ µm. Solid curves represent simulations entering the upper branch, dashed curves represent simulations entering the lower branch. **(c)** Shape disagreement percentages between cells in **(a)** and **(b)** are plotted with solid and dashed curves, respectively. **(d)** Distance traveled by each cell as a function of the time spent traversing the bifurcation.

$y_0 = y_c$ is included in the figure as a dashed black line. A similar spike is not seen just above the predicted critical value as cells tend to act more alike when both enter the low flow branch. For an example of this, see Figure 3.3a where the cells entering the low flow branch look much more similar than those entering the high flow branch in Figure 3.3b. At 30 µm, after cells have entered their respective daughter branches, the shape disagreements increase further with the exception of the spike just below y_c which decreases slightly. Note

that y_c is only predicted to be the same for both the high and low hydraulic resistivity cases for high osmotic pressure differences due to the refinement of the bisection algorithm used. In actuality, the critical values for these scenarios are most likely slightly different, with the critical value in the low hydraulic resistivity case probably the higher of the two, in agreement with dynamics for low osmotic pressure differences. Figure 3.4b shows the actual cell center locations for the cell after they have traveled 0, 10, 20, and 30 µm. In this panel, a slight constriction of cell center trajectories due to cell migration may be observed before the distribution of cells widen farther downstream.

For the flow split $\Psi_1 = 0.375$, Tables 3.1 and 3.2 give the average shape disagreement percentages for a range of hydraulic resistances at low and high osmotic pressure differences, respectively. For example, the cells in Figure 3.4 are comparing $(\kappa, \Delta\pi_p) = (10^8$ dyn·s/cm^4,200 dyn/cm^2) to $(10^6$ dyn·s/cm^4,200 dyn/cm^2). The corresponding average shape disagreement percentage, found in Table 3.2, is 9.06%. In general, comparing more disparate levels of hydraulic resistivity leads to a higher shape disagreement percentage, regardless of osmotic pressure difference. Also, lower osmotic pressure differences lead to higher shape disagreement percentages. The special cases involving a vessel without an ESL, where $\kappa = 0$ and $\Delta\pi_p = 0$, and a vessel with an impenetrable ESL, where $\kappa \to \infty$ and $\Delta\pi_p \to \infty$, were included to be able to compare to those extreme physiological cases.

Figure 3.5 compares simulations with two different levels of osmotic pressure difference, $\Delta\pi_p = 200$ dyn/cm^2 and $\Delta\pi_p = 20$ dyn/cm^2, plotted in blue and red, respectively. The flow split for both is $\Psi_1 = 0.375$. As seen in Figures 3.3 and 3.4, comparisons of cells initialized near and below the mother vessel centerline lead to greater shape disagreement percentages than those near and above the centerline. To focus on the greater disagreement percentages, the cell center y-values for both were initialized at $y_0 = 0.645$ µm above the centerline and were chosen so that they are close to and below the predicted critical values of $y_c = 0.685$ and 0.766 µm for $\Delta\pi_p = 200$ dyn/cm^2 and $\Delta\pi_p = 20$ dyn/cm^2, respectively. The trajectories of the centroid of each cell are also plotted. These are represented by solid curves when corresponding to a low hydraulic resistivity of $\kappa = 10^6$ dyn·s/cm^4, as in Figure 3.5a, and dashed curves when corresponding to a high hydraulic resistivity of $\kappa = 10^8$ dyn·s/cm^4, as in Figure 3.5b.
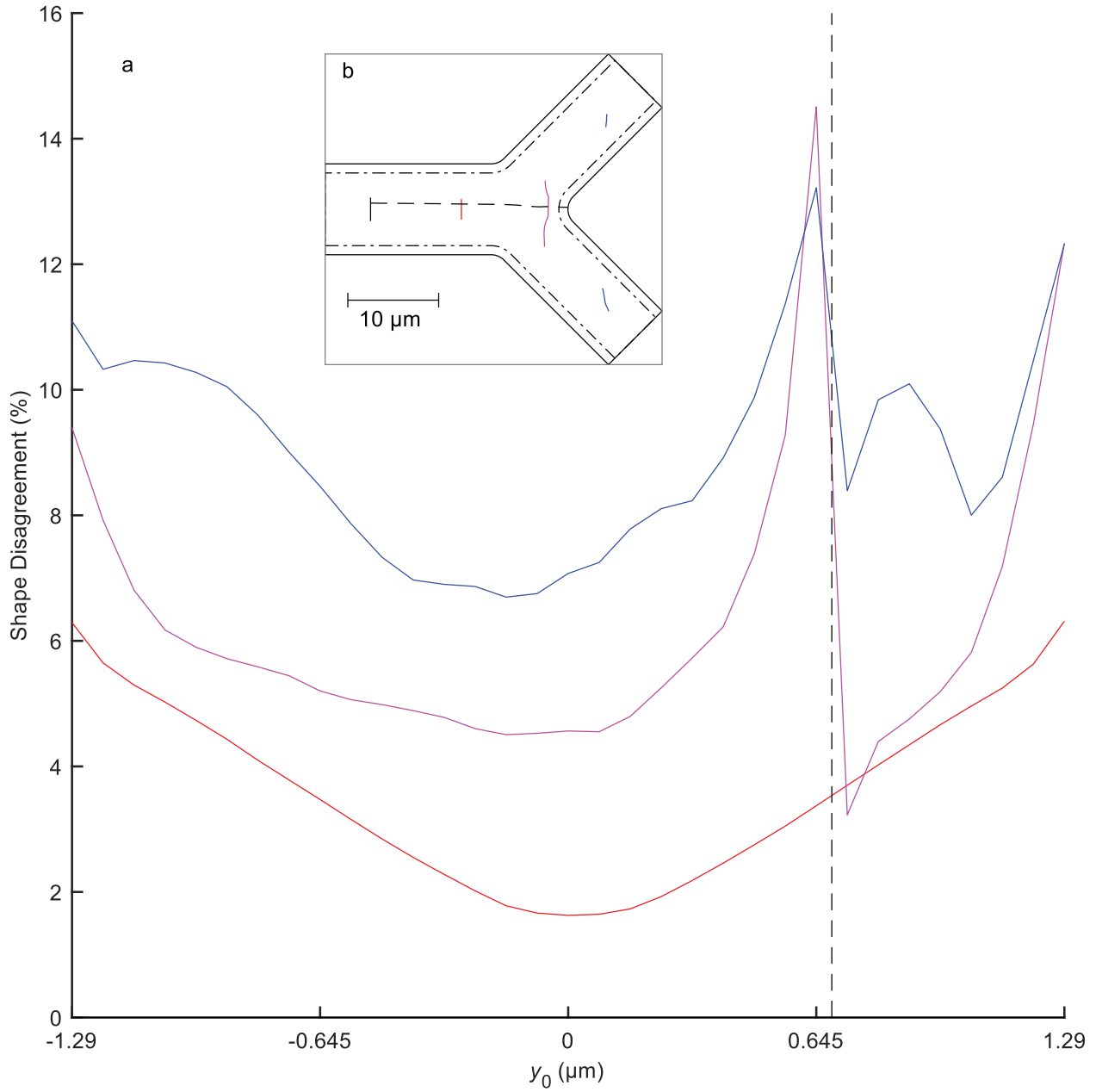
Figure 3.4. Dependence of cell shape disagreement between simulations run at $\kappa = 10^6$ and 10^8 dyn·s/cm^4 on initial cell center location for $\Psi_1 = 0.375$ and $\Delta\pi_p = 200$ dyn/cm^2. Cells are compared after 0, 10, 20, and 30 µm, and are plotted as black, red, magenta, and blue curves, respectively. **(a)** Cell shape disagreement percentage as a function of initial cell center y-values, y_0. The black dashed line is located at $y_0 = y_c = 0.685$ µm. **(b)** The cell center locations after traveling 0, 10, 20, and 30 µm. The black dashed curve is the predicted separating cell streamline that begins at y_c.

Table 3.1.

Average shape disagreement percentages when comparing simulations with different hydraulic resistivities in the ESL at a low osmotic pressure difference of $\Delta\pi_p = 20$ dyn/cm^2 (unless otherwise noted) and a flow split of $\Psi_1 = 0.375$.

κ (dyn·s/cm^4)	$0, \Delta\pi_p = 0$	10^6	10^7	10^8
$\infty, \Delta\pi_p \to \infty$	20.35	14.20	10.02	4.11
10^8	17.72	11.52	6.70	
10^7	13.21	5.88		
10^6	8.77			

Table 3.2.

Average shape disagreement percentage when comparing simulations with different hydraulic resistivities in the ESL at a high osmotic pressure difference of $\Delta\pi_p = 200$ dyn/cm^2 (unless otherwise noted) and a flow split of $\Psi_1 = 0.375$.

κ (dyn·s/cm^4)	$0, \Delta\pi_p = 0$	10^6	10^7	10^8
$\infty, \Delta\pi_p \to \infty$	20.35	10.31	7.43	3.23
10^8	18.06	9.06	5.62	
10^7	15.37	4.29		
10^6	14.17			

Upstream of the bifurcation, there is very little difference in shape for both comparisons. This is due to cells remaining far from the ESL region where forces due to osmotic pressure difference are small. Also, as each comparison is made at a single level of hydraulic resistivity, the fluid flow field is exactly equal when cell shapes are equal as osmotic pressure difference does not affect it. At the bifurcation in Figure 3.5a, the cell in the simulation with lower osmotic pressure difference penetrates into the ESL region significantly more than the other cell. This leads to a significant shape disagreement between the two, as well as a more rounded shape. Similar dynamics may be observed for high hydraulic resistivity in Figure 3.5b, diminished as they are when compared to the case of low hydraulic resistivity.

In Figure 3.5c, shape disagreement percentage between cells in simulations with the two different osmotic pressure differences for both the low and high hydraulic resistivity cases are plotted as functions of distance traveled in solid and dashed curves, respectively. At its peak, upon reaching the ESL at the bifurcation, more cell shape disagreement is seen for low hydraulic resistivity compared to that of the high hydraulic resistivity case. Prior to interaction with the ESL, there is practically no shape disagreement. After traveling into a daughter branch, shape disagreement begins to decrease in both cases. Figure 3.5d plots the distance traveled by each of the cells as a function of time. Higher hydraulic resistivity in the ESL leads to cells traveling faster than those in low hydraulic resistivity simulations. Also, higher osmotic pressure difference in the ESL leads to cells traveling slower upon initial interaction with the ESL than those in low osmotic pressure difference simulations that readily and more quickly sink into the layer. However, due to more shallow penetration into the layer, the higher osmotic pressure difference cells travel more quickly than their cohorts thereafter. This can be seen most clearly in the low hydraulic resistivity simulations though the same trend does occur for higher hydraulic resistivity as well in a diminished capacity.

Plotted against the entire range of possible initial cell center y-value locations y_0 for a flow split of $\Psi_1 = 0.375$, Figure 3.6a shows the maximum distance a cell penetrates into the ESL for low, medium, and high hydraulic resistivities of $\kappa = 10^6$, 10^7, and 10^8 dyn·s/cm^4 as red, green, and blue curves, respectively. For each of these, both low and high osmotic pressure difference cases of $\Delta\pi_p = 20$ and 200 dyn/cm^2 are shown as dashed and solid curves, respectively. Cells penetrate farther into the ESL if initialized closer to the separating cell streamline that begins at $y_0 = y_c$. However, >50% of cells in low osmotic pressure difference simulations, regardless of hydraulic resistivity level, penetrated beyond the midpoint of the diffuse boundary of the ESL region which indicates that close proximity to the separating cell streamline is not required for significant penetration. In general, lower hydraulic resistivity and lower osmotic pressure difference in the ESL result in higher penetration distances of cells into the ESL. Osmotic pressure difference appears to impact penetration distances more than hydraulic resistivity. Lowering hydraulic resistivity from physiological to pathological values increased maximum penetration distance two-fold, while lowering osmotic pressure difference increased the same fifteen-fold. A maximum penetration distance of 3.7% of the
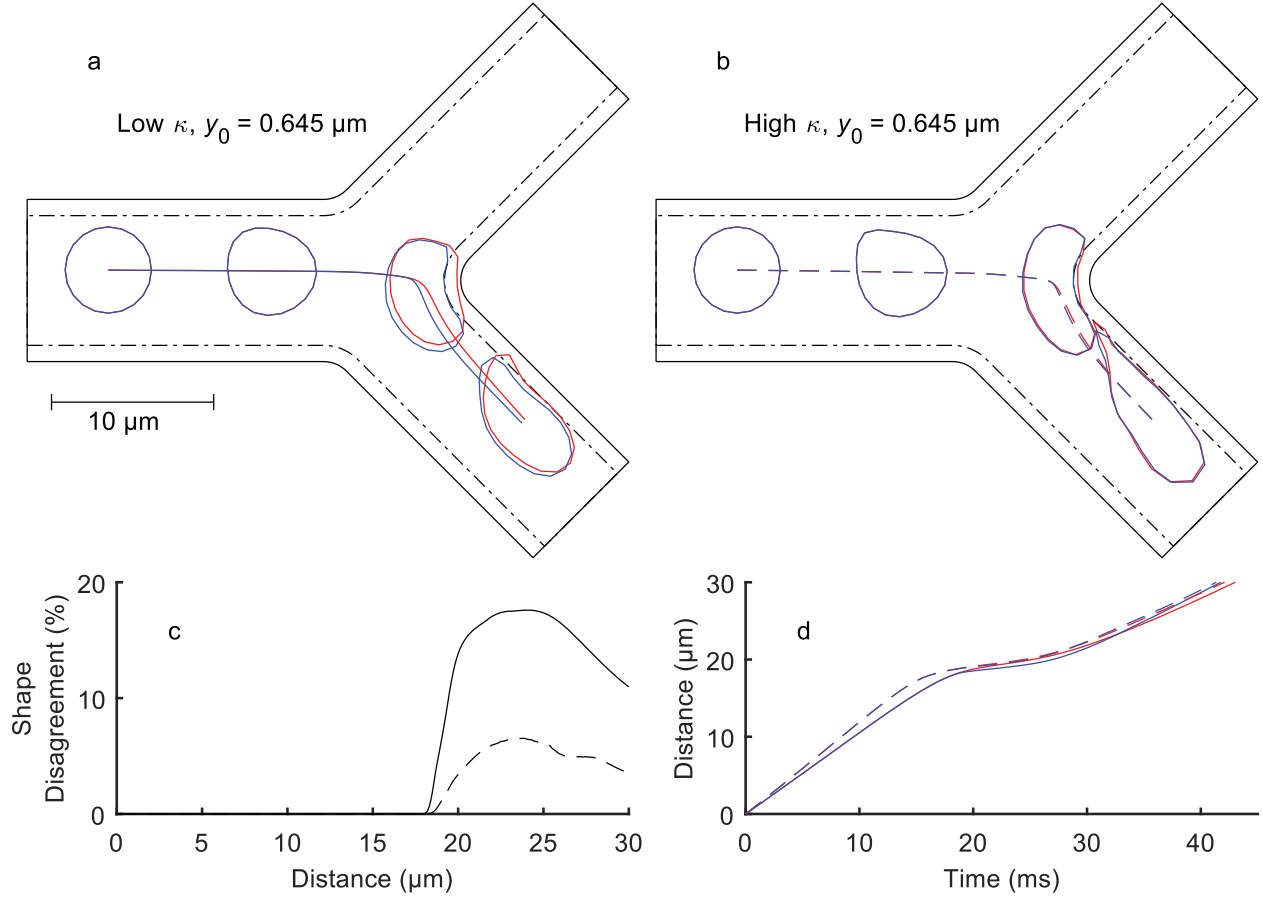
Figure 3.5. The effects of osmotic pressure difference in the ESL on cell shape and speed for $\Psi_1 = 0.375$. Blue represents $\Delta\pi_p = 200$ dyn/cm^2 and red represents $\Delta\pi_p = 20$ dyn/cm^2. Snapshots of RBCs at 0, 10, 20, and 30 µm traveled are plotted with the cell streamlines, initialized at $y_0 = 0.645$ µm for **(a)** $\kappa = 10^6$ dyn·s/cm^4 as solid curves and **(b)** $\kappa = 10^8$ dyn·s/cm^4 as dashed curves. **(c)** Shape disagreement percentage between the cells in **(a)** and **(b)** are plotted with solid and dashed curves, respectively. **(d)** Distance traveled by each cell as a function of the time spent traversing the bifurcation.

width of the ESL, w, is seen for the high osmotic pressure difference and high hydraulic resistivity case, while 92.1% is seen for the low osmotic pressure difference and low hydraulic resistivity case, an increase of thirty-fold.

Figure 3.6b shows ESL penetration as a function of time for multiple simulations with cells initialized at cell center y-values of $y_0 = 0.645$ µm, which was chosen to be near and below y_c for all cases. The plot is representative of behavior seen in simulations where a significant amount of penetration occurs. In cases of low osmotic pressure difference, penetration is not

localized in time, as once a maximum penetration distance is reached by the cell, it tends to remain near that penetration distance for a significant amount of time. For cases of high osmotic pressure difference, the time a cell spends near the maximum penetration distance is shortened.

For the flow split $\Psi_1 = 0.375$, Table 3.3 gives the average time a cell takes to travel 30 µm and navigate the bifurcation, $\bar{t}_p$, the average maximum penetration distance into the ESL, $\bar{\delta}_{max}$, and the critical initial cell center y-value, y_c, for a range of hydraulic resistivities at both low and high osmotic pressure differences. For example, the cell that penetrates the ESL most in Figure 3.5a corresponds to the lowest nonzero values of hydraulic resistivity and osmotic pressure differences. The corresponding average penetration distance into the ESL for such cases can be found in Table 3.3 as 0.526 µm. As before, the extreme cases of $\kappa = 0$, $\Delta\pi_p = 0$ and $\kappa \to \infty$, $\Delta\pi_p \to \infty$ are included for comparison.

In general, a lower hydraulic resistivity in the ESL leads to longer average passage times as the background fluid flow is less centralized, as noted in Figure 3.2. Lowering osmotic pressure difference also increases average passages times as cells are able to penetrate farther in the ESL. The hydraulic resistivity into the ESL also affects penetration distances. For lower levels, when cells approach the ESL at the bifurcation, the fluid in between the cell and the ESL is able to flow not only along the ESL boundary, but through the ESL as well. This allows for cells to more quickly and deeply penetrate into the ESL region. For the extreme cases when no ESL, or an impermeable ESL, is present, cells travel through the bifurcation more quickly.

3.4   Discussion

Though by a relatively small margin, the partitioning behavior of RBCs is influenced by the hydraulic resistivity and osmotic pressure difference in the ESL. This effect may be explained by an increased obstruction effect taking place, as described by Barber et al. [26]. At lower osmotic pressure differences, the ESL resists compression less and allows the cell to penetrate the ESL more deeply. This moves it away from the main flow region allowing it to obstruct the low flow branch less in general. This is in contrast to the effects of higher osmotic
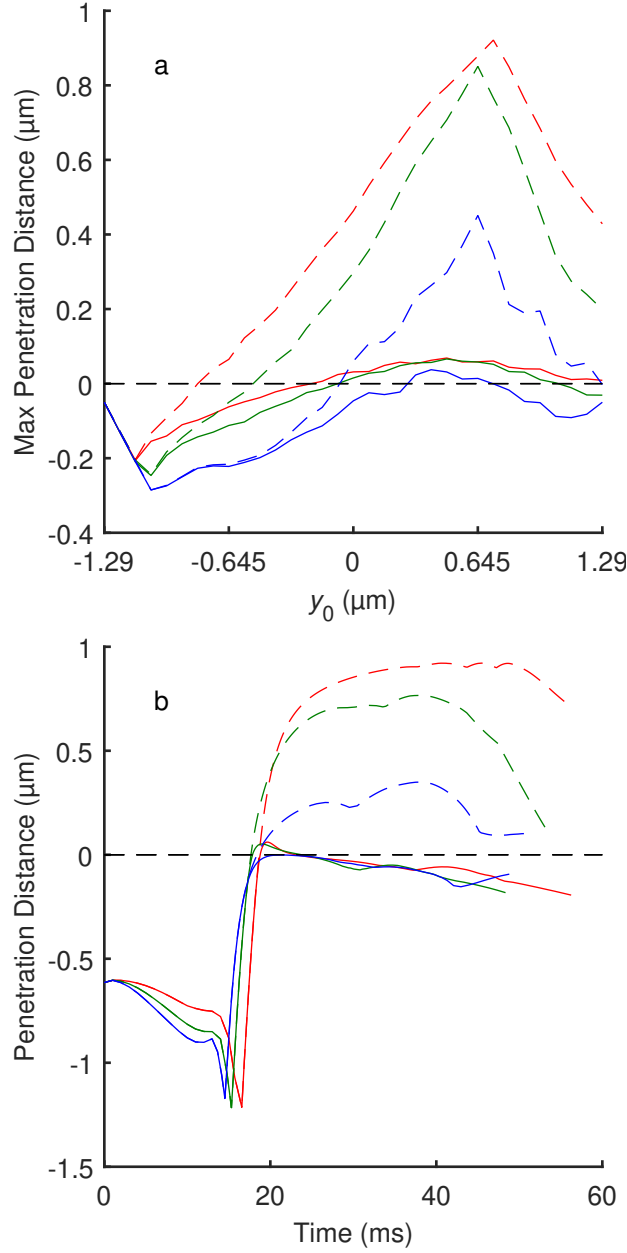
Figure 3.6. The effects of hydraulic resistivity and osmotic pressure difference on RBC penetration distance into the ESL for $\Psi_1 = 0.375$. Red, green, and blue curves represent $\kappa = 10^6$, 10^7, and 10^8 dyn·s/cm^4, respectively. Dashed and solid curves represent $\Delta\pi_p = 20$ and 200 dyn/cm^2, respectively. **(a)** Maximum penetration distance into the ESL as a function of initial cell center y-values. **(b)** Penetration distance into the ESL as a function of time. Each RBC was initialized at $y_0 = 0.645$ µm.

Table 3.3.

Average passage times, $\bar{t}_p$, average maximum penetration distances, $\bar{\delta}_{max}$, and critical y-values, y_c, at multiple combinations of hydraulic resistivity and osmotic pressure difference for $\Psi_1 = 0.375$. Low and high osmotic pressure differences correspond to $\Delta\pi_p = 20$ and 200 dyn/cm^2, respectively, unless otherwise noted.

κ (dyn·s/cm^4)	$0, \Delta\pi_p = 0$	10^6	10^7	10^8	$\infty, \Delta\pi_p \to \infty$
$\bar{t}_{p,low}$ (ms)	26.43	31.43	29.05	27.43	26.88
$\bar{t}_{p,high}$ (ms)	26.43	30.91	28.70	27.26	26.88
$\bar{\delta}_{max,low}$ (µm)	0	0.526	0.426	0.208	0
$\bar{\delta}_{max,high}$ (µm)	0	0.041	0.039	0.025	0
$y_{c,low}$ (µm)	0.766	0.766	0.685	0.685	0.685
$y_{c,high}$ (µm)	0.766	0.685	0.685	0.685	0.685

pressure difference where the ESL resists compression from the cell much more and penetrates the ESL much less. This increases the relative amount that the cell tends to obstruct low flow branches and tends to pull cells into the low flow branch. Higher resistance in the ESL prevents fluid from flowing through it as quickly which leads to cells at the mouth of the low flow daughter branch more completely blocking the flow at that branch when compared to a case with lower resistance in the ESL. At the same time, cells deform slightly less for lower hydraulic resistivities and their rounder shapes tend to obstruct downstream branches more. The net result of these factors, as seen in Figure 3.2b, is enhanced obstruction in the higher hydraulic resistance cases. At the same time, at higher hydraulic resistivity, more shear force is felt by the cell. This is due to a more centralized flow profile, which is a consequence of the lower flow through the ESL in the more resistive case, as can be seen by the flow profiles pictured in Figure 3.2b. In the same figure, it can be seen that a higher shear rate leads to more deformation in the cell shape, which agrees with previous studies [59]. Generally speaking, more cell deformation leads to a greater rate of cell migration towards the center of the mother vessel upstream of the bifurcation and away from the low flow branch. However, the migration effect, in general, is not as strong as the obstruction effect.

Outside of partitioning effects, the strength of the hydraulic resistivity in the ESL can produce differences in the shape and speed of RBCs. Higher hydraulic resistivity in the ESL results in a greater shear rate in the non-ESL region near the ESL boundary. As can be seen in Figure 3.3c even in the mother vessel before the bifurcation, the shapes of the cells in the low and high hydraulic resistivity cases differ, with the differences increasing when cells are initialized closer to the ESL. When the cell comes into contact with the ESL at the far end of the bifurcation however, much larger shape disagreements are seen especially when cells travel down the high flow daughter branch. Since more cells wind up traveling down the high flow branch, cells initialized near the critical initial y-value will travel farther in close contact with the ESL than those traveling down the low flow daughter branch. This can also be seen in Figure 3.4, as after contact with the ESL in the bifurcation at 20 and 30 µm traveled, shape disagreement spikes for the initial y-values close to the critical initial y-value on the high flow daughter branch side. A similar spike is not seen however, on the low flow daughter branch side of the graph. This indicates that greater interaction with the ESL correlates with higher deformation in RBCs. After initial contact with the ESL, shape disagreements level off slightly, but remain at a significant level as the cell travels farther down a daughter branch. Higher hydraulic resistivity in the ESL also results in faster RBCs in bifurcations, as seen in Figure 3.3d. Before reaching the bifurcation, faster speeds in the high hydraulic resistivity case can be explained by greater fluid velocity in the free flowing region that compensates for the lower fluid velocity in the ESL region. Once reaching the bifurcation however, the gap in speed between the two levels of hydraulic resistivity in the ESL is slightly increased at the bifurcation especially in the case of the cells traveling down the low flow daughter branch. This has to do with the fact that cells with lower hydraulic resistivity are able to penetrate and flatten against the ESL more easily due to increased circulation in the ESL region underneath such cells. It takes time for cells to penetrate and then recover from an ESL incursion. Table 3.3 confirms the general trend in terms of hydraulic resistivity travel speed with lower hydraulic resistivity simulations experiencing approximately 4 ms greater passage times than higher hydraulic resistivity simulations.

Similar results hold for osmotic pressure differences in the ESL. When only comparing differences of osmotic pressure difference in the ESL, there will be no shape disagreement

before the bifurcation, as osmotic pressure differences in the ESL have no impact on fluid flow, and so does not have an effect on shear. After coming into contact with the ESL in the bifurcation however, there is significant shape disagreement especially in the case of lower hydraulic resistivity, as plotted in Figure 3.5c. While shape disagreement peaks immediately after the cells come into contact with the ESL at the bifurcation, note how in Figure 3.5a the reduction and leveling off of shape disagreement corresponds to a gradual repelling of the RBC from the ESL. This indicates that greater interaction with the ESL produced by a lower osmotic pressure difference or lower hydraulic resistivity in the ESL can lead to greater deformation of RBCs when in bifurcations. Lower osmotic pressure difference in the ESL also results in slower RBCs in bifurcations, as seen in Figure 3.5d. When impacting the ESL at the bifurcation, a clear and sustained slowing of the RBCs occurs in the low osmotic pressure difference cases at both low and high hydraulic resistivity. This indicates that lower osmotic pressure differences in the ESL impedes the progress of RBCs at bifurcations when compared to higher osmotic pressure differences.

Based on these results, it is clear that greater interaction between the ESL and RBCs occurs in scenarios involving lower values of the parameters of hydraulic resistivity and osmotic pressure difference in the ESL leading to the increased deformation and decreased speed of RBCs. The RBCs increased interaction in these scenarios is intrinsically tied to their ability to penetrate into the ESL region. Reducing either or both the hydraulic resistivity and osmotic pressure difference in the ESL results in a dramatic increase in an RBCs maximum penetration distance into the ESL as seen in Figure 3.6a, as well as the length of time an RBC spends impinging upon the ESL as seen in Figure 3.6b. Lower osmotic pressure difference especially allows the RBC to penetrate more deeply into the ESL, as seen clearly in Table 3.3. At low osmotic pressure difference, the ESL is on average penetrated from 20-52% of its width across the full range of hydraulic resistivities considered here. This is in contrast to high osmotic pressure difference where the ESL is on average penetrated from 2-4% of its width across the same range of hydraulic resistivities. These differences in ESL penetration could explain the effects interaction with the ESL at bifurcations have on RBC deformation and speed.

Throughout this chapter, cell-to-cell interactions have been neglected, corresponding to a low hematocrit. Isolated RBCs tend to migrate towards the centerline of the mother vessel, indicating that the distribution upstream of the bifurcation of these RBCs depends on the distance they have traveled. By including cell-cell interactions, as is the case in the following chapter, these effects are mitigated which expands the upstream distribution of RBCs. Higher hematocrit levels have also been observed to promote more uniform partitioning [16]. There are also other limitations such as the use of a two-dimensional model, a set geometry, and a set upstream distribution (see Chapter 5 for more details).

In summary, the partitioning, deformation and ESL penetration of RBCs is affected by the hydraulic resistivity and osmotic pressure difference in the ESL. Increased obstruction effects for increased hydraulic resistivity promote uniform partitioning, but only by a relatively small margin. Increased flow centralization and an increased resistance to compression correspond to increased levels of hydraulic resistivity and osmotic pressure difference, respectively, which correlates with increased deformation. An increased resistance to compression also correlates with decreased ESL penetration, which helps to explain deformation effects as well as the increased speed at which cells in such scenarios traverse bifurcations.

4. THE EFFECT OF CELL TO CELL INTERACTIONS ON THE BEHAVIOR OF RED BLOOD CELLS IN ESL-LINED DIVERGING CAPILLARY BIFURCATIONS

4.1 Introduction

Forty to forty-five percent of blood is composed of red blood cells (RBCs) making cell-cell interactions very important during the partitioning process. In fact, past experimental studies have found significant dependence of RBC partitioning on discharge hematocrit [16]. Combining this with the increasingly recognized importance of the endothelial surface layer (ESL) and the correlation of ESL pathologies with other diseases, discussed in Chapter 1, suggests investigating how partitioning and overall RBC dynamics at nonzero hematocrits may be affected by changes in ESL properties. To better understand how cell-cell interactions may vary as ESL properties change, the model developed in Chapter 2 is used here to consider RBCs moving two at a time through a microvessel bifurcation lined with an explicitly modeled ESL. As in the simulations of isolated RBCs studied in Chapter 3, the study considers the effects of hydraulic resistivity and osmotic pressure difference on RBC partitioning, deformation, and ESL penetration.

Possible mechanical explanations for the observed trends are identified by comparing the results with corresponding results for isolated cells, as well as past studies on RBC interactions in vessels without an explicitly modeled ESL region. Barber et al. [26] identified three primary interactions between cells that led to changes in RBC partitioning behavior when compared to isolated cells. The trade-off effect occurs when the leading cell entering a daughter branch influences the following cell to enter the opposite branch. The herding effect occurs when the following cell entering a daughter branch causes the leading cell to enter that same branch. The following effect occurs when the leading cell entering a daughter branch causes the following cell to enter that same branch. Considering these three effects allow us to discuss and classify the underlying mechanical effects through which the ESL influences RBC partitioning in paired cell scenarios.

4.2 Methods

The initial shape of the RBCs for every simulation is taken to be a circle with radius $R_{cell} = 2.66$ µm. The center of the leading or front cell is initialized in the fluid at location $(x, y) = (-15$ µm, $y_{0,f})$. The motion of this cell is integrated by itself for either a prescribed time Δt_0 or a prescribed distance Δd_0 before the center of the following or back cell is initialized in the fluid at location $(x, y) = (-15$ µm, $y_{0,b})$. Both $y_{0,f}$ and $y_{0,b}$ are contained in the interval $[y_b, y_t] = [-1.29, 1.29]$. The motion of both cells are then integrated until their partitioning behavior can be determined. Time delayed release (Δt_0) was used in portions of the study because the method for estimating partitioning, taken from [26], uses probability distributions that are easiest to define in terms of time. Distance delayed release (Δd_0) was used in other portions of the study to allow for more consistent comparisons between simulations with various flow profiles due to the hydraulic resistivity in the ESL.

The branching domain considered here is as seen in Figure 2.2a, and is representative of a diverging vessel bifurcation in a capillary network. The mother branch has a width of $w_0 = 10$ µm, including a $w = 1$ µm wide ESL. The daughter branches have widths of $w_1 = w_2 = 8.35$ µm, including the $w = 1$ µm wide ESL. Equal branching angles of 45° are considered. The total flow rate is $Q_0 = 8 \times 10^{-3}$ cm^2/s for cases including an ESL, and $Q_0 = 10 \times 10^{-3}$ cm^2/s for the no-ESL/10 µm wide scenario. The flow split or fraction of bulk blood flow into the upper daughter branch is given by $\Psi_1 = Q_1/Q_0$, where Q_1 is the flux at the outlet of the upper daughter branch.

The same values for the maximum hydraulic resistivity and osmotic pressure differences used for isolated cells in Chapter 3 are used here: $\kappa = 0$, 1×10^6 dyn·s/cm^4, 1×10^7 dyn·s/cm^4, 1×10^8 dyn·s/cm^4, and ∞ and $\Delta\pi_p = 20$ dyn/cm^2, 200 dyn/cm^2. To estimate cell partitioning behavior, the same criteria are used as in the single cell simulations to determine if an RBC has transitioning from the mother vessel to a specific daughter branch, as described in section 3.2. If these criteria are not met due to a numerical failure causing the simulation to stop before a determination has been made, the simulation is examined by hand to determine which daughter branch the cell enters. There were no cases where a determination could not be made.

As noted in section 3.2, a branch function for single cells initialized at fluid location $(x, y) = (-15\ \mu m, y_0)$ traveling through a bifurcation can be defined by the following:

$$b_1(\Psi_1, y_0) = \begin{cases} 1 & \text{if the RBC enters the top branch} \\ 0 & \text{if the RBC enters the bottom branch} \end{cases} . \tag{4.1}$$

Similarly, branch functions can be defined for two cells traveling through a bifurcation. For two cells whose initialization corresponds to $(y_{0,f}, y_{0,b}, \Delta t_0)$, they are defined by the following:

$$b_{2,f}(\Psi_1, y_{0,f}, y_{0,b}, \Delta t_0) = \begin{cases} 1 & \text{if the leading cell enters the top branch} \\ 0 & \text{if the leading cell enters the bottom branch} \end{cases} , \tag{4.2}$$

$$b_{2,b}(\Psi_1, y_{0,f}, y_{0,b}, \Delta t_0) = \begin{cases} 1 & \text{if the following cell enters the top branch} \\ 0 & \text{if the following cell enters the bottom branch} \end{cases} . \tag{4.3}$$

Similar branch functions may be defined for Δd_0. For each combination of flow split Ψ_1 and either time delay Δt_0 or distance delay Δd_0, the curves Γ_f (for $b_{2,f}$) and Γ_b (for $b_{2,b}$) separate the branch function values of 1 and 0 from each other in the $y_{0,f} - y_{0,b}$ plane.

For a given flow split Ψ_1 and either time delay Δt_0 or distance delay Δd_0, the value of a branch function in the $y_{0,f} - y_{0,b}$ plane is estimated using a simple interface-finding algorithm. To start the algorithm, we first test the 2×2 grid of corner points of (y_b, y_b), (y_b, y_t), (y_t, y_b), and (y_t, y_t). We then repeatedly refine the grid in two nested stages. The first stage tests all points in the center of the smallest squares of previously tested points. These newly tested points are then added to the grid creating a grid of diamonds except along the edges where we have half diamonds or triangles. The second stage tests the centers of the diamonds. Along the edges, points on the edge halfway between existing edge points are tested. The newly tested points added to the old points form a new grid of squares once again. These two stages are repeated until the desired level of refinement is reached, which in these studies culminates in a 17×17 grid of tested points.

To "test" points, we can run simulations for a specific $(y_{0,f}, y_{0,b})$, see which branch each cell enters, and then set $b_2 2, f$ and $b_{2,b}$ to 0 or 1, as is appropriate. Testing every point in

this fashion, however, is computationally expensive. To more efficiently obtain the branching function, we assume that if the points nearest to a point of interest, $(y_{0,f}, y_{0,b})$, have all been tested and found to have the exact same partitioning behavior, then the point inside of the enclosed square/diamond/triangle probably has the same behavior. That point is then assigned the corresponding $b_{2,f}$ and $b_{2,b}$ without the need to run a simulation.

The separating curves Γ_f and Γ_b are assumed to be halfway between places where the branching function values are known to be 0 and 1. In particular, we look at each row and column and find when two adjacent grid points in the row or column are 0 on one side and 1 on the other. We then assume that the Γ curve passes through the point halfway between the two grid points. All such points are connected by line segments to provide the estimated separating curves Γ_f and Γ_b for the leading and following cell, respectively.

The minimum time delay between the initialization of the leading and following cells, $\Delta t_{0,\text{min}}(y_{0,f}, y_{0,b})$, such that the minimum distance between the cells is exactly 0.01 µm, is uniquely determined for each pair of initial cell center y-values $(y_{0,f}, y_{0,b})$. To calculate this minimum time delay, the motion of the leading cell is first integrated for a time greater than the minimum time delay. Next, the following cell is initialized in the fluid as described previously. Finally, the positions of the nodes of the leading cell are interpolated with respect to time to locate the set of positions that lead to a minimum distance from the following cell of exactly 0.01 µm. Any $\Delta t_0 < \Delta t_{0,\text{min}}$ is not considered due to the unrealistic scenarios it would produce in simulations. The maximum time delay between the initialization of the leading and following cells considered in this study is chosen as $\Delta t_{0,\text{max}} = 20$ ms to match the value used by Barber et al. [26], which corresponds to a sufficient separation between cells such that the cells have little to no significant influence on one another.

As noted in section 3.2, the RBC flux into the top or first daughter branch as a fraction of the total RBC flux into both daughter branches, Φ_1, can be estimated for isolated RBCs at a prescribed flow split, Ψ_1, by the following:

$$\Phi_1(\Psi_1) = \int_{y_b}^{y_t} p_1(y_0) b_1(\Psi_1, y_0) dy_0. \tag{4.4}$$

The density function $p_1(y_0)$ describes the probability that the center of a cell passes through $y = y_0$ when the center of the cell passes through $x = x_0 = -15$ μm, and is calculated as follows:

$$p_1(y_0) = \frac{u_d(y_0)}{\int_{y_b}^{y_t} u_d(y)dy}. \tag{4.5}$$

Here, $u_d(y)$ is the distribution of the velocities upstream of the bifurcation.

Similarly, the fractional flux of leading and following cells entering the top daughter branch for a particular time delay Δt_0 at a prescribed flow split, Ψ_1, may be defined by the following:

$$
\begin{aligned}
\Phi_{1,f}(\Psi_1, \Delta t_0) &= \int_{y_b}^{y_t} \int_{y_b}^{y_t} p_1(y_{0,f}) p_1(y_{0,b}) b_{1,f}(\Psi_1, y_{0,f}, y_{0,b}, \Delta t_0) dy_{0,f} dy_{0,b}; \\
\Phi_{1,b}(\Psi_1, \Delta t_0) &= \int_{y_b}^{y_t} \int_{y_b}^{y_t} p_1(y_{0,f}) p_1(y_{0,b}) b_{1,b}(\Psi_1, y_{0,f}, y_{0,b}, \Delta t_0) dy_{0,f} dy_{0,b}.
\end{aligned} \tag{4.6}
$$

Similar expressions may be written for $\Phi_{1,f}(\Psi_1, \Delta d_0)$ and $\Phi_{1,b}(\Psi_1, \Delta d_0)$.

Integrating over all possible time delays $(\Delta t_{0,\min}(y_{0,f}, y_{0,b}) < \Delta t_0 < \Delta t_{0,\max})$, we have the fractional flux of all paired leading and following cells entering the top daughter branch, as follows:

$$
\begin{aligned}
\Phi_{1,f}(\Psi_1) &= \frac{\iiint_\Omega p_1(y_{0,f}) p_1(y_{0,b}) b_{1,f}(\Psi_1, y_{0,f}, y_{0,b}, \Delta t_0) d\Omega}{\iiint_\Omega p_1(y_{0,f}) p_1(y_{0,b}) d\Omega}; \\
\Phi_{1,b}(\Psi_1) &= \frac{\iiint_\Omega p_1(y_{0,f}) p_1(y_{0,b}) b_{1,b}(\Psi_1, y_{0,f}, y_{0,b}, \Delta t_0) d\Omega}{\iiint_\Omega p_1(y_{0,f}) p_1(y_{0,b}) d\Omega},
\end{aligned} \tag{4.7}
$$

where Ω is the set of all possible $(y_{0,f}, y_{0,b}, \Delta t_0)$. We note that while explicit probability distribution functions are included for $y_{0,f}$ and $y_{0,b}$ (p_1), the effective probability distribution for the time delay, Δt_0, is a constant/uniform distribution. The fractional flux of all paired cells entering the top daughter branch is then the average the above two equations:

$$\Phi_{1,2}(\Psi_1) = \frac{1}{2}(\Phi_{1,f}(\Psi_1) + \Phi_{1,b}(\Psi_1)). \tag{4.8}$$

Also considered is the effect of hydraulic resistivity and osmotic pressure difference on RBC deformations in diverging vessel bifurcations. For simulations involving two RBCs,

deformation magnitude is estimated using two deformation metrics. The first is the mean linear strain of the external segments:

$$\lambda_s = \frac{1}{n} \sum_{i=1}^{n} \frac{|l_i - l_0|}{l_0}, \tag{4.9}$$

where l_i is the length of the ith external segment, l_0 is the reference length of the external segment, and n is the number of external nodes in the discretized cell membrane. The second is a measure of the mean bending angle:

$$\lambda_b = \frac{1}{n} \sum_{i=1}^{n} |\alpha_i|, \tag{4.10}$$

where α_i is the exterior angle between adjacent external segments. This provides an estimate for how much the membrane has been bent.

As noted in section 3.2 for single cell simulations, to best isolate effects due only to deformation and not translation, we compare cells that have traveled the same distance as opposed to comparing cells that have traveled for the same time. This requires linear interpolation with respect to the distance traveled by the cells in question. For two cell simulations, we perform similar comparisons between cells that have traveled the same distance. However, due to the increased complexity in such systems (two cells versus one), results often depend on two $(y_{0,f}, y_{0,b})$ not just one (y_0) degree of freedom. Hence comparisons produce three-dimensional data in $y_{0,f} - y_{0,b}$ space. While our testing strategy that is used to estimate partitioning behavior provides estimates for branching function values at all locations on a regular 17×17 grid, since simulations are run only when needed, deformation and penetration information is only known at a select few locations on that grid. In particular, deformation and penetration information is known primarily at points near the separating curves Γ_f and Γ_b. An exception to this is the 33 points tested along the level surface $y_{0,b} = 0.968$ to better compare penetration plots in Figure 4.8. In a sense, this is a reasonable sampling as it samples more points close to the separating curves where we expect larger variations in deformation and penetration behaviors as cells take more time to

79

negotiate the bifurcation. Nonetheless, the available locations for such behavioral data are scattered and not on a regular grid.

To better visualize and provide estimates for deformation and penetration behavior across the entire $y_{0,f} - y_{0,b}$ space, we use radial basis function (RBF) interpolation. For N data points $f_{SIM}^j(\boldsymbol{x}_j)$ collected from N locations $\boldsymbol{x}_j$, the interpolant takes the following form:

$$f_{RBF}(\boldsymbol{x}) = \sum_{i=1}^{N} w_i \phi(\|\boldsymbol{x} - \boldsymbol{x}_i\|_2), \qquad (4.11)$$

where $\phi(r)$ is a multiquadratic family of radial basis functions of the form:

$$\phi(r) = \sqrt{r^2 - r_0^2}. \qquad (4.12)$$

The value of r_0 is generally taken to be greater than the minimal distance between data points, yet less than the maximal distance [60], [61]. In this case, the parameter is taken to be $r_0 = 0.0806$, or just above the minimum distance between data points. The weights, w_i, are precomputed by solving:

$$f_{SIM}^j(\boldsymbol{x}_j) = \sum_{i=1}^{N} w_i \phi(\|\boldsymbol{x}_j - \boldsymbol{x}_i\|_2). \qquad (4.13)$$

How deeply an RBC invades or penetrates into the ESL region is considered using the same method for single cells described in section 3.2. The penetration of the leading and following cells is given by:

$$\delta_f(t, y_{0,f}) = w - \min_{s_B, s_C} \|\boldsymbol{B}(s_B) - \boldsymbol{C}_f(s_C)\|_2 \,;$$
$$\delta_b(t, y_{0,b}) = w - \min_{s_B, s_C} \|\boldsymbol{B}(s_B) - \boldsymbol{C}_b(s_C)\|_2 \,, \qquad (4.14)$$

where $\boldsymbol{B}(s_B)$ is a parametrization of the boundary curve corresponding to the vessel wall and $\boldsymbol{C}_f(s_C)$ and $\boldsymbol{C}_b(s_C)$ are parametrizations of the leading and following cells' discretized membrane curve. This produces a positive value for RBCs penetrating past the middle of the diffuse boundary of the ESL and a negative value for RBCs before that midpoint.

4.3 Results

Figure 4.1 illustrates the three primary effects initiated by changes in the hydraulic resistivity that alter cell-cell interactions in a diverging microvessel bifurcation. These representative simulations were produced using a flow split of $\Psi_1 = 0.375$, a set distance interval of $\Delta d_0 = 7.5$ µm between cells, a high osmotic pressure difference of $\Delta \pi_p = 200$ dyn/cm^2, and hydraulic resistivities ranging from $\kappa = 10^6 - 10^8$ dyn·s/cm^4. In each snapshot, the distances listed on the figure correspond to the distance traveled since the initialization in the mother vessel of the cell whose partitioning behavior is affected. Throughout the figure, the cells in red correspond to a simulation with the hydraulic resistivity of the ESL set at $\kappa = 10^6$ dyn·s/cm^4, those in green to $\kappa = 10^7$ dyn·s/cm^4, and those in blue to $\kappa = 10^8$ dyn·s/cm^4.

In Figure 4.1a, the cells were initialized at $(y_{0,f}, y_{0,b}) = (0.806, 0.484)$. The red cells undergo a version of the trade-off interaction where the back cell enters the low flow branch even though it would have entered the high flow branch if the front cell had not been there, while the front cell enters the high flow branch even though it would have entered the low flow branch if the back cell had not been there. For the green cells (higher ESL hydraulic resistivity), however, the back cell exhibits a new partitioning behavior and instead travels down the high flow branch due to the front cell blocking its entry into the low flow branch more than in the other case. This is an example of a "blockage" effect.

In Figure 4.1b, the cells were initialized at $(y_{0,f}, y_{0,b}) = (0.161, -0.323)$. The green cells exhibit standard partitioning behavior where the back cell enters the same branch it would have if the front cell had not been there and vice versa. Raising the hydraulic resistivity, however, causes the back cell to exhibit a new partitioning behavior as it travels down the opposite branch. The higher resistivity enhances the obstruction effect in general and, in this case, pulls the cell into the low flow branch. This is an example of an "obstruction" effect for paired cells.

Finally, in Figure 4.1c, the cells were initialized at $(y_{0,f}, y_{0,b}) = (0.645, -1.29)$. The green cells exhibit an interaction where the front cell enters the low flow branch even though it would have entered the high flow branch if the back cell had not been in close proximity to

it while entering the high flow branch itself. Increasing the hydraulic resistivity, however, centralizes the flow and effectively narrows the vessels. In that case, as the back cell squeezes through the narrower free flowing region into the bottom branch, it pulls the front cell with it in a standard herding interaction. In herding interactions, the back cell pulls the front cell into the high flow branch even though the front cell would have entered the low flow branch if the back cell had not been there. This is an example of a "pseudo herding" effect.

The estimated separating curves Γ_f and Γ_b for a flow split of $\Psi_1 = 0.375$, a high osmotic pressure difference of $\Delta\pi_p = 200$ dyn/cm^2, and a hydraulic resistivity in the ESL ranging from $\kappa = 10^6 - 10^8$ dyn·s/cm^4 are shown in Figure 4.2. Again, red, green, and blue curves correspond to low, medium, and high hydraulic resistivity in the ESL. Figures 4.2a and b illustrate the separating curves for the back cell in simulations with distance intervals $\Delta d_0 = 7.5$ and 10 µm between cells, respectively. Figures 4.2c and d show the same for front cells. For the back cell plots, above Γ_b we have that $b_{2,b} = 1$ which corresponds to a cell entering the upper branch. For the front cell plots, the same is true of $b_{2,f}$ to the right of Γ_f. The dashed lines on each plot correspond to the critical initial y-value of a cell's center above or to the right of which a single cell will enter the upper branch and below or to the left of which a single cell will enter the lower branch. Back cells are affected by the presence of an additional cell more than front cells. The deviation between Γ_f or Γ_b and the dashed lines decreases for higher Δd_0, especially for the front cell for which they nearly coincide. The gaps that arise between the Γ_b curves when the higher hydraulic resistivity curve is below the other in panel (a) represent obstruction behavior: the back cell enters the upper branch for the higher hydraulic resistivity case as a result of its interaction with the front cell. The more rare gaps that arise between the Γ_b curves when the higher hydraulic resistivity curve is above the other represent blockage behavior: the back cell enters the opposite branch as a result of its interaction with the front cell. The gaps that arise between the Γ_f curves in panel (b) represent pseudo herding behavior: the front cell enters the opposite branch as a result of its interaction with the back cell.

The overall effects of blockage, obstruction, and pseudo herding interactions on partitioning as a function of temporal cell spacing is shown in Figure 4.3 for a flow split of $\Psi_1 = 0.375$, a high osmotic pressure difference $\Delta\pi_p = 200$ dyn/cm^2, and a hydraulic resistivity in the
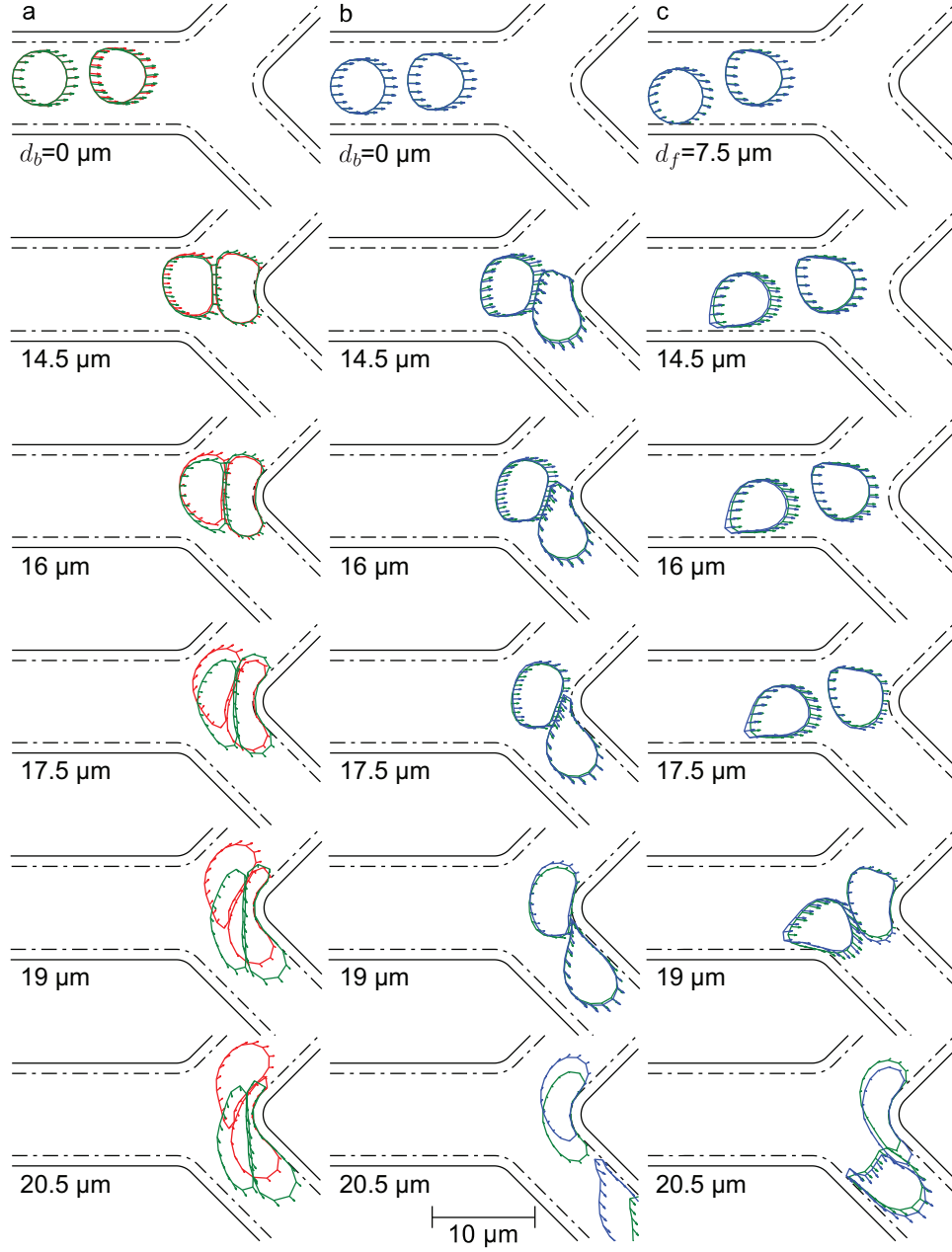
Figure 4.1. Effects of varying hydraulic resistivity on RBC interactions. Here $\Psi_1 = 0.375$, $\Delta d_0 = 7.5$ µm, and $\Delta \pi_p = 200$ dyn/cm^2. Simulations using ESL hydraulic resistivities of 10^6, 10^7, and 10^8 dyn·s/cm^4 are pictured in red, green, and blue, respectively. d_b and d_f are the distances traveled by the back and front cells, respectively. **(a)** Example of a blockage effect on the back cell. **(b)** Example of an obstruction effect on the back cell. **(c)** Example of a pseudo herding effect on the front cell.
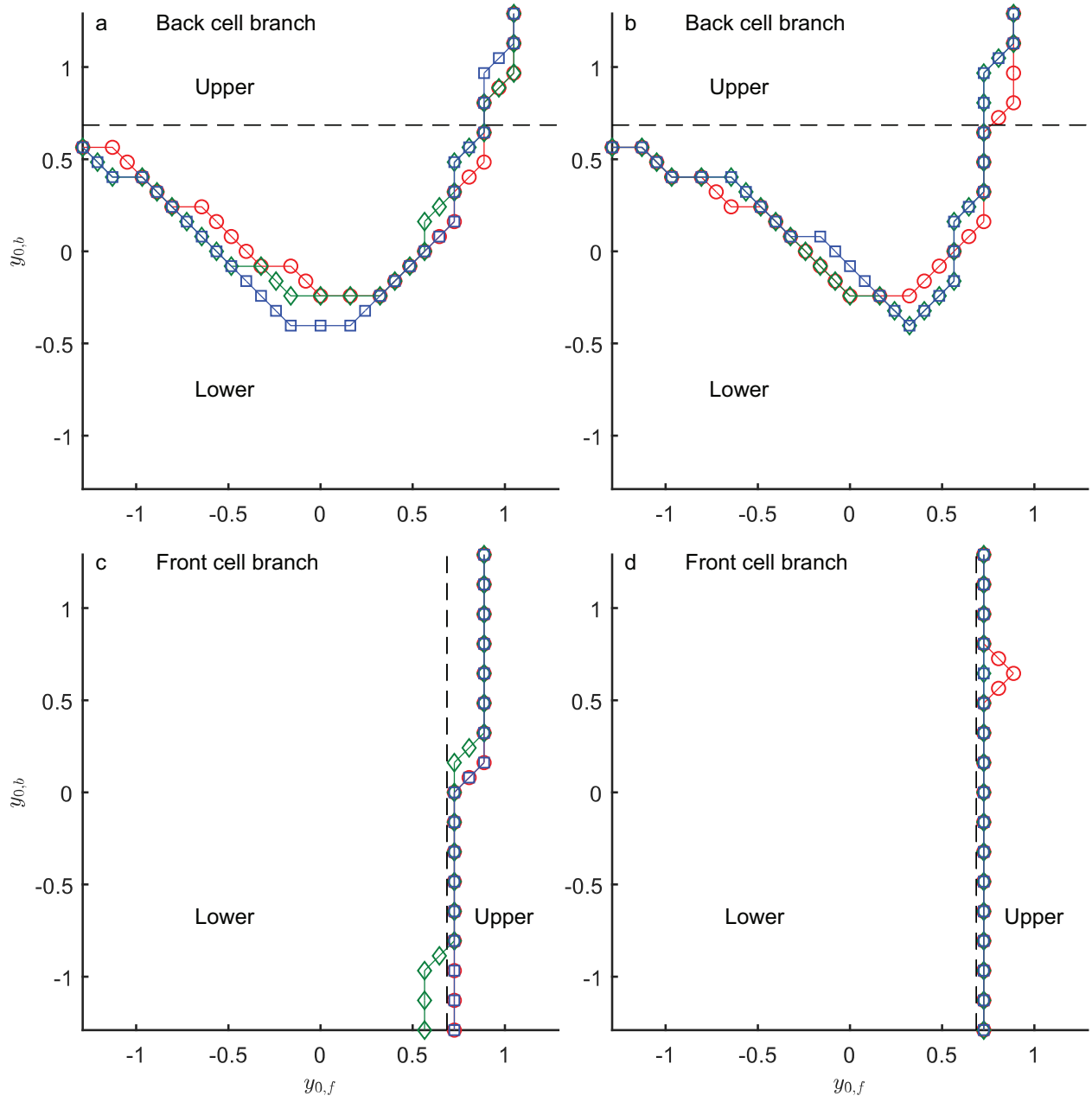
Figure 4.2. The effects of the hydraulic resistivity in the ESL on RBC partitioning behavior at a bifurcation for $\Psi_1 = 0.375$ and $\Delta \pi_p = 200$ dyn/cm^2. Cells from simulations with hydraulic resistivity in the ESL of 10^6, 10^7, and 10^8 dyn·s/cm^4 are pictured in red, green, and blue, respectively. The dashed lines on each plot correspond to the critical initial y-value of a cell's center above (back cell) or to the right (front cell) of which a single cell will enter the upper branch and below or to the left of which a single cell will enter the lower branch. **(a)** Γ_b for $\Delta d_0 = 7.5$ µm. **(b)** Γ_b for $\Delta d_0 = 10$ µm. **(c)** Γ_f for $\Delta d_0 = 7.5$ µm. **(d)** Γ_f for $\Delta d_0 = 10$ µm.

ESL ranging from $\kappa = 10^6 - 10^8$ dyn·s/cm^4. The percentage of front cells, back cells, and both cells entering the upper branch are plotted as dash-dotted, dashed, and solid curves, respectively. The dotted lines correspond to the percentage of cells entering the upper branch in single cell simulations. Again, red, green, and blue curves correspond to low, medium, and high hydraulic resistivity in the ESL. Data points along the curves with a filled symbol correspond to a set of simulations run with a defined distance interval, Δd_0, between cells instead of a time interval, Δt_0. The average time the front cell took to travel Δd_0 µm was calculated for these simulations and used as the Δt_0 coordinate on Figure 4.3. Simulations run with $\Delta d_0 = 7.5$ and 10 µm were included. Back cells are affected by the presence of an additional cell more than front cells. For smaller cell spacing, higher hydraulic resistivity in the ESL produces the greatest differential between paired cell results and those for isolated cells. However, for larger cell spacing, this trend reverses before approaching the isolated cell behavior. This reversal is in part due to spacing effects as a result of increased flow centralization for higher hydraulic resistivities, as discussed in more detail below.

Following Equation 4.7, we may integrate $\Phi_{1,f}$, $\Phi_{1,b}$, and $\Phi_{1,2}$ over all possible $y_{0,f}$, $y_{0,b}$, and Δt_0 to estimate the fraction of all paired cells entering the upper branch. The data for a flow split of $\Psi_1 = 0.375$ and a high osmotic pressure difference of $\Delta \pi_p = 200$ dyn/cm^2 is listed in Table 4.1, as well as Φ_1 for comparison to the partitioning behavior of single cell simulations. Uniform partitioning would then correspond to $\Phi_1 = 0.375$. In general, the addition of a second cell increases the uniformity of partitioning. However, varying the level of hydraulic resistivity in the ESL has little effect on partitioning behavior overall.

The analysis of cell shape deformation as an RBC travels through a microvessel bifurcation is complicated somewhat by simulation failure. Due to the close proximity of cells to one another, certain situations arise which are not accounted for by the model (see section 2.3 for more details), and the simulation must be terminated at that point. Therefore, complete comparisons can only be made across all simulations up to the shortest distance traveled in any particular simulation before termination is necessary. While partial comparisons using only simulations that do not terminate early are possible, the fact is that the cells that tend to experience early termination are also the cells that tend to be the most interesting as they start closest to the separating curves.
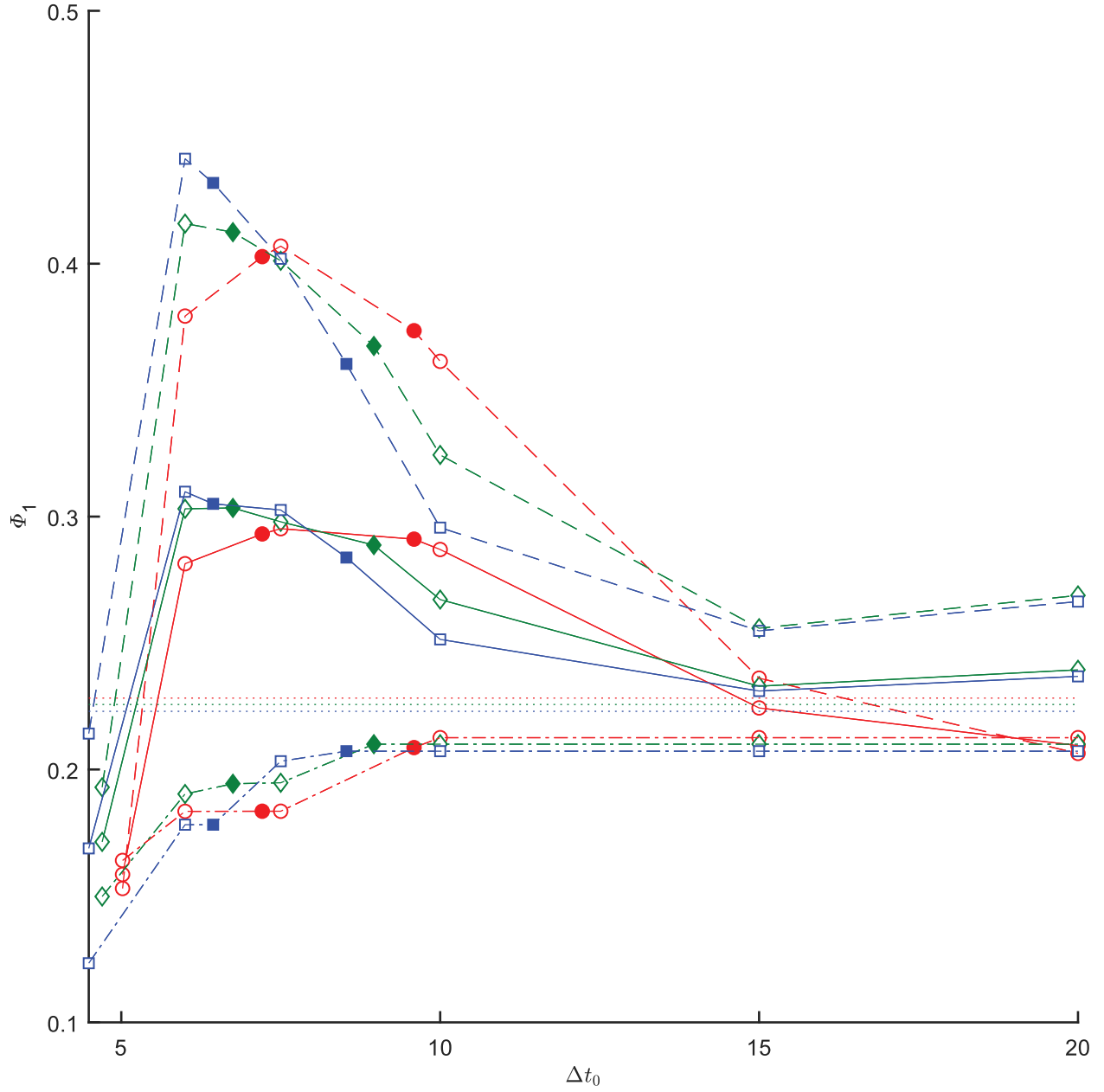
Figure 4.3. The overall effects of RBC interactions on partitioning as a function of Δt_0 for $\Psi_1 = 0.375$ and $\Delta \pi_p = 200$ dyn/cm^2. Cells from simulations with hydraulic resistivity in the ESL of 10^6, 10^7, and 10^8 dyn·s/cm^4 are pictured in red, green, and blue, respectively. Data points along the curves with a filled symbol correspond to a set of simulations run with a defined distance interval, Δd_0, between cells instead of a time interval, Δt_0. Plotted are $\Phi_{1,f}$ (dash-dotted), $\Phi_{1,b}$ (dashed), $\Phi_{1,2}$ (solid), and Φ_1 (dotted).

Table 4.1.

The fraction of all paired cells entering the upper branch for $\Psi_1 = 0.375$ and $\Delta\pi_p = 200$ dyn/cm^2 at varying values of κ.

κ (dyn·s/cm^4)	$\Phi_{1,f}(\Psi_1)$	$\Phi_{1,b}(\Psi_1)$	$\Phi_{1,2}(\Psi_1)$	$\Phi_1(\Psi_1)$
0	0.1935	0.2457	0.2196	0.1977
10^6	0.2047	0.2944	0.2496	0.2282
10^7	0.2036	0.3057	0.2547	0.2257
10^8	0.1998	0.3017	0.2507	0.2223
∞	0.1962	0.3028	0.2495	0.2222

In Figure 4.4, the average deformation over all possible coordinates $(y_{0,f}, y_{0,b})$ is shown across all simulations of each type up to the maximum possible common simulation distance for a flow split of $\Psi_1 = 0.375$. For two cell simulations, the simulations already obtained during the partitioning calculations were supplemented with more points from the 33×33 grid of $y_{0,f}$-$y_{0,b}$ space. This made enough points to cover approximately 15% of that grid. This data was used to create an interpolant using radial basis functions, as described above in section 4.2. This was then used to calculate the average deformation values used in Figure 4.4.

Figures 4.4a and b show, over distance traveled by the front cell, the mean linear strain, λ_s, at an external segment of the front cell and the mean bending angle, λ_b, at an external node between two external segments of the front cell, respectively. Figures 4.4c and d show the same for the back cell. In all plots, red, green, and blue curves correspond to low, medium, and high hydraulic resistivity in the ESL. Solid curves represent two cell simulations while dotted curves represent single cell simulations, both of which are simulated at a high osmotic pressure difference of $\Delta\pi_p = 200$ dyn/cm^2. The blue dashed curve and the blue dash-dotted curve represent high hydraulic resistivity in the ESL for a low osmotic pressure difference of $\Delta\pi_p = 20$ dyn/cm^2 for two cell and single cell simulations, respectively. All two cell simulations are computed at a distance interval of $\Delta d_0 = 7.5$ μm between cells. It is clear

that only two cell simulations computed at high hydraulic resistivity were able to run for long enough to get a complete picture of the average effects of the ESL on cell shape deformation at the microvessel bifurcation. In general, increased hydraulic resistivity enhanced deformations in terms of both strain and bending. The addition of cell-cell interactions dramatically increased both metrics compared to isolated cells at the bifurcation, especially for front cells.

In Figure 4.5, the same two deformation metrics, λ_s and λ_b, are plotted on the $y_{0,f} - y_{0,b}$ plane for a flow split of $\Psi_1 = 0.375$, a high osmotic pressure difference of $\Delta\pi_p = 200$ dyn/cm^2, a high hydraulic resistivity in the ESL of $\kappa = 10^8$ dyn·s/cm^4, and a distance interval of $\Delta d_0 = 7.5$ µm between cells. Figures 4.5a and b show the plots for the cell shape deformation of the front cell, and Figures 4.5c and d show the same for the back cell. The red circles on each plot correspond to actual simulated data points, while the rest of the surface is comprised of interpolated points as described above. Each two cell surface is compared to the corresponding single cell surface, which for the front cell plots is constant in the $y_{0,b}$ direction and for the back cell plots is constant in the $y_{0,f}$ direction. All plots are shown at the maximum distance traveled by all simulations involved, which for front cells is equal to 20.3 µm and for back cells is equal to 19.2 µm. For front cells, the presence of an additional exaggerates the peaks in strain and bending along the separating cell curve, Γ_f, compared to isolated cells, though not by the same magnitude along the entire curve. Peaks and troughs in the topography for back cells mirror to some extent those seen for front cells.

To better understand how cell-cell interactions may affect deformation, simulations for three data points from the surfaces in Figure 4.5 (filled pink circles) were run and compared with isolated cell runs. The three data points were chosen to show a range of dynamics that occur when high, medium, and low deformation levels are seen for the front and back cells. Figure 4.6 illustrates comparisons of the front cell with isolated cell runs while Figure 4.7 compares the back cell with isolated cell runs.

In Figure 4.6a, the cells were initialized at $(y_{0,f}, y_{0,b}) = (0.806, 1.29)$. After both cells had traveled 20.3 µm, the mean strain, λ_s, increased from 0.060 for the single cell to 0.188 for the front cell (213%) and the value of λ_b increased from 0.399 for the single cell to 0.462 for the front cell (16%). In Figure 4.6b, the cells were initialized at $(y_{0,f}, y_{0,b}) = (0.645, -0.323)$.
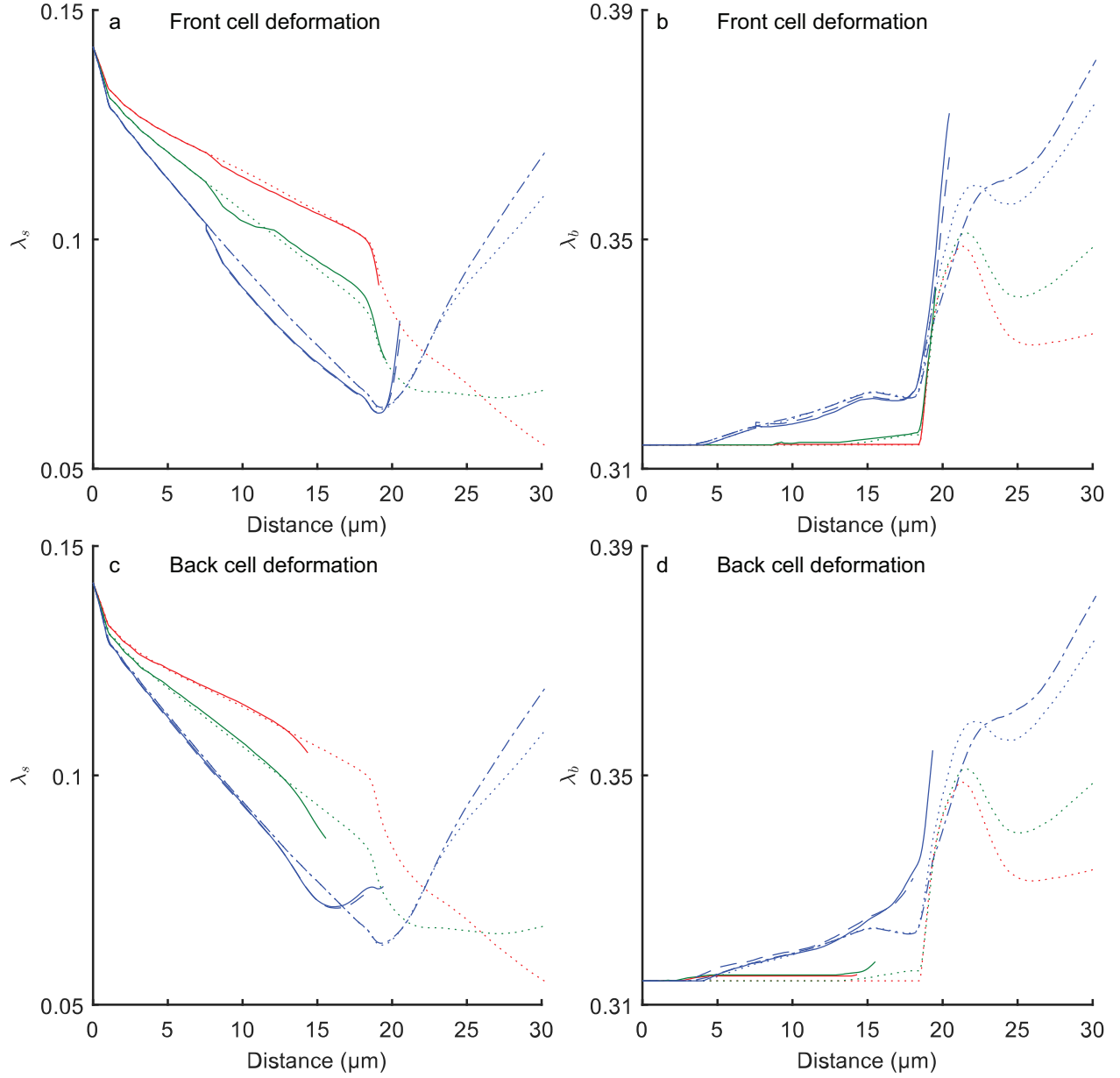
Figure 4.4. The average effects of an RBC traveling through a microvessel bifurcation on mean linear strain, λ_s, and mean bending, λ_b, for $\Psi_1 = 0.375$. Cells from simulations with hydraulic resistivity in the ESL of 10^6, 10^7, and 10^8 dyn·s/cm^4 are pictured in red, green, and blue, respectively. Single and two cell simulations are shown for $\Delta\pi_p = 200$ dyn/cm^2 (dotted, solid) and $\Delta\pi_p = 20$ dyn/cm^2 (dash-dotted, dashed). **(a)**, **(b)** Deformation of front cells. **(c)**, **(d)** Deformation of back cells.
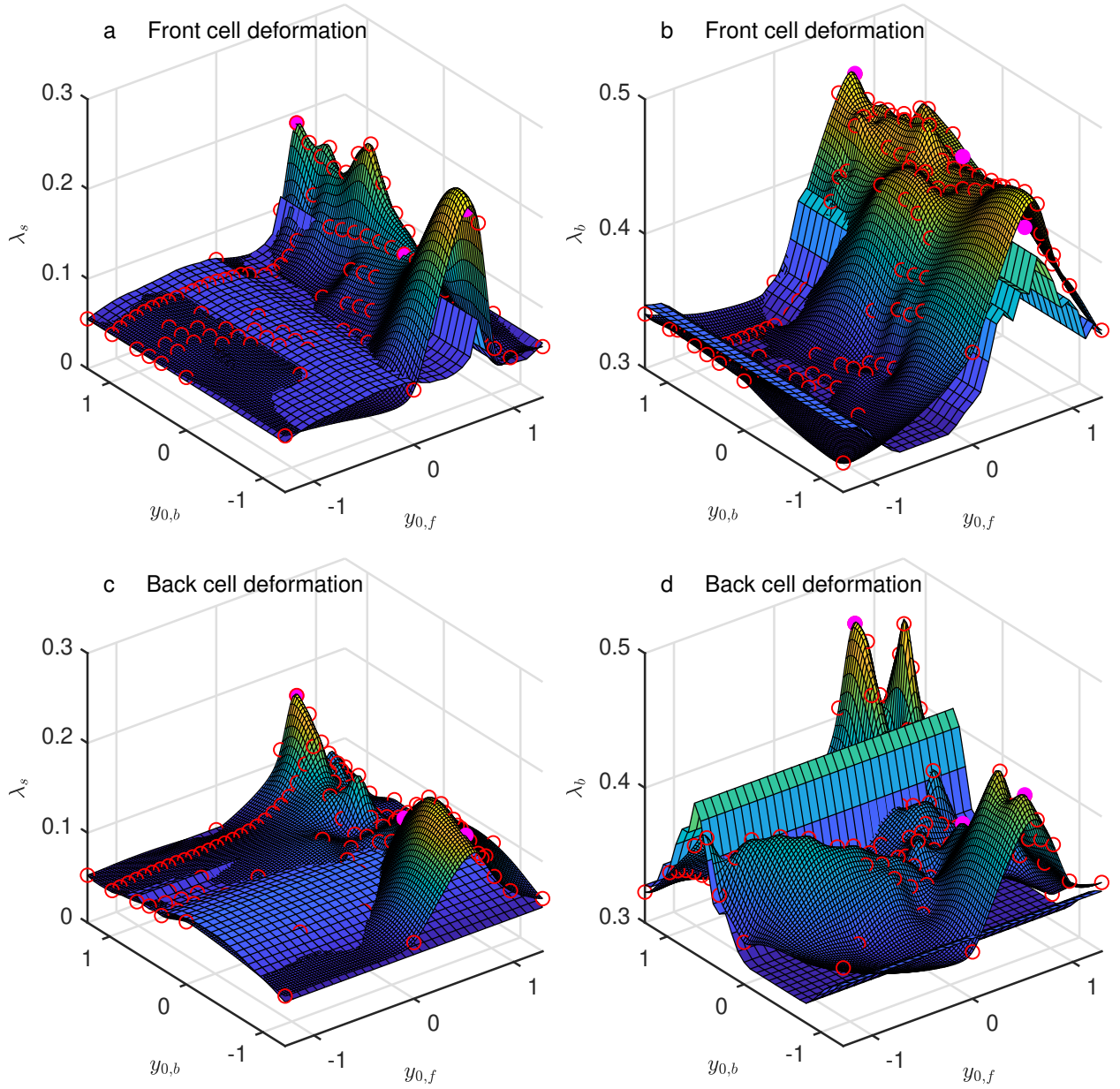
Figure 4.5. RBC shape deformation, λ_s and λ_b, over all possible initial cell center locations for $\Psi_1 = 0.375$, $\Delta\pi_p = 200$ dyn/cm^2, $\kappa = 10^8$ dyn·s/cm^4, and $\Delta d_0 = 7.5$ µm. The red circles on the two cell surfaces represent actual simulated data points. The three filled pink circles in each panel represent the points shown in Figures 4.6 and 4.7. Single cell surfaces are included in each plot for comparison. **(a)**, **(b)** Deformation of front cells. **(c)**, **(d)** Deformation of back cells.

Again, comparing single cell simulations to two cell simulations after 20.3 µm, λ_s increased from 0.112 to 0.134 (20%) and λ_b increased from 0.422 to 0.438 (4%), much less than the first example. Finally, in Figure 4.6c, the cells were initialized at $(y_{0,f}, y_{0,b}) = (0.645, -1.129)$. From single to two cell simulations, λ_s increased from 0.112 to 0.227 (103%) and λ_b increased from 0.422 to 0.465 (10%), in between the magnitude of change of the first two examples.

Figure 4.7 illustrates the same three data points as Figure 4.6, but compares back cell shapes with an isolated cell for the same set of distances traveled. In Figure 4.7a, after both cells had traveled 19.2 µm, λ_s and λ_b increased by 221% (0.052 to 0.167) and by 42% (0.328 to 0.465), respectively. In Figure 4.7a, λ_s and λ_b increased 64% (0.075 to 0.123) and 20% (0.314 to 0.378), respectively. And in Figure 4.7a, λ_s and λ_b increased 163% (0.056 to 0.147) and 27% (0.338 to 0.428), respectively. Each of these percentage increases is greater than the corresponding increases for the front cell. Also, the peak deformation levels for the back and front cells do not occur in the same locations on the $y_{0,f} - y_{0,b}$ plane as the peak levels for a single cell.

Also considered is the effect of hydraulic resistivity and osmotic pressure difference in the ESL on how deeply an RBC penetrates into the ESL region. Figure 4.8a shows the maximum penetration distance into the ESL region as a function of the initial y-value of the cell center for a flow split of $\Psi_1 = 0.375$ and a distance interval of $\Delta d_0 = 7.5$ µm between cells. Here, the initial cell center location of the back cell is fixed at $(x_{0,b}, y_{0,b}) = (-15, 0.968)$. This value was chosen because the peak penetration value of the three-dimensional plot on the $y_{0,f} - y_{0,b}$ plane lies on the $y_{0,b} = 0.968$ level surface. Zero penetration, marked on the plot with a dashed black line, corresponds to the center of the diffuse boundary of the ESL region. For two cell simulations, denoted with a solid curve for a high osmotic pressure of $\Delta \pi_p = 200$ dyn/cm^2 and a dashed curve for a low osmotic pressure of $\Delta \pi_p = 20$ dyn/cm^2, only the distance the front cell penetrates into the ESL region is considered. Again, red, green, and blue curves correspond to low, medium, and high hydraulic resistivity in the ESL. For comparison, a single cell simulation is included for high hydraulic resistivity at a high osmotic pressure difference and is denoted with a dotted curve. The square symbols on the curves indicate the simulations plotted in Figures 4.8b and c at initial cell center y-values of 0.564 and 0.968, respectively. These plots show the penetration distance into the ESL
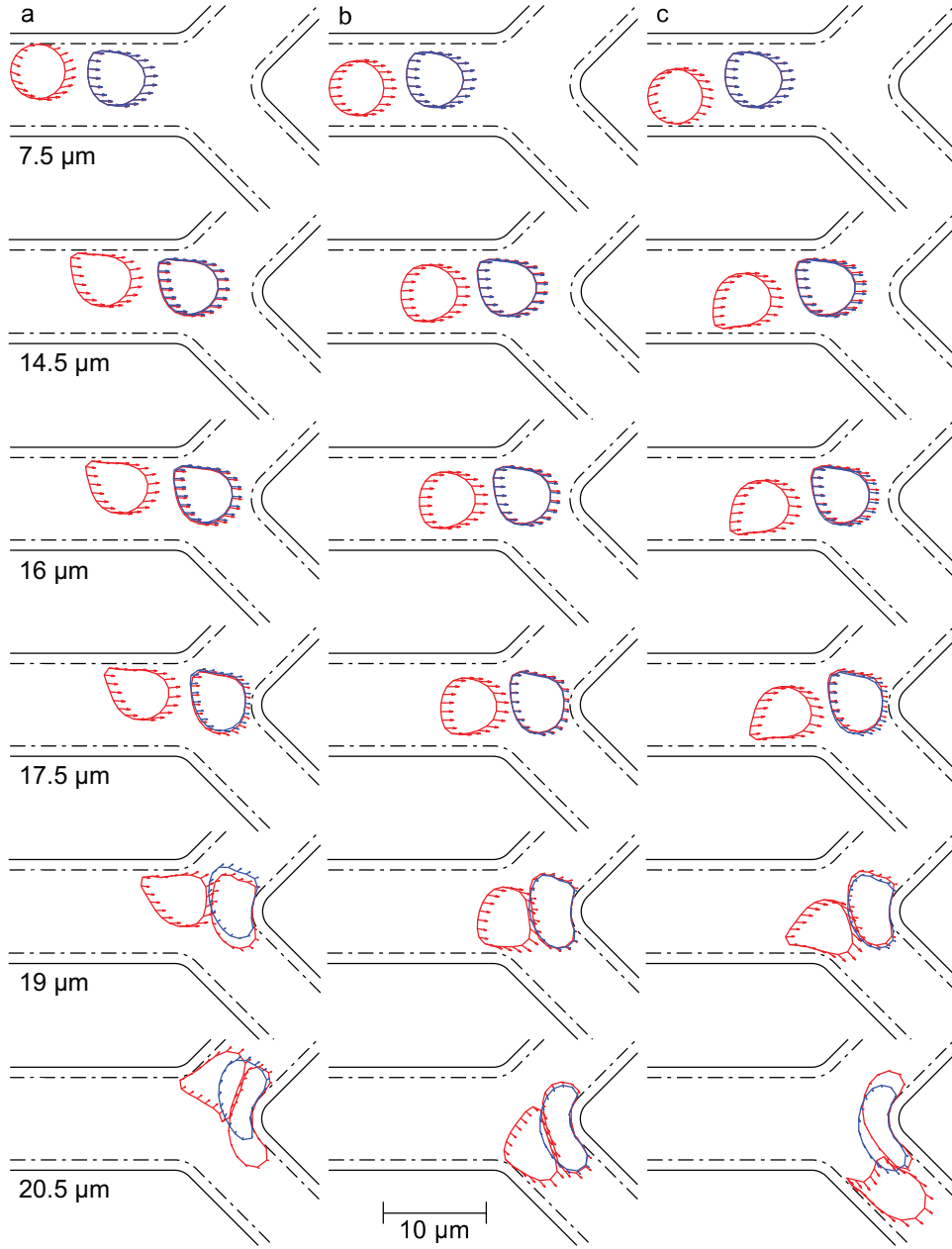
Figure 4.6. The effects of RBC interactions on front cell shape deformation for $\Psi_1 = 0.375$, $\Delta\pi_p = 200$ dyn/cm^2, $\kappa = 10^8$ dyn·s/cm^4, and $\Delta d_0 = 7.5$ µm. Blue and red cells represent single and two cell simulations, respectively. In each snapshot, the distances listed on the figure correspond to the distance traveled since the initialization in the mother vessel of the front or single cell. **(a)** Cells initialized at $(y_{0,f}, y_{0,b}) = (0.806, 1.29)$. **(b)** Cells initialized at $(y_{0,f}, y_{0,b}) = (0.645, -0.323)$. **(c)** Cells initialized at $(y_{0,f}, y_{0,b}) = (0.645, -1.129)$.
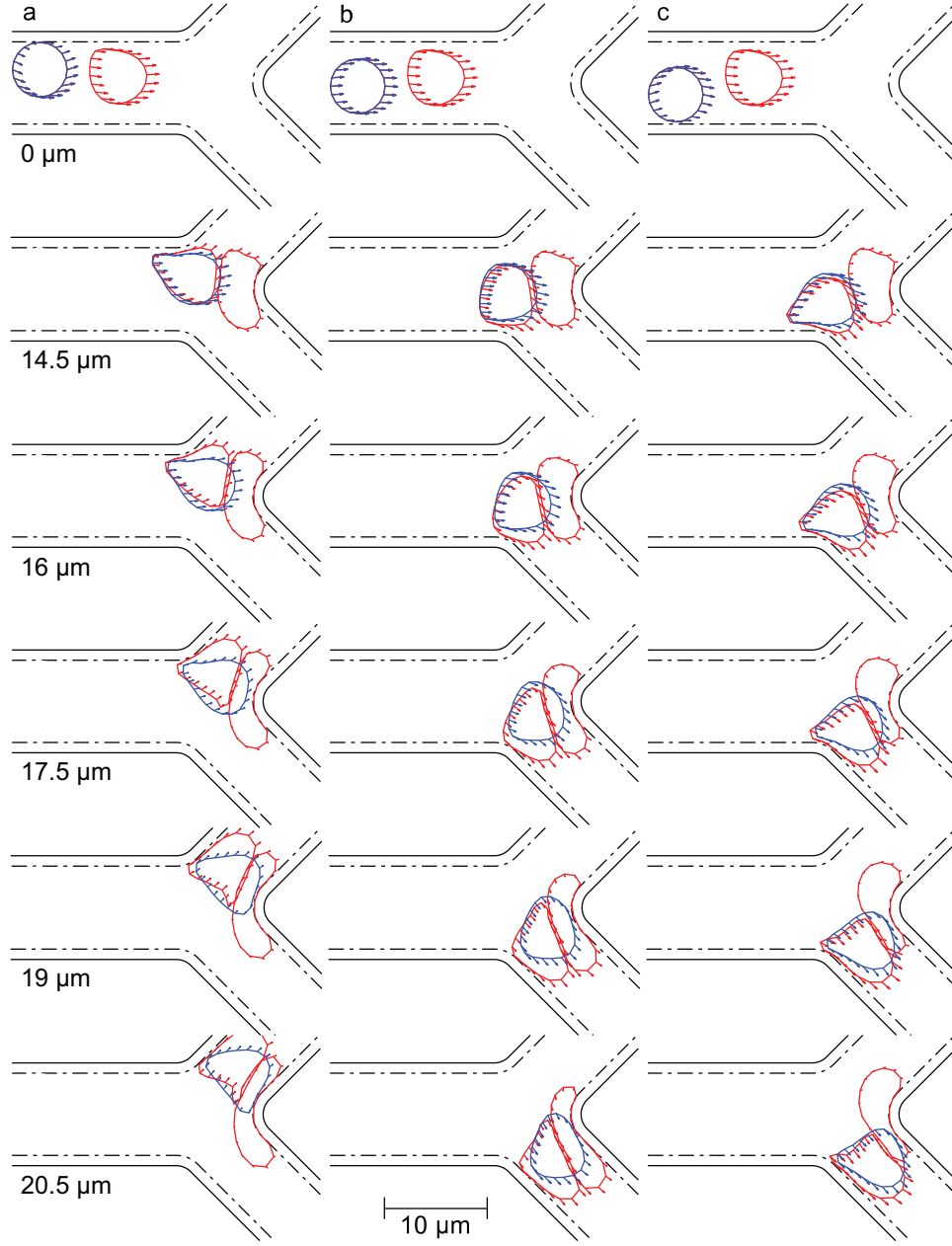
Figure 4.7. The effects of RBC interactions on back cell shape deformation for $\Psi_1 = 0.375$, $\Delta\pi_p = 200$ dyn/cm^2, $\kappa = 10^8$ dyn·s/cm^4, and $\Delta d_0 = 7.5$ µm. Blue and red cells represent single and two cell simulations, respectively. In each snapshot, the distances listed on the figure correspond to the distance traveled since the initialization in the mother vessel of the back or single cell. **(a)** Cells initialized at $(y_{0,f}, y_{0,b}) = (0.806, 1.29)$. **(b)** Cells initialized at $(y_{0,f}, y_{0,b}) = (0.645, -0.323)$. **(c)** Cells initialized at $(y_{0,f}, y_{0,b}) = (0.645, -1.129)$.

region over distance traveled by the front or single cell. The square symbols on the curves in these plots indicate the peak penetration distances achieved for each simulation. The black circular symbols on the curves representing single and two cell simulations for high hydraulic resistivity at a high osmotic pressure difference correspond to the snapshot taken in Figure 4.9. The addition of cell-cell interactions produces an increased penetrative effect. However, for paired front cells, penetration does not have a clear trend for varying hydraulic resistivity in the ESL for RBCs that penetrate past the median of the diffuse ESL boundary (dashed black line). However, decreased osmotic pressure difference has a clear correlation to increased penetration distance.

Figure 4.9a shows a snapshot of the simulations indicated with black circular symbols on Figure 4.8 at 21 µm of distance traveled by the single or front cell. The single and two cell simulations are shown in blue and red, respectively. Figure 4.9b magnifies the region of Figure 4.9a in the grey box. This example clearly shows the increased RBC penetration into the ESL when an additional cell is present and interacting with the original cell and is typical of the penetration behavior seen in other simulations with significant penetration of the ESL.

4.4 Discussion

Numerical simulations produced three types of effects that can alter partitioning behavior when ESL properties are varied and thus, theoretically, downstream hematocrit.

The blockage effect occurs when an increase in hydraulic resistivity in the ESL causes the front cell to block the entry of the back cell into a given branch and causes it to enter the opposite branch. In this case the interaction between cells is relatively large as cells can layer on top of each other, as seen in Figure 4.1a. In this scenario, the majority of the front cell area is entering the high flow branch, yet a significant portion is also entering the low flow branch. This results in an RBC with a shape identified by two relatively large bulbous regions entering separate daughter branches with a more narrow connecting region between them. Increasing the hydraulic resistivity enhances the obstruction effect and encourages the lead cell to enter the low flow branch. To balance flow conservation, when the lead cell moves

94
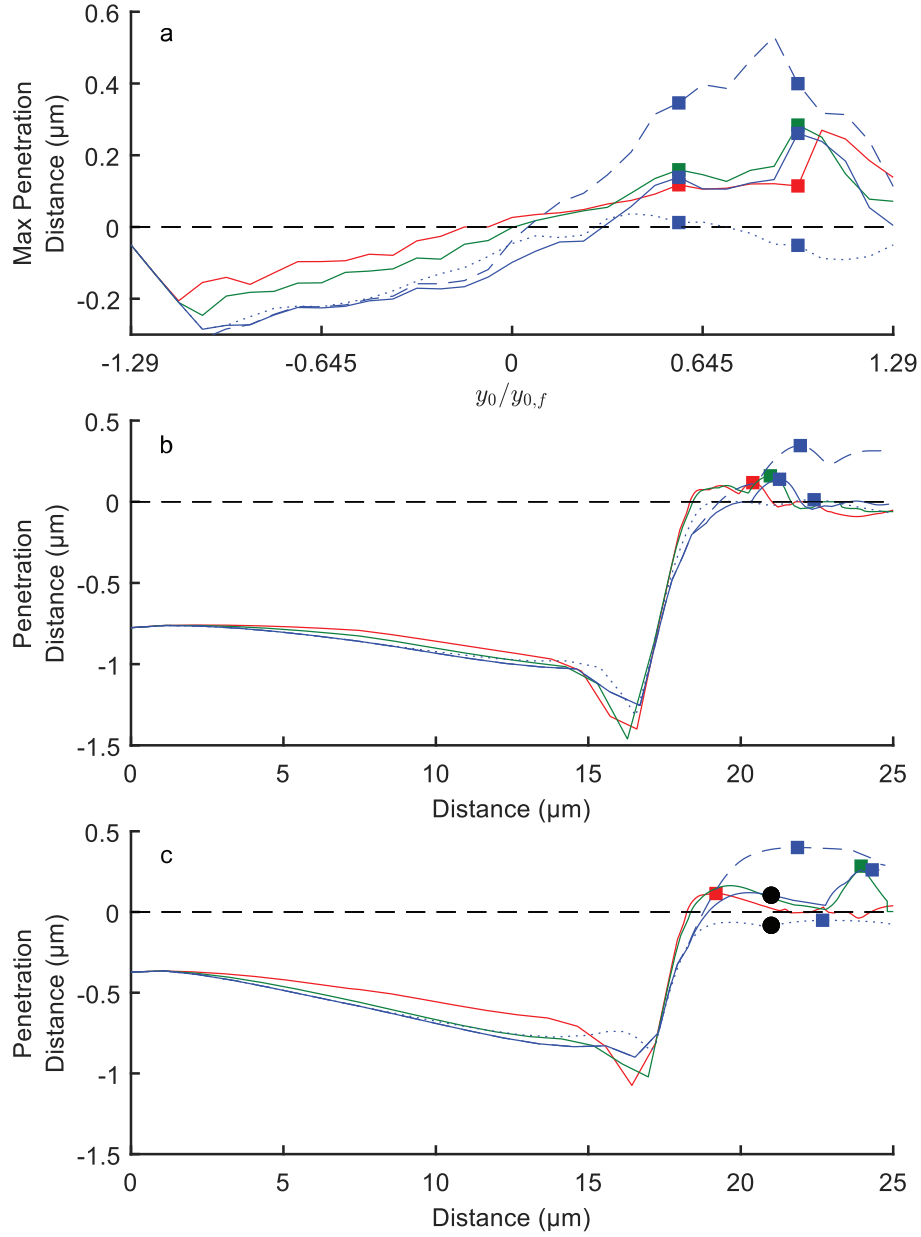
Figure 4.8. The effects of hydraulic resistivity and osmotic pressure difference in the ESL on front cell penetration into the ESL for $\Psi_1 = 0.375$ and $\Delta d_0 = 7.5$ µm. Cells from simulations with hydraulic resistivity in the ESL of 10^6, 10^7, and 10^8 dyn·s/cm^4 are pictured in red, green, and blue, respectively. Single and two cell simulations are shown for $\Delta \pi_p = 200$ dyn/cm^2 (dotted, solid) and two cell simulations are shown for $\Delta \pi_p = 20$ dyn/cm^2 (dashed). **(a)** Maximum penetration distance plotted over $y_0/y_{0,f}$. **(b)**, **(c)** Penetration distance plotted over distance traveled. Square symbols indicate peak values corresponding to $y_0/y_{0,f}$ in **(a)**. Circular symbols correspond to snapshot taken in Figure 4.9.
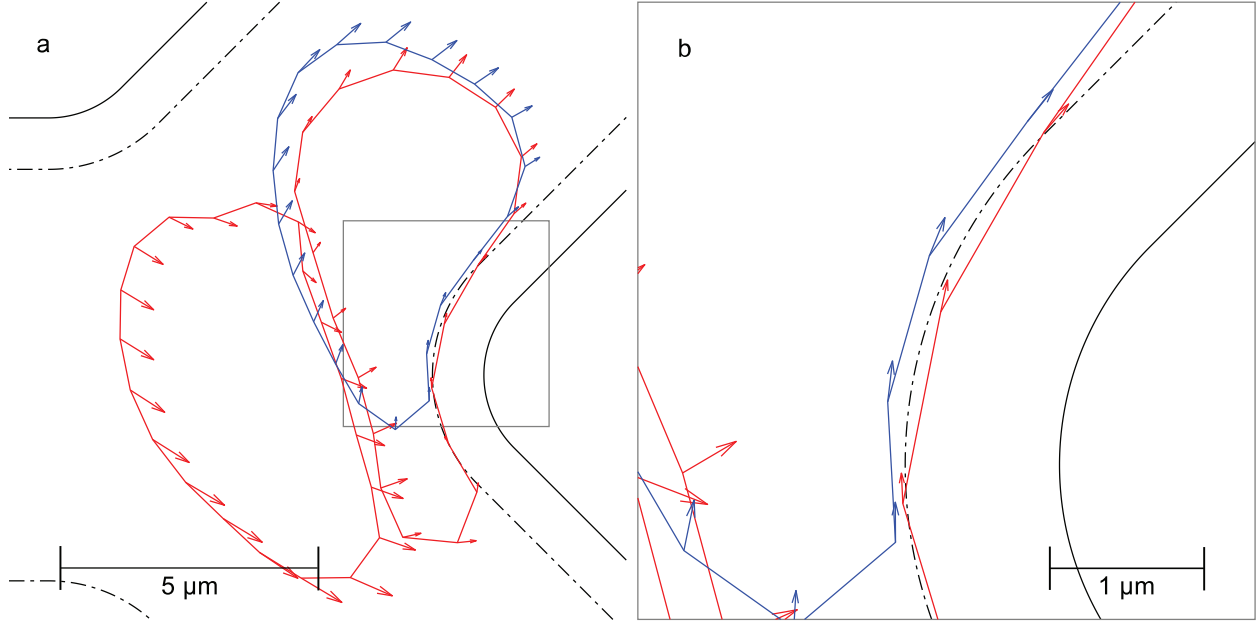
Figure 4.9. The effect of RBC interactions on RBC penetration into the ESL region for $\Psi_1 = 0.375$, $\Delta\pi_p = 200$ dyn/cm^2, $\kappa = 10^8$ dyn·s/cm^4, and $\Delta d_0 = 7.5$ µm. Blue and red cells represent single and two cell simulations, respectively. Cell centers were initialized at y-values of $y_0 = y_{0,f} = y_{0,b} = 0.968$. **(a)** Snapshot at 21 µm of distance traveled by the single and front cells. Arrows correspond to nodal velocities. **(b)** Magnification of the region enclosed in the grey box from **(a)**.

towards the low flow branch, the back cell moves towards the high flow branch. Whether or not the front cell eventually enters the low flow branch entirely is immaterial in defining this blockage effect as the trajectory of the back cell has already been sufficiently altered by this effect produced by the front cell (akin to the mechanism behind trade-off interactions) to alter its partitioning behavior. As seen in the figure, the blockage effect encourages more cells to enter the same high flow branch as hydraulic resistivity is raised, which corresponds to more nonuniform partitioning. The high flow branch in general claims most of the RBCs and now claims even more.

The obstruction effect, referring to a two cell effect in this discussion, occurs when the partitioning behavior of a cell is altered by being drawn into the low flow branch whereas the same cell for lower hydraulic resistivity in the ESL would have entered the high flow branch. This often occurs with only relatively long-distance interactions between cells. An

example of this interaction is illustrated in Figure 4.1b. In this scenario, the locations and velocities of each cell node comprising the back cell membrane are not significantly impacted by the difference in hydraulic resistivity in the ESL between the two cases until the back cell is impeded by the ESL at the bifurcation at 19 µm of distance traveled. As seen in Chapter 3, raising the hydraulic resistivity sends more flow through the centers of the vessels causing and enhancing the obstruction effect in general. This in turn causes the trajectory of the back cell to diverge towards the low flow, or upper branch. This is opposed to what happens in the lower hydraulic resistivity case where the obstruction effect is not strong enough to pull in the back cell and the back cell instead enters the high flow, or lower branch. As seen in the figure, raising the hydraulic resistivity causes the cells to go into separate branches, which corresponds to more uniform partitioning.

The pseudo herding effect occurs when the partitioning behavior of a front cell is affected through an interaction with the back cell facilitated by an increase in hydraulic resistivity in the ESL. In these scenarios, higher hydraulic resistivity in the ESL produces more elongated front cells as they negotiate the bifurcation. An example of this can be seen in Figure 4.1c. In this example, this elongated shape of the front cell allows the back cell to interact with a larger portion of the membrane of the front cell. In addition, increased hydraulic resistivity makes it so that flow can only enter the high flow branch through the non-ESL portion of the high flow vessel. This creates a flow blockage that further encourages both cells to enter the bottom branch. Both of these factors enable the back cell to pull the front cell into the lower branch. Lower hydraulic resistivities do not elongate cells as much and allow flow to go around cells blocking the high flow branch by traveling through the ESL. This enables the back cell to pass by without sufficient interaction to pull the front cell into the lower branch. As seen in the figure, raising the hydraulic resistivity causes more cells to enter the same high flow branch, which generally corresponds to more nonuniform partitioning.

These three effects are the driving forces behind changes in partitioning behavior that result when hydraulic resistivity is varied. Such changes can be seen in Figure 4.3. There, at a distance interval of $\Delta d_0 = 7.5$ µm between cells, increased hydraulic resistivity in the ESL leads to more nonuniform partitioning behavior for back cells. In contrast, the points at $\Delta d_0 = 10$ µm shows that the trend begins to break down. Looking at 4.2 shows a similar

97

trend breakdown as distance is increased. There higher resistivities seem to correspond to a greater departure from single cell dynamics for back cells when $\Delta d_0 = 7.5$ µm. At $\Delta d_0 = 10$ µm, however, there is no obvious trend regarding the curves' distances from the single cell y_c dashed line. To explain the diminished trend, an additional boundary condition related effect must be discussed.

Recall that constant boundary conditions for flux are prescribed for the inlet and outlet flows of the bifurcation system (see section 2.1.2 for more details). A result of these conditions is that increased hydraulic resistivity in the ESL leads to more flow resistance in the layer and a higher fluid flow rate near the vessel center to compensate. Two competing mechanisms arise from these changes. First, cells tend to travel more quickly near the center of the vessels for comparatively higher hydraulic resistivity scenarios. If the front cell is held up at the bifurcation, the back cell takes less time to reach that front cell when the hydraulic resistivity is higher. This means that in scenarios with higher hydraulic resistivities, interactions will take place more quickly and strongly. Second, cells tend not to sink into the ESL as deeply for comparatively higher hydraulic resistivity scenarios and are able to traverse the bifurcation more quickly as a result. This means that in scenarios with higher hydraulic resistivities, interactions take place more slowly and weakly. Overall, the second of these mechanisms is the more dominant, leading to weaker interactions and partitioning behavior more similar to that of isolated cells. These spacing effects, however, are minimal for small Δd_0 values.

It should be noted that the blockage, obstruction, and pseudo herding effects are observed regardless of whether low or high osmotic pressure differences are used in the ESL. Simulations were run for both osmotic pressure difference values and produced near identical results in terms of partitioning behavior.

The partitioning behavior for the various cases can be seen in Figure 4.3. Initially, for low initial distance between cells and as cell-cell interaction effects gain prominence, higher hydraulic resistivity correlates with a greater fraction of cells entering the upper daughter branch. As the initial distance between cells increases, the cell-cell interaction effects are diminished, and the spacing effects described above lead to a reversal: now low hydraulic resistivity correlates with a greater fraction of cells enter the upper branch. As the initial distance between cells increases even further, to approximately $\Delta t_0 = 10$ ms for front cells

and $\Delta t_0 = 15$ ms for back cells, partitioning behavior erodes to levels approaching those of isolated cells. In the case of low hydraulic resistivity in the ESL of $\kappa = 10^6$ dyn·s/cm^4, the relatively slower speed of the cells near the mother vessel center prolongs the interval of Δt_0 in which cell-cell interactions occur, briefly making it so that back cell partitioning goes below the levels for isolated cells.

Integrated over the full Δt_0 interval where paired RBC interactions occur, the fraction of RBCs entering the low flow branch varies less than 2% across the levels of hydraulic resistivity in the ESL studied, as listed in Table 4.1. However, as hematocrit increases and the distances between flowing RBCs decreases, it is likely that the effects on cell interactions discussed above will have an increasing effect on overall partitioning.

Also considered is the effect of hydraulic resistivity and osmotic pressure in the ESL on cell shape deformations. Mean linear strain is initially elevated in the cell membrane, and mean bending angle is reduced, due to how the cells are initialized in the fluid in a compressed circular state, as described in section 3.2. As the cells travel along the mother vessel, the strain decreases and bending increases as the cell shapes develop towards steady state configurations. These changes are more pronounced for higher hydraulic resistivity in the ESL due to the comparatively higher shear rate near the ESL which promotes deformation.

Figure 4.4 shows the average behavior of these metrics over distance traveled by both front and back cells in two cell simulations as well as for isolated cells. Low, medium, and high hydraulic resistivities and low and high osmotic pressure differences in the ESL are considered. The front cell experiences a sharp increase in strain upon interaction with the ESL at the bifurcation. On average, this increase is greater than that of an isolated cell for the same ESL parameters due to the further impact of the back cell, sandwiching the front cell between itself and the vessel bifurcation. The back cell experiences a similar increase, but less sharply due to the cushioning effect the front cell provides. Comparing isolated cells, high hydraulic resistivity in the ESL compresses the cell more as the RBC slides through the bifurcation into a daughter branch, while lower hydraulic resistivities compress the cell less in the same region. In fact, for a low hydraulic resistivity of $\kappa = 10^6$ dyn·s/cm^4 in the ESL, no increase in strain is seen, on average, at any point while traversing the bifurcation.

The front cell also experiences a sharp increase in bending upon interaction with the ESL at the bifurcation. On average, this increase is greater than that of an isolated cell for the same ESL parameters due to the further impact of the back cell. A similar, though less sharp, increase is seen in the back cell due to the cushioning effect provided by the front cell. Comparing isolated cells, high hydraulic resistivity in the ESL bends the cell more as the RBC slides through the bifurcation into a daughter branch, while lower hydraulic resistivities bend the cell less in the same region. After the initial impact with the bifurcation, bending decreases before increasing again as shear effects from the daughter branch wall deform the RBC.

Given these observations from the data, it is reasonable to predict that for paired cell deformations, the strain and bending in the front cell will be higher than the corresponding isolated cell cases due to the additional force exerted upon it by the back cell, but also decreasing in magnitude for decreasing levels of hydraulic resistivity in the ESL. The differences in deformation produced by a lower magnitude of osmotic pressure difference in the ESL would theoretically also decrease the magnitude of strain and bending due to the increased compressibility of the layer. However, simulations for a low osmotic pressure difference in the ESL were not able to run for long enough to confirm this hypothesis absolutely, though slight decreases were observed.

Deformation in front cells tend to be greatest for cells whose initial cell center locations are near the separating curve for front cells, Γ_f. There, cells take the longest time to negotiate the bifurcation, which also extends their interaction time with the back cells. This can be seen in Figures 4.5a and b. The same effects for back cells are also strongly impacted by Γ_f, indicating that close contact with the front cell is the primary cause of deformation for back cells. This can be seen in Figures 4.5c and d.

The typical deformation differences between single and paired cells are shown in the examples plotted in Figures 4.6 for front cells and 4.7 for back cells. These plots illustrate three points taken near Γ_f from Figure 4.5, plotted there as filled pink circles. An increase in deformation, in this context, refers to the comparative increase between isolated and paired cells at 20.3 µm for front cells and 19.2 µm for back cells, the maximum distance traveled by the cells in all simulations involved. The first point shows an example of a sharp increase in

100

deformation due to a direct impact between the cells and the vessel wall at the bifurcation. The second shows an example of a very small increase in deformation. This is due to the fact that the cells have enough room to traverse the bifurcation without influencing the shape of the other cell, especially in the case of the front cell. Finally, the third example shows a sharp increase in deformation due to a herding type effect as the back cell first pushes the front cell towards the opposite daughter branch but then pulls the front cell through the same branch it enters. While partitioning of the front cell was not ultimately affected, the deformation of the cell was.

Finally, how deeply an RBC penetrates into the ESL region is considered. Comparing isolated cell penetration to the penetration of the front cell in a paired cell simulation, we can see from the plotted data in Figure 4.8a for high hydraulic resistivity in the ESL that for the range of initial cell center locations that lead to significant RBC interactions, the front cell penetrates into the ESL region significantly deeper. The example illustrated in Figure 4.9 shows how a strong interaction with the back cell forces the front cell deeper into the ESL region. However, when RBC interactions are minimal, the isolated cell travels nearer to the vessel wall due to the absence of a back cell which would prevent fluid flow from pushing the front cell as strongly towards the ESL region. When comparing paired cell simulations at low and high osmotic pressure differences in the ESL, we see the most significant increase in penetration distance, especially in the aforementioned range of initial cell center locations that lead to more significant RBC interactions.

Comparisons between varying levels of hydraulic resistivity in the ESL for paired cell simulations prove to be more complex than those seen between isolated cell simulations in Figure 3.6. The trend in isolated cells that lower hydraulic resistivity leads to a greater penetration distance is true in the physiological range comparing $\kappa = 10^8$ to 10^7 dyn·s/cm^4 for paired cells. However, a pathologically low level of hydraulic resistivity in the ESL of $\kappa = 10^6$ dyn·s/cm^4 leads to lower penetration distances for a range of $y_{0,f}$ values corresponding to stronger RBC interactions.

There are three key factors leading to this result. First is the impact of the discretized membrane. The discretized cell membrane used in simulations may produce membrane segments oriented perpendicular to the ESL region that may be pushed into the layer. This

101

may lead to physiologically unrealistic scenarios of cell corners penetrating deeply into the ESL region. An example of this may be seen in Figure 4.8c in the second, higher peaks in the curves representing medium and high hydraulic resistivity for paired cell simulations. However, even when ignoring these second, possibly unrealistic peaks, the low hydraulic resistivity case still does not penetrate the ESL region as deeply as cases of comparatively higher hydraulic resistivity.

This leads to the second factor, the impact of centerline fluid flow rates. As previously discussed, for lower hydraulic resistivity in the ESL, the fluid flow rate near the vessel center is comparatively low. This leads to a more gradual impact of the back cell into the front cell, producing a lower penetration distance into the ESL. Finally, the third factor is related to the second. The lower centerline fluid flow rate makes it so that it takes longer for back cells to catch up to front cells impeded by the bifurcation. This allows the front cell to absorb the impact of itself into the ESL at the bifurcation before feeling the additional impact of the back cell. These last two factors help explain why lower hydraulic resistivity in the ESL actually leads to lower maximum penetration into the ESL region when there is significant RBC interaction.

Partitioning of hematocrit at microvessel bifurcations depends strongly on the upstream hematocrit distribution. However, in this study, the distribution of upstream RBCs was assumed to be uniform. *In vivo*, upstream hematocrit is determined by a number of factors including cell migration towards the vessel centerline, cell-cell and cell-wall interactions, cell deformation, vessel history (such as any upstream bifurcations encountered), and the length of the upstream vessels. For any given upstream hematocrit distribution, p_1, the partitioning function $\Phi_{1,2}(\Psi_1)$ may be recalculated using the equations in section 4.2. Also, the arrival times and spacing of RBCs are assumed to be uniform and independently distributed. This is not generally the case. RBCs traveling in capillaries tend to form clusters due to variations in size, shape, and deformability [62] (nonuniform), and RBCs cannot overlap (nonindependent). There are also other limitations such as the use of a two-dimensional model and a set geometry (see Chapter 5 for more details).

In summary, the inclusion of cell-cell interactions in the model produces additional ESL-mediated effects that influence the partitioning, deformation and ESL penetration of RBCs.

Increased hydraulic resistivity in the ESL leads to three key effects that influence partitioning behavior. The blockage and pseudo herding effects promote more uniform partitioning, while the obstruction effect promotes more nonuniform partitioning. For closer spacing between cells, these interactions lead to more uniform partitioning, while farther spacing leads to the opposite. Cell-cell interactions also enhance deformation, especially through a sandwiching effect between front and back cells at bifurcations which is increased for high hydraulic resistivity in the ESL. And while decreased osmotic pressure difference in the ESL leads to significantly higher penetration by RBCs, decreased hydraulic resistivity produces less intense cell-cell interactions due to lower flow centralization which, in general, has the opposite effect.

5. CONCLUSIONS

When vessel diameters become comparable to those of red blood cells (RBCs) in the microvasculature, the endothelial surface layer (ESL) has been seen to play a significant role in blood flow dynamics in microvessel bifurcations [43]. To better understand the significance and scope of the ESL region on blood flow dynamics in the particular context of diverging microvessel bifurcations, it is important to consider the ESL's interaction with individual RBCs and its impact on cell-cell interactions. To do this, we focused on two particular ESL properties that have been shown to significantly affect general flow dynamics [3], [29]. These are the hydraulic resistivity in the ESL and the osmotic pressure difference between the ESL region and the region of free flowing plasma. These parameters were explored across a range of values corresponding to physiologically realistic scenarios for both healthy and pathological vessels. Experimental studies have been performed to measure the structure of the ESL region and its role in increasing flow resistance in the capillaries [20], [25]. However, the mechanical effects between RBCs and the ESL that influence cell partitioning, deformation, and penetration into the ESL layer are not fully understood. These three aspects of RBC behavior have important implications for the distribution of oxygen, the release of ATP, the adhesion of RBCs to vessel walls, and other biological processes (see Chapter 1 for more details). The model described in this dissertation has been used to better understand the mechanics underlying these aspects of RBC behavior and by extension, the biological processes that rely on them.

In regards to the effect of the ESL on RBC partitioning, simulations were run for isolated cells and paired cells. Very small differences were observed in partitioning for isolated cells, though small trends were identified. In general, lower hydraulic resistivity and lower osmotic pressure difference in the ESL produced more nonuniform partitioning behavior in RBCs. This was observed to be due to the decreased obstruction of fluid flow produced by cells in the case of lower hydraulic resistivity, and due to increased penetration into the ESL region, which lowered the relative amount of obstruction of the downstream branches, in the case of lower osmotic pressure difference.

For paired cell simulations, however, more significant and complex changes in RBC partitioning were observed. Three types of effects that arise when hydraulic resistivity in the ESL is varied were observed to alter the distribution of hematocrit between the daughter branches at diverging microvessel bifurcations. The "blockage" effect occurs when increasing the hydraulic resistivity causes a front cell to more fully block a particular branch which forces the back cell to enter the unblocked branch instead of the other branch. The "obstruction" effect occurs when increasing the hydraulic resistivity enhances obstruction which causes a back cell to be pulled into the low, instead of the high, flow branch. The "pseudo herding" effect occurs when increasing the hydraulic resistivity causes the back cell to pull the front cell in such a way that it enters the same, instead of the opposite, branch. In this last effect, the higher hydraulic resistivity elongates the front cells more and effectively narrows the free flowing regions in the vessel both of which increase the effectiveness with which the back cell pulls on the front cell. These effects are primarily seen for cells that are in close proximity to one another when entering the bifurcation region and their net effect is to produce more uniform partitioning as hydraulic resistivity is increased. Little change in partitioning was observed for paired cell simulations when comparing relatively high and low levels of osmotic pressure difference in the ESL.

The ESL also has a significant effect on RBC deformations in microvessel bifurcations. Comparing simulations of isolated cells for different hydraulic resistivities and osmotic pressure differences showed that changing ESL properties could significantly alter the shapes of cells as they pass through the bifurcation. At high osmotic pressure difference, high hydraulic resistivity in the ESL produced more deformed shapes than low hydraulic resistivity, especially for cells that both enter the high flow branch. While small amounts of deformation take place upstream and downstream of the bifurcation, most deformation takes place when the cell is in the bifurcation region near or in the ESL. The more centralized flow profile in the higher hydraulic resistivity scenarios have higher flow rates in the free flowing regions that enhance deformation for cells near or in the ESL leading to more deformation in general. For osmotic pressure differences, the low osmotic pressure difference allows cells to penetrate the ESL more easily and keep their rounded/less deformed shape. The effect is stronger when the hydraulic resistivity is lower. This is because when the ESL allows fluid

to more readily flow through it, it is easier for the cell to displace that fluid out of the ESL and easier for the cell to sink in.

Mean strain and bending angle in cell membranes were also considered as measures of deformation. The addition of another RBC in simulations produced significant changes in these metrics. Compared to isolated cell simulations, levels of strain and bending in two cell simulations increased sharply, especially the front cell membranes in the case of high hydraulic resistivity in the ESL. This is initially due to the front cell, impeded at the bifurcation, being impacted by the back cell. However, the increase in deformation is maintained and even increased as both cells slide against each other and the ESL through the bifurcation region. Predictions for lower hydraulic resistivities were made based on isolated cell data and how it compared to the data produced for two cell simulations for high hydraulic resistivity in the ESL. Little difference in strain or bending was observed when comparing high and low osmotic pressure differences.

Also considered was the effect of hydraulic resistivity and osmotic pressure difference in the ESL on cell penetration into the ESL region for both isolated cell simulations and two cell simulations. For isolated cells, a clear and consistent increase in maximum penetration distance into the ESL region was observed when decreasing the hydraulic resistivity in the ESL. This increase was especially prominent when decreasing the osmotic pressure difference in the ESL. In fact, the penetration distances observed were large enough to suggest the possibility of cell adhesion to the vessel wall or interaction with deeper structures in the glycocalyx [7], [41]. In two cell simulations, this trend continued for front cells in the physiological range of hydraulic resistivities observed in the ESL. However, when interacting strongly with the back cell, a decrease in hydraulic resistivity led to a decrease in maximum penetration distance. This was due in part to the impact of centerline fluid flow rates. Due to constant flux in and out of the bifurcation domain, lower hydraulic resistivity in the ESL produces lower fluid flow rates near the center of the vessel. This leads to a more gradual impact of the back cell into the front cell, producing lower penetration distances, instead of the higher ones expected based on single cell simulations.

Two-dimensional models have inherent limitations when modeling three-dimensional systems. The cross-sectional size of an RBC is on the order of $(R_{cell}/R_{vessel})^{D-1}$, where D is the

dimension of the model. This means that the cells in this model occupy a smaller proportion of the vessel lumen than in reality, which leads to exaggerated obstruction and trade-off effects in the two-dimensional model. Also in this study, the same configuration of vessels have been used in every simulation. However, vessel diameter of the mother vessel and the ratio of daughter branch diameters are known to affect deformation [42] and partitioning [43] of RBCs. For very small vessels, shape deformation in RBCs spike as they are forced to squeeze through vessels whose diameters are smaller than the diameter of an RBC at rest. At ratios of daughter branch vessel diameters other than 1, isolated RBCs are more likely to travel down the branch with smaller diameter due to an increased obstruction effect. Limitations regarding assumptions made about upstream cell distributions are discussed in section 4.4.

As described in section 2.1.2, constant boundary conditions for flux are prescribed for the inlet and outlet flows of the bifurcation system. As a result, increased hydraulic resistivity in the ESL leads to more flow resistance in the layer and a higher fluid flow rate near the vessel center to compensate. Measures have been taken to ensure clear results including comparing cells at equal distances traveled versus time traveled in vessels. However, certain results for paired cell simulations are nonetheless affected by these boundary condition effects. For example, when increasing initial cell spacing from $\Delta d_0 = 7.5$ to 10 µm, a reversal of trends is seen in Figure 4.2.

REFERENCES

[1] G. W. Schmid-Schonbein, R. Skalak, S. Usami, and S. Chien, "Cell distribution in capillary networks," *Microvasc Res*, vol. 19, no. 1, pp. 18–44, 1980. DOI: 10.1016/0026-2862(80)90082-5.

[2] A. R. Pries and T. W. Secomb, "Microvascular blood viscosity in vivo and the endothelial surface layer," *Am J Physiol Heart Circ Physiol*, vol. 289, no. 6, H2657–64, 2005. DOI: 10.1152/ajpheart.00297.2005.

[3] T. W. Secomb, R. Hsu, and A. R. Pries, "Effect of the endothelial surface layer on transmission of fluid shear stress to endothelial cells," *Biorheology*, vol. 38, no. 2-3, pp. 143–50, 2001.

[4] W. Y. Yen, B. Cai, M. Zeng, J. M. Tarbell, and B. M. Fu, "Quantification of the endothelial surface glycocalyx on rat and mouse blood vessels," *Microvasc Res*, vol. 83, no. 3, pp. 337–46, 2012. DOI: 10.1016/j.mvr.2012.02.005.

[5] A. R. Pries, T. W. Secomb, H. Jacobs, M. Sperandio, K. Osterloh, and P. Gaehtgens, "Microvascular blood flow resistance: Role of endothelial surface layer," *Am J Physiol*, vol. 273, no. 5, H2272–9, 1997. DOI: 10.1152/ajpheart.1997.273.5.H2272.

[6] B. M. Fu and J. M. Tarbell, "Mechano-sensing and transduction by endothelial surface glycocalyx: Composition, structure, and function," *Wiley Interdiscip Rev Syst Biol Med*, vol. 5, no. 3, pp. 381–90, 2013. DOI: 10.1002/wsbm.1211.

[7] H. Vink, A. A. Constantinescu, and J. A. Spaan, "Oxidized lipoproteins degrade the endothelial surface layer : Implications for platelet-endothelial cell adhesion," *Circulation*, vol. 101, no. 13, pp. 1500–2, 2000. DOI: 10.1161/01.cir.101.13.1500.

[8] A. W. Mulivor and H. H. Lipowsky, "Role of glycocalyx in leukocyte-endothelial cell adhesion," *Am J Physiol Heart Circ Physiol*, vol. 283, no. 4, H1282–91, 2002. DOI: 10.1152/ajpheart.00117.2002.

[9] H. Oberleithner, M. Wälte, and K. Kusche-Vihrog, "Sodium renders endothelial cells sticky for red blood cells," *Frontiers in physiology*, vol. 6, p. 188, 2015. DOI: 10.3389/fphys.2015.00188.

[10] H. Kimura, R. D. Braun, E. T. Ong, R. Hsu, T. W. Secomb, D. Papahadjopoulos, K. Hong, and M. W. Dewhirst, "Fluctuations in red cell flux in tumor microvessels can lead to transient hypoxia and reoxygenation in tumor parenchyma," *Cancer Res*, vol. 56, no. 23, pp. 5522–8, 1996.

[11] E. Zhao, J. Barber, M. Burch, J. Unthank, and J. Arciero, "Modeling acute blood flow responses to a major arterial occlusion," *Microcirculation*, vol. 27, no. 4, e12610, 2020. DOI: 10.1111/micc.12610.

[12] T. N. Williams and S. L. Thein, "Sickle cell anemia and its phenotypes," *Annu Rev Genomics Hum Genet*, vol. 19, pp. 113–147, 2018. DOI: 10.1146/annurev-genom-083117-021320.

[13] D. A. Fedosov, B. Caswell, S. Suresh, and G. E. Karniadakis, "Quantifying the biophysical characteristics of plasmodium-falciparum-parasitized red blood cells in microcirculation," *Proc Natl Acad Sci U S A*, vol. 108, no. 1, pp. 35–9, 2011. DOI: 10.1073/pnas.1009492108.

[14] T. Secomb and A. Pries, "Blood viscosity in microvessels: Experiment and theory," *Comptes rendus. Physique*, vol. 14 6, pp. 470–478, 2013.

[15] J. O. Barber, J. P. Alberding, J. M. Restrepo, and T. W. Secomb, "Simulated two-dimensional red blood cell motion, deformation, and partitioning in microvessel bifurcations," *Annals of Biomedical Engineering*, vol. 36, no. 10, pp. 1690–1698, 2008. DOI: 10.1007/s10439-008-9546-4.

[16] A. Pries, K. Ley, M. Claassen, and P. Gaehtgens, "Red cell distribution at microvascular bifurcations," *Microvascular Research*, vol. 38, no. 1, pp. 81–101, 1989. DOI: https://doi.org/10.1016/0026-2862(89)90018-6.

[17] J. M. Squire, M. Chew, G. Nneji, C. Neal, J. Barry, and C. Michel, "Quasi-periodic substructure in the microvessel endothelial glycocalyx: A possible explanation for molecular filtering?" *Journal of Structural Biology*, vol. 136, no. 3, pp. 239–255, 2001. DOI: https://doi.org/10.1006/jsbi.2002.4441.

[18] J. Rostgaard and K. Qvortrup, "Electron microscopic demonstrations of filamentous molecular sieve plugs in capillary fenestrae," *Microvascular Research*, vol. 53, no. 1, pp. 1–13, 1997. DOI: https://doi.org/10.1006/mvre.1996.1987.

[19] F. E. Curry, K. P. Arkill, and C. C. Michel, "The functions of endothelial glycocalyx and their effects on patient outcomes during the perioperative period. a review of current methods to evaluate structure-function relations in the glycocalyx in both basic research and clinical settings," in *Perioperative Fluid Management*, E. Farag and A. Kurz, Eds. Springer International Publishing, 2016, pp. 75–116. DOI: 10.1007/978-3-319-39141-0_3.

[20] S. Weinbaum, J. M. Tarbell, and E. R. Damiano, "The structure and function of the endothelial glycocalyx layer," *Annual Review of Biomedical Engineering*, vol. 9, no. 1, pp. 121–167, 2007. DOI: 10.1146/annurev.bioeng.9.060906.151959.

[21] J. R. Levick, "Revision of the starling principle: New views of tissue fluid balance," *The Journal of Physiology*, vol. 557, no. 3, pp. 704–704, 2004. DOI: https://doi.org/10.1113/jphysiol.2004.066118.

[22] H. Vink and B. R. Duling, "Capillary endothelial surface layer selectively reduces plasma solute distribution volume," *Am J Physiol Heart Circ Physiol*, vol. 278, no. 1, H285–9, 2000. DOI: 10.1152/ajpheart.2000.278.1.H285.

[23] T. W. Secomb, R. Hsu, and A. R. Pries, "A model for red blood cell motion in glycocalyx-lined capillaries," *Am J Physiol*, vol. 274, no. 3, H1016–22, 1998. DOI: 10.1152/ajpheart.1998.274.3.H1016.

[24] H. Vink and B. R. Duling, "Identification of distinct luminal domains for macromolecules, erythrocytes, and leukocytes within mammalian capillaries," *Circ Res*, vol. 79, no. 3, pp. 581–9, 1996. DOI: 10.1161/01.res.79.3.581.

[25] T. W. Secomb, R. Hsu, and A. R. Pries, "Blood flow and red blood cell deformation in nonuniform capillaries: Effects of the endothelial surface layer," *Microcirculation*, vol. 9, no. 3, pp. 189–96, 2002. DOI: 10.1038/sj.mn.7800132.

[26] J. O. Barber, J. M. Restrepo, and T. W. Secomb, "Simulated red blood cell motion in microvessel bifurcations: Effects of cell-cell interactions on cell partitioning," *Cardiovasc Eng Technol*, vol. 2, no. 4, pp. 349–360, 2011. DOI: 10.1007/s13239-011-0064-4.

[27] P. Balogh and P. Bagchi, "Analysis of red blood cell partitioning at bifurcations in simulated microvascular networks," *Physics of Fluids*, vol. 30, no. 5, p. 051 902, 2018. DOI: 10.1063/1.5024783.

[28] E. Damiano, "The effect of the endothelial-cell glycocalyx on the motion of red blood cells through capillaries," *Microvascular Research*, vol. 55, no. 1, pp. 77–91, 1998. DOI: https://doi.org/10.1006/mvre.1997.2052.

[29] D. S. Hariprasad and T. W. Secomb, "Motion of red blood cells near microvessel walls: Effects of a porous wall layer," *J Fluid Mech*, vol. 705, pp. 195–212, 2012. DOI: 10.1017/jfm.2012.102.

[30] J. B. Freund, "Numerical simulation of flowing blood cells," *Annual review of fluid mechanics*, vol. 46, pp. 67–95, 2014.

[31] D. A. Fedosov, B. Caswell, and G. E. Karniadakis, "A multiscale red blood cell model with accurate mechanics, rheology, and dynamics," *Biophysical journal*, vol. 98, no. 10, pp. 2215–2225, 2010.

[32] C. Sun and L. L. Munn, "Lattice-boltzmann simulation of blood flow in digitized vessel networks," *Computers & Mathematics with Applications*, vol. 55, no. 7, pp. 1594–1600, 2008.

[33] T. G. Fai and C. H. Rycroft, "Lubricated immersed boundary method in two dimensions," *Journal of Computational Physics*, vol. 356, pp. 319–339, 2018.

[34] S. Zhao, Y. Yu, T.-W. Pan, and R. Glowinski, "A dlm/fd/ib method for simulating compound cell interacting with red blood cells in a microchannel.," *Chinese Annals of Mathematics*, vol. 39, no. 3, 2018.

[35] M. Bor-Kucukatay, R. B. Wenby, H. J. Meiselman, and O. K. Baskurt, "Effects of nitric oxide on red blood cell deformability," *American Journal of Physiology-Heart and Circulatory Physiology*, vol. 284, no. 5, H1577–H1584, 2003, PMID: 12521942. DOI: 10.1152/ajpheart.00665.2002.

[36] A. M. Forsyth, J. Wan, P. D. Owrutsky, M. Abkarian, and H. A. Stone, "Multiscale approach to link red blood cell dynamics, shear viscosity, and atp release," *Proceedings of the National Academy of Sciences*, vol. 108, no. 27, pp. 10 986–10 991, 2011. DOI: 10.1073/pnas.1101315108.

[37] A. M. Forsyth, S. Braunmuller, J. Wan, T. Franke, and H. A. Stone, "The effects of membrane cholesterol and simvastatin on red blood cell deformability and atp release," *Microvasc Res*, vol. 83, no. 3, pp. 347–51, 2012. DOI: 10.1016/j.mvr.2012.02.004.

[38] H. Zhang, Z. Shen, B. Hogan, A. I. Barakat, and C. Misbah, "Atp release by red blood cells under flow: Model and simulations," *Biophys J*, vol. 115, no. 11, pp. 2218–2229, 2018. DOI: 10.1016/j.bpj.2018.09.033.

[39] D. H. Lee, M. J. Dane, B. M. van den Berg, M. G. Boels, J. W. van Teeffelen, R. de Mutsert, M. den Heijer, F. R. Rosendaal, J. van der Vlag, A. J. van Zonneveld, H. Vink, T. J. Rabelink, and N. E. O. s. group, "Deeper penetration of erythrocytes into the endothelial glycocalyx is associated with impaired microvascular perfusion," *PLoS One*, vol. 9, no. 5, e96477, 2014. DOI: 10.1371/journal.pone.0096477.

[40] J. W. Weisel and R. I. Litvinov, "Red blood cells: The forgotten player in hemostasis and thrombosis," *J Thromb Haemost*, vol. 17, no. 2, pp. 271–282, 2019. DOI: 10.1111/jth.14360.

[41] H. Oberleithner, "Vascular endothelium leaves fingerprints on the surface of erythrocytes," *Pflugers Archiv : European journal of physiology*, vol. 465, 2013. DOI: 10.1007/s00424-013-1288-y.

[42] T. W. Secomb, B. Styp-Rekowska, and A. R. Pries, "Two-dimensional simulation of red blood cell deformation and lateral migration in microvessels," *Annals of Biomedical Engineering*, vol. 35, no. 5, pp. 755–765, 2007. DOI: 10.1007/s10439-007-9275-0.

[43] A. R. Pries, T. W. Secomb, P. Gaehtgens, and J. F. Gross, "Blood flow in microvascular networks. experiments and simulation.," *Circulation Research*, vol. 67, no. 4, pp. 826–834, 1990. DOI: 10.1161/01.RES.67.4.826.

[44] PDE Solutions Inc., *Flexpde*, version 7.17, Dec. 15, 2020. [Online]. Available: https://www.pdesolutions.com.

[45] H. C. Brinkman, "A calculation of the viscous force exerted by a flowing fluid on a dense swarm of particles," *Journal of Applied Sciences Research*, vol. A1, pp. 27–34, 1947.

[46] E. A. Evans and R. Skalak, "Mechanics and thermodynamics of biomembranes: Part 2," *CRC Crit Rev Bioeng*, vol. 3, no. 4, pp. 331–418, 1979.

[47] K. C. Jea and D. M. Young, "On the simplification of generalized conjugate-gradient methods for nonsymmetrizable linear systems," *Linear Algebra and its Applications*, vol. 52-53, pp. 399–417, 1983. DOI: https://doi.org/10.1016/0024-3795(83)80026-3.

[48] V. Heinrich, K. Ritchie, N. Mohandas, and E. Evans, "Elastic thickness compressibilty of the red cell membrane," *Biophys J*, vol. 81, no. 3, pp. 1452–63, 2001. DOI: 10.1016/s0006-3495(01)75800-6.

[49] J. Barber and L. Zhu, "Two-dimensional finite element model of breast cancer cell motion through a microfluidic channel," *Bulletin of Mathematical Biology*, pp. 1–22, 2019. DOI: 10.1007/s11538-018-00557-x.

[50] W. Chien, G. Gompper, and D. A. Fedosov, "Effect of cytosol viscosity on the flow behavior of red blood cell suspensions in microvessels," *Microcirculation*, vol. 28, no. 2, e12668, 2021. DOI: https://doi.org/10.1111/micc.12668.

[51] J. O. Barber, *Computational simulation of red blood cell motion in microvascular flows*, 2009. [Online]. Available: http://hdl.handle.net/10150/193887.

[52] T. W. Secomb, "Mechanics of red blood cells and blood flow in narrow tubes," in *Hydrodynamics of Capsules and Cells*, C. Pozrikidis, Ed. London: Chapman & Hall/CRC, 2003, pp. 163–196.

[53] H. N. Mayrovitz and J. Roy, "Microvascular blood flow: Evidence indicating a cubic dependence on arteriolar diameter," *Am J Physiol*, vol. 245, no. 6, H1031–8, 1983. DOI: 10.1152/ajpheart.1983.245.6.H1031.

[54] J. Arciero, L. Lembcke, M. Burch, E. Franko, and J. Unthank, "Assessing the hemo-dynamic contribution of capillaries, arterioles, and collateral arteries to vascular adap-tations in arterial insufficiency," *Microcirculation*, vol. 27, no. 2, e12591, 2020. DOI: https://doi.org/10.1111/micc.12591.

[55] E. R. Damiano, B. R. Duling, K. Ley, and T. C. Skalak, "Axisymmetric pressure-driven flow of rigid pellets through a cylindrical tube lined with a deformable porous wall layer," *Journal of Fluid Mechanics*, vol. 314, pp. 163–189, 1996. DOI: 10.1017/S0022112096000274.

[56] A. R. Pries, T. W. Secomb, T. Gessner, M. B. Sperandio, J. F. Gross, and P. Gaehtgens, "Resistance to blood flow in microvessels in vivo," *Circ Res*, vol. 75, no. 5, pp. 904–15, 1994. DOI: 10.1161/01.res.75.5.904.

[57] A. R. Pries, T. W. Secomb, M. Sperandio, and P. Gaehtgens, "Blood flow resistance during hemodilution: Effect of plasma composition," *Cardiovasc Res*, vol. 37, no. 1, pp. 225–35, 1998. DOI: 10.1016/s0008-6363(97)00226-5.

[58] A. R. Pries, T. W. Secomb, and P. Gaehtgens, "The endothelial surface layer," *Pflugers Arch*, vol. 440, no. 5, pp. 653–66, 2000. DOI: 10.1007/s004240000307.

[59] C. Pfafferott, G. B. Nash, and H. J. Meiselman, "Red blood cell deformation in shear flow. effects of internal and external phase viscosity and of in vivo aging," *Biophys J*, vol. 47, no. 5, pp. 695–704, 1985. DOI: 10.1016/S0006-3495(85)83966-7.

[60] R. Franke, "Scattered data interpolation: Tests of some method," *Mathematics of Com-putation*, vol. 38, no. 157, pp. 181–200, 1982.

[61] W. H. Press, S. A. Teukolsky, W. T. Vetterling, and B. P. Flannery, "Numerical recipes: The art of scientific computing," in, 3rd ed. Cambridge, England: Cambridge University Press, 2007.

[62] P. Gaehtgens, C. Dührssen, and K. H. Albrecht, "Motion, deformation, and interaction of blood cells and plasma during flow through narrow capillary tubes.," *Blood cells*, vol. 6, pp. 799–817, 1980.

VITA

EDUCATION

- **Ph.D. Candidate in Mathematics, Purdue University, West Lafayette, IN. 2015–2021.**

  Advisor: Dr. Jared Barber.

- **Master of Science in Mathematics, Indiana University - Purdue University (IUPUI), Indianapolis, IN. 2015–2017.**

- **Bachelor of Science in Mathematics, Olivet Nazarene University, Bourbonnais, IL. 2012–2014.**

  Summa Cum Laude. Minor in Chemistry.

- **Associate of Science in General Mathematics and Science, Prairie State College, Chicago Heights, IL. 2010–2012.**

  Summa Cum Laude.

WORK AND TEACHING EXPERIENCE

- **Mathematics Instructor, IUPUI, Indianapolis, IN. 2017–2020.**

  – Analytic Geometry and Calculus I, Spring 2020.

  – Trigonometry, Fall 2019.

  – Calculus for the Life Sciences II, Summer 2019.

  – Analytic Geometry and Calculus II, Spring 2019.

  – College Algebra, Fall 2018.

  – Calculus for the Life Sciences II, Summer 2018.

  – Intermediate Algebra, Spring 2018.

  – Intermediate Algebra, Fall 2017.

- **Mathematics Tutor, Mathematics Assistance Center at IUPUI, Indianapolis, IN. 2016–2019.**

Tutored a wide range of topics, including trigonometry, calculus, differential equations, and linear algebra.

- **Chemistry Lab Teacher's Assistant, Olivet Nazarene University, Bourbonnais, IL. 2013–2014.**
  Answered questions during lab and graded lab reports and quizzes.

PUBLICATIONS

- Triebold C, Barber J. *Dependence of red blood cell dynamics in microvessel bifurcations on the endothelial surface layer's resistance to flow and compression.* Submitted.

- Triebold C, Barber J. *Simulated red blood cell motion: The effect of the endothelial surface layer on cell-cell interactions in microvessel bifurcations.* In preparation.

PRESENTATIONS

- SIAM Annual Meeting, July 2021. *The effects of the endothelial surface layer on red blood cell dynamics in microvessel bifurcations.* Co-author Jared Barber.

- IUPUI Biomathematics Seminar, April 2021. *Use and abuse of fractals.*

- IUPUI Biomathematics Seminar, November 2020. *On respiratory droplets and face masks.*

- IUPUI Biomathematics Seminar, April 2020. *Parallel tempering: Theory, applications, and new perspectives.*

- IUPUI Biomathematics Seminar, October 2019. *Local perturbation analysis: A computational tool for biophysical reaction-diffusion models.*

- Interface of Mathematical Models and Experimental Biology: Role of the Microvasculature Conference, September 2019. *Interactions between pairs of red blood cells in microvascular flows.* Co-authors Jared Barber and Maryam Amram.

- IUPUI Biomathematics Seminar, February 2019. *Multiple attractors, saddles, and populations dynamics in periodic habitats.*

- IUPUI Biomathematics Seminar, November 2018. *Hydromechanics of low Reynolds number flow: Singularity method for Stokes flows.*

- IUPUI Biomathematics Seminar, March 2018. *Introduction to Markov chain Monte Carlo.*

- IUPUI Biomathematics Seminar, November 2017. *Dissipative particle dynamics: Introduction, methodology and complex fluid applications.*

- IUPUI Biomathematics Seminar, February 2017. *Vegetable dynamics: The role of water in plant movements.*

- IUPUI Biomathematics Seminar, October 2016. *Introduction to fluid mechanics.*

- IUPUI Biomathematics Seminar, April 2016. *Development of respiratory control instability in heart failure.*

- IUPUI Biomathematics Seminar, November 2015. *Structural remodeling of mouse gracilis artery after chronic alteration in blood supply.*

PROFESSIONAL ASSOCIATIONS

- **Society for Industrial and Applied Mathematics, IUPUI Student Chapter.**

  - President, 2020–2021.

  - Vice President, 2017–2020.

  - Participant, 2015–2017.

FELLOWSHIPS AND AWARDS

- **IUPUI School of Science Graduate Student Teaching Award, 2019.**
  Nominee of the Mathematical Sciences department.

- **IUPUI University Fellowship, 2015.**
  One of four Ph.D. candidate recipients across all departments.

- **20 Points, 74th Annual Putnam Competition, 2013.**
  Ranked 597 out of 4,113 participants nationwide.